REMOVAL OF MERCURY AND IODIDE FROM WATER USING FLY ASH DERIVED ZEOLITES AND NANOCOMPOSITES

Zhandos Tauanov

A thesis is submitted in partial fulfillment of the requirement of Nazarbayev University for the degree of Doctor of Philosophy

June 2019

DECLARATION

I declare that the research contained in this thesis, unless otherwise formally indicated within the text, is the original work of the author. The thesis has not been previously submitted to this or any other university for a degree and does not incorporate any material already submitted for a degree.

Signed:

Dated:

ABSTRACT

With growing issue of the abundance of coal fly ash throughout the world that occupy landfills by creating both environmental and health problems, the requirement for an effective utilization method is constantly growing. Another issue that also needs to be tackled is the contamination of water with hazardous metals and radioactive ions, such as Hg^{2+} and I^-. There is a huge interest of research community in conversion of coal fly ash into zeolites and composites. The impetus is on the optimization of its production process and modification with silver nanoparticles. This, however, requires a thorough understanding of coal fly ash zeolitization conditions and mechanisms. The preferred route of the synthesis of zeolites is the hydrothermal treatment of coal fly ash in a strong alkali solution at elevated temperatures, followed by doping of silver nanoparticles. The process involves several parameters, such as reaction temperature, time, the concentration and L/S ratio, Si/Al ratio in coal fly ash. These parameters appear to have an arbitrary effect on the yield of zeolite and the nanocomposite produced thereof. We propose a conversion model using the fuzzy system and optimize the zeolitization process. The model is designed and developed, using the data, both from literature and experiments, and is later optimized to provide accurate inferences. Further, the doping of silver nanoparticles to produce nanocomposites and using the novel nanocomposite for efficient remediation of Hg^{2+} and I^- from water to study the mechanism by multiple advanced characterization methods. The results indicate that the model accurately predicts the conversion of coal fly ash into zeolite for a given set of reaction parameters. Average deviation between the model predictions and experimental values for zeolite yield is less than 5%. Moreover, the model also assists in characterizing the dependence of conversion on individual parameters, which further sheds light on the mechanism(s) of zeolite formation. Furthermore, the produced novel nanocomposites demonstrate a fast and efficient removal of Hg^{2+} and I^- (up to 99% and 94.85%, respectively) from the water. The investigation of reaction mechanism shows that nanocomposite adsorbs the pollutants through a chemisorption by forming an amalgam and precipitate, while the parent coal fly ash and zeolites undergo a physisorption. Thus, the proposed nanocomposite might be an alternative material for a enhanced removal of Hg^{2+} and I^- from water that may help to reduce the accumulated coal fly ash reserves and to resolve the water contamination.

ACKNOWLEDGEMENTS

First of all, I would like to thank Allah for giving me this incredible opportunity to carry out research, study, learn and meet new people in my life, for his support and guidance through all these years.

I would immensely like to thank *Prof. Vasileios Inglezakis* with whom I have had the great honor and pleasure of working for over the last four years. His strong management skills and ability to accomplish targets as a scientist and mentor have been an invaluable experience and motivation for me.

My deepest thanks also goes to co-supervisors *Prof. Dhawal Shah* and *Dr. Grigorios Itskos*, who were also very supportive throughout the Ph.D. studies by helping me in designing the experiments and providing critical reviews of manuscripts. I am also grateful to our research team and colleagues, namely *Alzhan Baimenov*, *Leila Abylgazina*, *Aliya Satayeva*, *Azat Seitkhan* and *Almira Yagofarova*, who shared my success and fails, suggested the ways to improve and sometimes even helped me to set-up and run the experiments.

A special thanks and appreciation goes to *Prof. Luis R. Rojas-Solorzano* and his team, who virtually transformed the PhD program with their sincere willingness and motivation to change for the better. They are always open to discuss any raising issues with students and ready to support, guide and help.

And last, but not least, I would like to express my endless love, sincere appreciation to my father *Toregul Tauanov* and mother *Zhanar Kogambayeva*, to my sisters *Aigul Tauanova*, *Gulzat Tauanova*, *Anar Tauanova* and brother *Aidos Tauanov*, to my wife *Aidana Tolepova* and son *Alikhan Toregul*, who have fully supported, motivated and driven me throughout the Ph.D. adventure.

Zhandos Tauanov

CO-AUTHORSHIP STATEMENT

This thesis is an integration of five published work, which includes three published conference articles and two published journal articles, and two submitted research articles.

The research article published in *Journal of Cleaner Production* entitled "Hydrothermal synthesis of zeolite production from coal fly ash: a heuristic approach and its optimization for system identification of conversion" has been co-authored with D. Shah, P.K. Jamwal and V. Inglezakis [1], while the research articles published in *Journal of Environmental Management* and *Journal of Environmental Science and Health, Part A* entitled "Synthetic coal fly ash-derived zeolites doped with silver nanoparticles for mercury (II) removal from water" and "Synthetic sodalite doped with silver nanoparticles: Characterization and mercury (II) removal from aqueous solutions" have been co-authored with P. Tsakiridis, S. Mikhalovsky, D. Shah and V. Inglezakis [2,3]. The research article published in Science of the Total Environment entitled "Removal of iodide from water using silver nanoparticles-impregnated synthetic zeolites" has been co-authored with V. Inglezakis [4].

The conference articles published in *IOP conference series: Materials Science and Engineering* entitled "Optimized Production of coal fly ash derived synthetic zeolites for mercury removal from wastewater" has been co-authored with D. Shah, G. Itskos and V. Inglezakis [5], and "Mineralogical, microstructural and thermal characterization of coal fly ash produced from Kazakhstani power plants" has been co-authored with L. Abylgazina, C. Spitas, D. Shah, G. Itskos and V. Inglezakis [6]. The conference article published in *MDPI Proceedings* that is entitled as "Silver nanoparticles impregnated zeolites derived from coal fly ash: effect of the silver loading on adsorption of mercury (II)" has been co-authored with D. Shah and V. Inglezakis [7].

The contributions of the author of the thesis in published journal articles, conference articles and submitted manuscripts, as the first author of work, include the literature review, full experiment implementation, data collection, analysis and management, and preparation of the first drafts of manuscripts. The co-authors contributed to critical review, the design of experiments and preparation of the final manuscripts.

PREFACE

Mr. Zhandos Tauanov received his B.Sc. (with honors) degree in Chemical Technology of Organic Substances from Al-Farabi Kazakh National University in June 2010 (Almaty, Kazakhstan). He received M.Sc. (with distinction) degree in Advanced Process Engineering from Loughborough University in December 2011 (Loughborough, UK). From November 2011 to January 2012 he worked as a proposal evaluation manager in JSC "National Center of State Science and Technology Evaluation", and then as a teaching assistant in AOE "Nazarbayev University" from January to September 2012. Then, he worked as a junior researcher for PE "National Laboratory Astana" from September 2012 till September 2017 and currently works as a research assistant for School of Engineering of AOE "Nazarbayev University" since April 2016. Starting from September 2015, he has been pursuing PhD degree in Materials Science and Engineering at School of Engineering of AOE "Nazarbayev University" with a research topic on synthetic adsorbents development for water remediation purposes with a focus on Hg^{2+} and I^-.

TABLE OF CONTENTS

LIST OF FIGURES

LIST OF TABLES

LIST OF ABBREVIATIONS

AAS	atomic absorption spectroscopy
AC	activated carbon
AF	activation function
ASTM	American society for testing and materials
Ag NPs	silver nanoparticles
Ag-ZFA	silver impregnated zeolitic nanocomposite
BET	Brunauer, Emmett, Teller (method of calculation)
BJH	Barrett, Joyner, and Halenda (method of calculation)
BTX	benzene, toluene, and xylene
CEC	cation exchange capacity
CBA	coal bottom ash
CFA	coal fly ash
E-CFA	Ekibastuz coal fly ash
EPA	environmental protection agency
FTIR	Fourier transform infrared spectroscopy
HVFA	high volume fly ash
HAPT	2-hydroxyacetophenone-4N-pyrrolidine thiosemicarbazones
HR	high resolution
JCPDS	joint committee powder diffraction standard
K-CFA	Karazhyra coal fly ash
K-R-ZFA	reduced Karazhyra zeolite
K-ZFA	zeolite produced from Karazhyra coal fly ash
LOI	loss on ignition
LTA CFA	Linde type A coal fly ash
MA	mercury analyzer
MARS	microwave-assisted reaction system
MCL	maximum contaminant level
M-CFA	Maikumen coal fly ash
M-R-ZFA	reduced Maikuben zeolite

M-ZFA	zeolite produced from Maikuben coal fly ash
MIL	Matérial Institut Lavoisier (a metal organic framework)
NP	nanoparticle
PN	nitrogen porosimeter
PSA	particle size analyzer
PSD	particle size distribution
SEM	scanning electron microscopy
SSA	specific surface areas
TC	total carbon
TEM	transmission electron microscope
TG-DSC	thermogravimetry and differential scanning calorimetry
TS	Takagi-Sugeno (a fuzzy system)
UV-Vis	ultraviolet-visible spectrometer
XRD	X-Ray diffraction
XRF	X-Ray fluorescence
ZP	zeta potential
ZSM-5	zeolite socony mobil-5 (a commercial zeolite)

LIST OF SYMBOLS

L/S	liquid to solid ratio
Si/Al	silica to alumina ratio
pH_{ZPC}	point of zero charge
$\boldsymbol{M_i}$	number of activation functions
$\boldsymbol{\sigma_i}$	standard deviation
$\boldsymbol{R_i}$	range of variables
$\boldsymbol{v_i}$	variables
$\boldsymbol{N_r}$	total number of rules
$\boldsymbol{n}$	number of input variables
$\boldsymbol{m_k}$	activation functions
$\boldsymbol{y_i}$	consequent variables
$\boldsymbol{Y}$	consequent vector
$\boldsymbol{W}$	regressor matrix
$\boldsymbol{w_i}$	fulfilment degree
$\boldsymbol{w_i}$	normalized degree of fulfilment
$\boldsymbol{I_k}$	k^{th} input number
$\boldsymbol{A_{kL}(I_k)}$	input variables in “Low” activation function
$\boldsymbol{A_{kH}(I_k)}$	input variables in “High” activation function
$\boldsymbol{e}$	Euler’s number
$\boldsymbol{a}$	constant given by $1/(\sigma\sqrt{2\pi})$
$\boldsymbol{P_{ik}}$	selection vector
$\boldsymbol{E}$	the expected value of the squared errors for the magnitude of zeolite yield
$\boldsymbol{N}$	the total number of experimental observations
$\boldsymbol{C_p}$	output from the fuzzy model
$\boldsymbol{C_p^e}$	the zeolite yield from p^{th} experiments for the same set of inputs
$\boldsymbol{p_{km}}$	the vector of antecedent fuzzy AF parameters for k^{th} input and m^{th} AF
$\boldsymbol{t}$	number of epochs
$\boldsymbol{\alpha}$	constant for the learning rate

2θ	diffraction angle
q_e	the equilibrium adsorption capacity
q_t	the adsorption capacity at time *t*
C_0	the initial concentration of solution
C_e	the equilibrium concentration of solution
C_t	the concentration of solution at time *t*
V	the volume of the aqueous solution used for adsorption experiment
m	the weight of the adsorbent used for adsorption experiment
$\bar{X}$	the dimensionless averaged fluid and solid concentrations
$\bar{C}_t$	the average fluid phase concentration at time *t*
$\overline{C_o}$	the initial concentration of fluid
Λ	the partition ratio
M	the solid mass
V_L	the fluid volume
$\overline{q_o}$	the average fluid phase concentration at equilibrium
$U(T)$	the fractional attainment of equilibrium
T	the dimensionless time
r_p	the particle radius
D_s	the constant surface diffusion coefficient

CHAPTER 1

INTRODUCTION

1.1. Utilization of coal fly ash in adsorption of pollutants

Coal is one of the ecosphere's most abundant and broadly distributed fossil fuel, with total proven reserves accounting for approximately 1000 billion tones [8]. The recent data on literature confirms that coal is still commonly used category of fuel in several unindustrialized and industrialized states such as South Africa (93%), Poland (92%), China (79%), India (69%) and the USA (49%) [2]. According to the literature, almost one-third of global electricity is produced from coal in 2011 and it is estimated to reach around 46% after two decades [9]. There are several dominating states that produce the majority share of coal and hence massively consume coal resources yearly, namely China, USA, Russia, India, and other countries, wherein Kazakhstan is estimated to produce 120 million tons annually [10]. Furthermore, the total consumption statistics show that 5% is accounted for Eurasian countries and Kazakhstan is among three CIS nations with a substantial 22% [8].

Coal fly ash (CFA) is a waste material of power plants, where coal is primarily used for electricity generation. The volume of yearly produced CFA is huge, hence it requires further investigation on utilization as it grounds severe ecological and health issues [2,11]. For instance, Kazakhstan yields about 19 million tons of CFA annually, and presently storing 300 million tons of fly ash in dumping zones [6]. With continuously increasing demand for energy and considering a heavy reliance of many states on coal industry, it is vital for countries to efficiently reuse and recycle CFA. According to figures of Kazakhstan, less than 10% of all fly ash is recycled and reused, which is significantly lower than indexes in developed states, such as the US (about 50%), EU states (more than 90%), China (almost 70%) and India (60%) [8].

Numerous attempts have been conducted worldwide to effectively recycle this abundant by-product. Of these efforts, one of the prominent solutions propagated is to utilize the CFA by converting it to some value-added products, such as synthetic zeolites and composite materials for water and gas purification purposes [12–16]. Multiple studies include a successful laboratory-scale application of CFA derived zeolites for heavy metals and dyes uptake from aqueous media [5,17–20]. Some researchers have also attempted to remove

mercury (Hg) both from aqueous phase [16,21] and flue gas as Hg° [22–25] using waste derived adsorbents, including synthetic zeolites, red mud, and mineral-based porous materials.

Recent studies also include zeolites and their composites that are doped or impregnated with metal or metal oxide nanoparticles (NPs), which consecutively further expands the application fields. For instance, they could be applied as adsorbents to remove aromatic compounds from aqueous media [26], as nanocomposites to use for antibacterial activities [27], as an enhancer of solar light in photocatalytic performance [28], as catalysts in reduction [29], hydrogenation and dehydrogenation reactions [30], as adsorbents to remove phosphates and ammonium [31,32] from aqueous solutions and many other fields.

Many researchers globally are examining the possible methods of remediation of wastewater from hazardous and toxic metals, halides, particularly to remove species of Hg^{2+} and I^-, to facilitate a cost-effective, fast and efficient approach. Among all mentioned metal and metal-oxide containing composites, a specific interest sets on silver (Ag) and silver oxide (Ag_2O) NPs doped in zeolitic nanocomposites derived from CFA since they retain the unique capability to form amalgams and precipitates with Hg^{2+} and I^- [33–36]. According to present protocol of the US Environmental Protection Agency (EPA) the maximum contaminant level (MCL) of Hg^{2+} concentration is 0.2 ppb. Thus, it requires an improved methods of removal and storage of these pollutants.

Another hazardous pollutant is the radioactive iodine isotopes, such as ^{129}I, ^{131}I, and since their transformation *via* dissolution and sublimation into water and air cause major issues. They adversely affect both human health and the ecosystem. The massive disasters occurred in nuclear power plants in Chernobyl and Fukushima raised further concerns on radioactive waste utilization, remediation of dissolved I^- and entrapment of sublimated iodine. The worst scenario in radioactive isotopes of I^- is there prolonged half-lifes, which might be as long as millions of year. Hence, all these issues require an effective approach of sequestration of I_2 and I^- from both aqueous and gaseous systems, which allows a selective removal of I^- over other competing and co-existing anions in the water environment.

Silver NPs containing nanocomposites have already found applications fields, such as an antibacterial component for disinfection, catalysis, oxidation and photocatalytic reactions, heavy metals removal, electrical properties enhancement of porous microstructures.

Typically, Ag and Ag_2O NPs are introduced into the zeolite structure *via* ion exchange followed by oxidation and reduction reactions. Some studies include where researchers utilized Ag NPs containing nanocomposite for heavy metals removal [21,36], however there is very limited work on Ag NPs containing zeolite nanocomposites used for removal of Hg^{2+} and I^- from aqueous and gaseous media (both elemental and ionic forms), particularly by means of nanocomposites derived from CFA.

The main motivation behind this study was to explore the utilization of Ag NPs containing nanocomposites for Hg^{2+} and I^- ions removal. Considering a relatively low-cost CFA resource, it could be effectively applied to produce Ag NPs containing composites that may address two issues: utilization of CFA and resolving the water resources contamination with Hg^{2+} and radioactive I^-. In this work, CFA derived synthetic zeolites and novel Ag NPs doped zeolitic porous nanocomposites are produced and tested for Hg^{2+} and I^-removal under simulated batch adsorption conditions. The adsorption capacity of all obtained zeolites and Ag NPs doped nanocomposites were compared with their parent CFAs in terms of microstructure, mineralogy, morphology, thermal and adsorption capacities.

1.2. Thesis hypothesis and statements

The literature review on worldwide CFA utilization fields demonstrate the possibility to produce synthetic zeolites from waste CFA that could be used as a substrate for Ag NPs containing nanocomposites to address the issues of water contamination with Hg^{2+} and I^-, have triggered the following thesis hypothesis and statements.

Thesis hypothesis:

- CFA derived synthetic zeolites could be effectively produced by systematic investigation and modeled using a heuristic approach under optimum reaction conditions for system identification of conversion.
- Ag NPs could be homogeneously dispersed within the microstructure of CFA derived nanocomposite and efficiently used for Hg^{2+} and I^- removal from wastewater.

- The adsorption mechanism, maximum adsorption capacity and effect of the competing ions on Hg^{2+} and I^- uptake could be effectively predicted by means of advanced characterizations methods and analysis.
- The diffusion based model on the AgI precipitation reaction could be applied to estimate the solid phase diffusion coefficient and validate the experimental results.

Thesis statements:

- To conduct an advanced literature review on the synthesis and application of zeolites and nanocomposites with metal nanoparticles for Hg^{2+} and I^- removal from water;
- Considering the different concentration of constituents in CFA, develop synthetic zeolites and identify the optimum conditions to produce them;
- To conduct a factorial analysis and optimize the production of synthetic zeolites using a heuristic modeling approach;
- To impregnate Ag NPs into synthetic zeolite microstructure and fully characterize them on multiple advanced instruments to explore the microstructure, mineralogy, thermal and surface properties;
- To effectively use a novel CFA derived nanocomposite with doped Ag NPs for removal of Hg^{2+} and I^- by identifying optimum conditions;
- To study the underlying adsorption mechanisms of Hg^{2+} and I^- in novel nanocomposites and proving them employing advanced characterization instruments (XRD, XRF, SEM-EDS, TEM-EDS, BET) and calculations;
- To model the adsorption kinetics and isotherm of Hg^{2+} and I^- for nanocomposites by applying the governing equations and experimental results.

1.3. The novelty of the research

The key novelties of the Ph.D. research work, to the best of author's knowledge, are:

- The application of heuristic modeling approach and experimental factorial analysis for system identification of conversion of CFA into synthetic zeolite. There are no existing theoretical or mathematical reaction models that enable to

elucidate or control the synthesis of zeolite from CFA. While conservative numerical and analytical modelling methods could not emulate such processes with accuracy, there exist heuristic approaches that could be employed to efficiently model uncertain and ambiguous systems.

- The production of Ag NPs doped composite materials from CFA derived synthetic zeolites, performing the studies on leaching of the adsorbed Hg^{2+} and I^-, examination of the co-existing an competing anions effect on the removal profile and investigation of the detailed mechanism of removal of Hg^{2+} and I^- from water using advanced characterization techniques;
- Modeling the adsorption kinetics and isotherms of Hg^{2+} and I^- by applying governing equations and experimental results. The utilization of the CFA-derived novel nanocomposites for removal of I^- from water and the application of a diffusion-based model on the *Ag-I reaction* on porous materials that is the first time presented in the related literature.

1.4. Research contributions

The list of published research articles and submitted research manuscripts:

1) Z. Tauanov, D. Shah, V. Inglezakis, P.K. Jamwal. Hydrothermal synthesis of zeolite production from coal fly ash: A heuristic approach and its optimization for system identification of conversion. *Journal of Cleaner Production*, 182, 616-623, 2018.
2) Z. Tauanov, P.E. Tsakiridis, S. Mikhalovsky and V. Inglezakis "Synthetic coal fly ash-derived zeolites doped with silver nanoparticles for mercury (II) removal from water". *Journal of Environmental Management*, 224, 164-171, 2018.
3) Z. Tauanov and V. Inglezakis "Removal of iodide from water using silver nanoparticles-impregnated synthetic zeolites". *Science of the Total Environment*, 682, 259–270, 2019.
4) Z. Tauanov, P.E. Tsakiridis, D. Shah and V. Inglezakis "Coal fly ash-derived sodalite doped with silver nanoparticles: mercury (II) removal potential from simulated water". *Journal of Environmental Science and Health, Part A*, doi: 10.1080/10934529.2019.1611129.

The list of published conference proceedings:

1) Z. Tauanov, L. Abylgazina, C. Spitas, G. Itskos, and V. Inglezakis. “Mineralogical, microstructural and thermal characterization of coal fly ash produced from Kazakhstani power plants”. *IOP Conf. Ser.: Mater. Sci. Eng*. 230, 012044, 2017.
2) Z. Tauanov, D. Shah, G. Itskos and V. Inglezakis. “Optimized production of coal fly ash derived synthetic zeolites for mercury removal from wastewater”. *IOP Conf. Ser.: Mater. Sci. Eng.* 230, 012046, 2017.
3) Z. Tauanov, D. Shah, and V. Inglezakis. “Silver nanoparticles impregnated zeolites derived from coal fly ash: effect of the silver loading on adsorption of mercury (II)”. *MDPI Proceedings*, 2(11), 647; 2018.

The list of presentations on international conferences, seminars and research weeks:

1) Z. Tauanov, S. Sandeman, D. Berillo, D. Shah and V. Inglezakis "Fly ash derived synthetic zeolites impregnated with silver nanoparticles: characterization and mercury removal potential". Postgraduate Research Week, May 2017, University of Brighton, Brighton, UK (Erasmus+ program, oral and poster presentations).
2) Z. Tauanov, D. Shah, G. Itskos and V. Inglezakis "Optimized production of coal fly ash derived synthetic zeolites for mercury removal from wastewater". International Conference on Materials Sciences and Nanomaterials, July 2017, Barcelona, Spain (oral presentation).
3) Z. Tauanov, L. Abylgazina, C. Spitas, G. Itskos and V. Inglezakis "Mineralogical, Microstructural and thermal characterization of coal fly ash produced from Kazakhstani power plants". International Conference on Materials Sciences and Nanomaterials, July 2017, Barcelona, Spain (oral presentation).
4) S. Poulopoulos, V. Inglezakis, D. Shah, Z. Tauanov, Grigorios Itskos "Fly ash derived synthetic zeolites impregnated with silver nanoparticles: characterization and mercury removal potential", 10th World Congress of Chemical Engineering (WCCE-10), Barcelona, Spain, October 2017 (poster presentation).
5) Z. Tauanov Z., S. Dhawal, G. Itskos, and V. Inglezakis. "Silver nanoparticles impregnated zeolitic composites derived from coal fly ash: Effect of the silver

loading on adsorption of mercury (II)" 3rd Efficient Water Systems (EWaS) International Conference, June 2018, Lefkada Island, Greece (oral presentation).

6) Z. Tauanov, D. Shah, G. Itskos, S. Mikhalovsky and V.J. Inglezakis "Coal fly ash derived nanocomposite for mercury removal from wastewater: effect of the anions". Carbon-2018, July 2018, Madrid, Spain (keynote speech).
7) Z. Tauanov, D. Shah, G. Itskos, and V.J. Inglezakis "Synthesis of fly ash-derived nanocomposite and utilization for mercury removal from wastewater. Green Energy and Municipal Solid Waste Management Solutions, 12 September 2018, Nazarbayev University, Astana, Kazakhstan (oral presentation).

1.5. Thesis organization

The PhD thesis consists of seven chapters. Chapter 1 is the introduction that provides an overview of the research, thesis hypothesis and statements, novelty and key contributions.

Chapter 2 presents a comprehensive literature review on the relevant research work presented in the thesis. The first section covers the topics that include the CFA classification, composition and utilization studies, while the second section discusses the Hg^{2+} and I^- contamination of water resources, the existing species and isotopes of these ions, and the state of the art remediation methods. The third section presents the possible ways of synthesis of zeolites from CFA, which comprises the hydrothermal treatment, fusion-assisted treatment, sonication and microwave-assisted syntheses. The literature review is summarized by application fields of CFA derived materials in the fourth section.

Chapter 3 includes the list of materials, physical and chemical methods applied during the synthesis and the detailed descriptions of advanced microstructural, morphological, mineralogical, chemical and thermal characterizations employed on pre- and post-adsorption materials loaded with Hg^{2+} and I^-. Furthermore, the details of the adsorption experiments, which includes the kinetics, isotherms, effects of the competing and co-existing anions, leaching studies and impact of the Ag NPs loading are described.

Chapter 4 presents the research outcomes conducted on full characterization of synthetic zeolites and parent CFAs that comprise microstructural, morphological, mineralogical,

chemical and thermal analysis, followed by the factorial analysis of the production of zeolites from CFA and optimization results using the fuzzy model based on the experimental and literature data. The research contributions based on these work are published in *Journal of Cleaner Production* with research paper entitled "Hydrothermal synthesis of zeolite production from coal fly ash: a heuristic approach and its optimization for system identification of conversion", and two conference papers published in *IOP conference series: Materials Science and Engineering* that are entitled "Optimized production of coal fly ash derived synthetic zeolites for mercury removal from wastewater" and "Mineralogical, microstructural and thermal characterization of coal fly ash produced from Kazakhstani power plants".

Chapter 5 focuses on the Hg^{2+} removal studies, particularly, the research on adsorption kinetics, adsorption equilibrium isotherms, leaching studies along with maximum adsorption capacity, and effect of the silver loading and co-existing anions on the removal performance of the novel nanocomposites and zeolites. The emphasize is given to the proposed mechanistic studies of Hg^{2+} removal from water using nanocomposites and parent zeolites that is confirmed via multiple advanced characterization techniques. The research findings based on these studies are published in *Journal of Environmental Management* with research paper entitled "Synthetic coal fly ash-derived zeolites doped with silver nanoparticles for Hg^{2+} removal from water" and *Journal of Environmental Science and Health, Part A* "Synthetic sodalite doped with silver nanoparticles: characterization and mercury (II) removal from aqueous solutions".

Chapter 6 studies the potential application of novel nanocomposites for remediation of I^- from water. The research themes that are covered include the adsorption kinetics and equilibrium isotherms, the insights into mechanistic studies of adsorption that are confirmed via advanced characterization methods, effect of the competing and co-existing anions and leaching studies that emphasizes the advantages of nanocomposites. The research results of based on these studies are published in *Science of the Total Environment* journal with research paper entitled "Removal of iodide from water using silver nanoparticles-impregnated synthetic zeolites".

Chapter 7 concludes the thesis by providing a possible future research that might be accomplished in order to further expand and improve the related work.

CHAPTER 2

LITERATURE REVIEW

2.1. Coal fly ash as a waste and raw material

2.1.1. Worldwide coal consumption

Coal is one of the world's most plentiful and broadly disseminated fossil fuel, with global proven resources valuing for almost 1000 billion tones [1]. It is still a frequently employed sort of combustible in multiple progressing and progressed countries. According to Yao *et al*. [3], coal-fired power production considered to 29.9% of global power production in 2011 and it is forecasted to touch approximately 46% by 2030. According to last decade statistics, PRC is the dominant consumer of coal worldwide with a share of more than 50% of the total world coal consumption in 2012 [9]. This trend is followed by the US and India with an annual consumption rate of 11.7% and 8%, respectively. The industrialized Asian countries, such as Japan (3.3%), South Korea (2.2%) and Indonesia (1.4%) also consume a large proportion of the world share as shown in Figure 2.1.

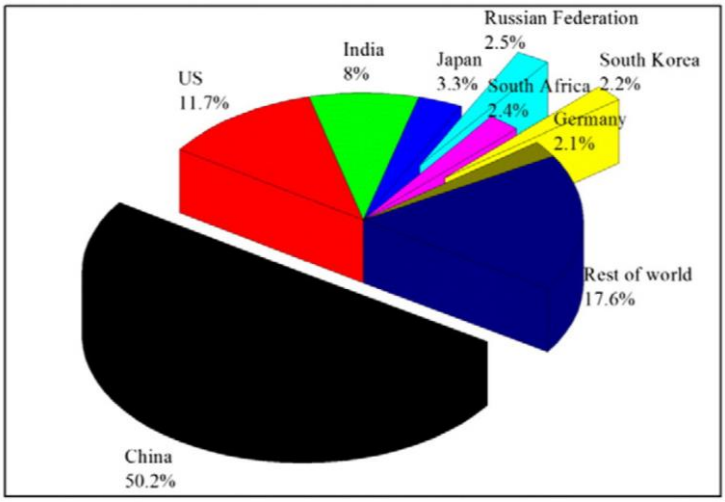

Figure 2.1. The coal consumption share worldwide in 2012 (taken from [9])

It is commonly known that coal is the primary source of energy (electricity) production and industrial growth of many countries depend on coal energy consumption. For example, in PRC almost 68.5% of energy is produced from coal in 2012 (Figure 2.2), whereas the shares

of energy produced from coal of developed and developing countries as the US, Japan and India account for 20, 53 and 21.78%, correspondingly [9].

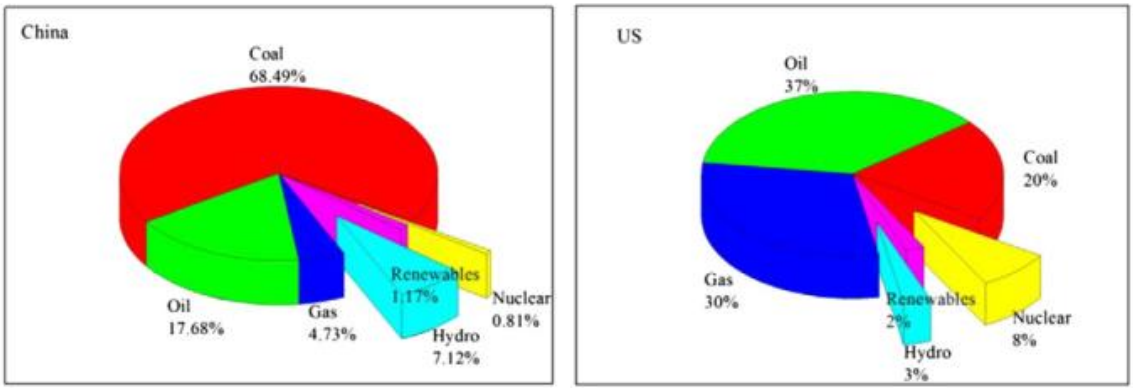

Figure 2.2. Consumption of energy by fuel type in 2012: China vs. USA (taken from [9])

The research conducted by the World Coal Institute [10] demonstrates an energy and moisture content of coal depending on origin with the estimated world reserves of each category and primary utilization fields as shown in Figure 2.3. Generally, according to their classification, a coal is classified into two groups: a low-rank coal that comprises about 47% of total coal reserves (lignite and sub-bituminous) and hard coal (bituminous and anthracite) that includes approximately 53% of total coal amount.

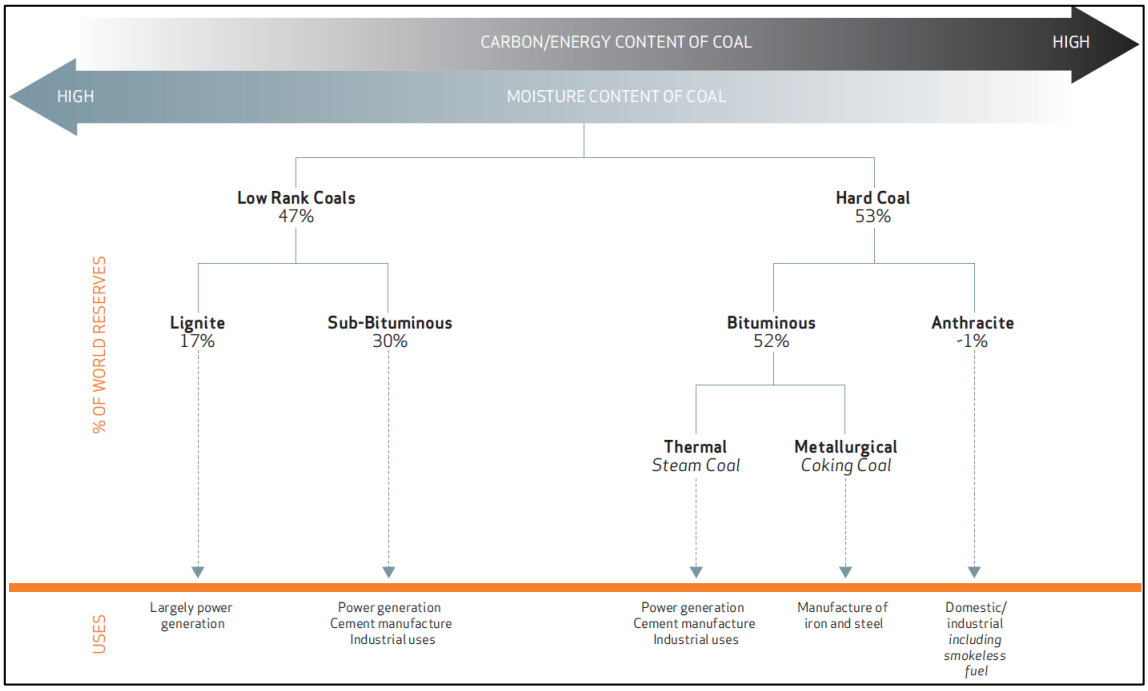

Figure 2.3. The world coal reserves classification (taken from [4])

One of the main drawbacks of energy consumption dependence on coal sources is the accumulation of coal ash that grounds environmental and health issues [37]. According to literature, a burned coal produces approximately 5 to 20wt.% of ash, which comprises both a coarse bottom ash (CBA, 5-15wt.%) and CFA (85-95wt.%) [9]. Typically, the coal ash is discharged in the form of wet and dry wastes after being used in coal combustion reactors. The bottom coal ash (CBA) is a coarse fraction of ash that is generally settled down at the bottom of combustion reactors and collected mechanically after burning process. CFA is a finer fraction of burned ash that is electrostatically or mechanically precipitated and collected in ash disposal areas after combustion.

As for the utilization of CFA, the statistics vary from country to country from a minimum of 3% to 90% [37]. The utilization index of CFA is around 50% in the US and 90% in EU states, while the recycling and reprocessing in China and India is 67% and 60%, respectively [37]. It should be highlighted that the average total ash utilization degree in the world has been improved by 9% and reached 25% [38,39], but it also indicates that almost 3/4th of the produced waste ash is still accumulated in disposal ponds and requires an appropriate recycling or reprocessing method. The projection of major inter-regional coal trade for the period of 2002-2030 conducted by the World Coal Institute [10] reveals that in most of the countries, particularly in developing regions the coal trade is expected to expand, hence it could be anticipated that the consumption will inevitably be increased (Figure 2.4). Therefore, it entails an urgent utilization of previously generated fly ash and to find other innovative and massive methods of reprocessing.

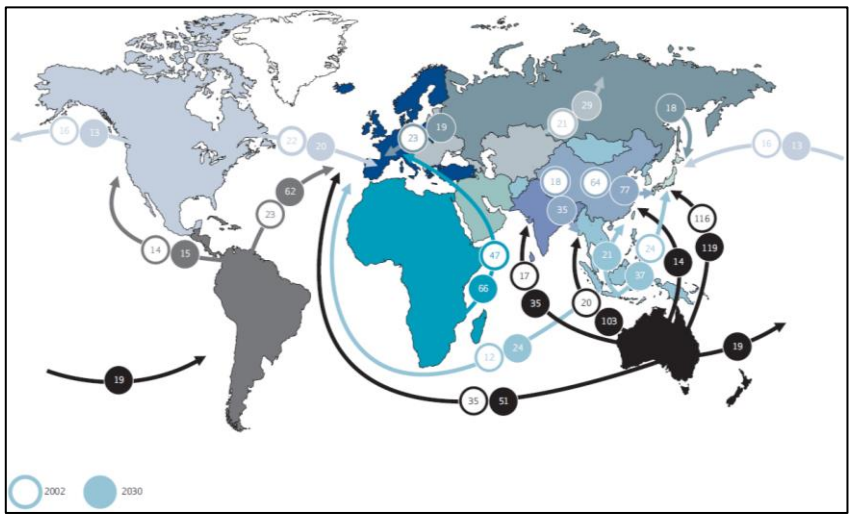

Figure 2.4. The world coal trade projection for 2002-2030 in Mt (taken from [4])

2.1.2. Coal fly ash classification and composition

CFA is a material with complex chemical and mineralogical composition that requires multiple advanced characterization methods to extract full data. Recent studies report that up to 316 individual minerals and 188 mineral groups found in various samples of ash [40–42]. According to ASTM standards (C618) CFA is classified into 2 classes: Class C, which contains more than 20% of CaO and more than 50% of combined SiO_2, Al_2O_3 and Fe_2O_3 oxides; while Class F, has the combined content of SiO_2, Al_2O_3 and Fe_2O_3 that is greater than 70% and the amount of CaO is less than 20% [11].

There are other CFA classification approaches, for example, Canada groups CFA according to the content of CaO and lost on ignition (LOI) index [37]. In this classification, CFA is grouped into Types F (<8%), CI (8-20%), CH (>20%) based on CaO content, whereas classification according to LOI indexes include Type F with CaO amount 8-12%, while other Types C, CI, and CH contain up to 6% CaO.

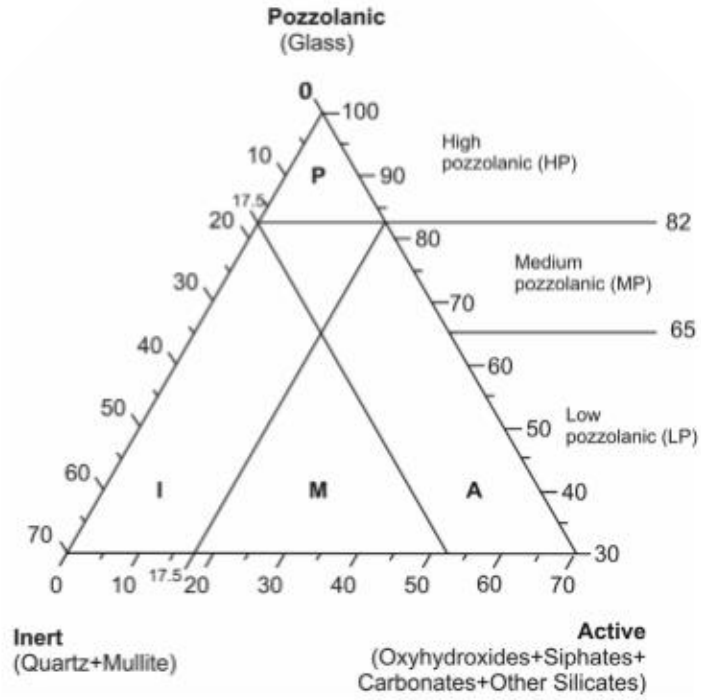

Figure 2.5. The phase-mineral classification of CFA (taken from [44])

The UN classifies CFA into 4 groups according to SiO_2/Al_2O_3 ratio and CaO content, where Group-I CFAs have SiO_2/Al_2O_3 >2 and CaO amount up to 15%; Group II includes CFAs with a SiO_2/Al_2O_3 ratio of up to 2 and CaO amount >15% with SO_3 content <3%. The Group

III CFA, on the other hand, has the amounts of CaO and SO_3 more than 15% and 3%, respectively, while the Group IV includes CFAs with CaO amount more than 15% with SO_3 less than 3% [37]. More recent classification of CFAs suggested by Vassilev and Vassileva is based on origin, mineralogy, chemical composition, physical and chemical properties. The system is diverse and hence gives a more comprehensive approach to classification that is useful when considering the application of CFAs in various fields of industry (Figure 2.5).

Table 2.1. The chemical composition of CFAs produced from various coal types

Coal type	Component (wt.%)								
	Na_2O	MgO	Al_2O_3	SiO_2	K_2O	CaO	SO_3	Fe_2O_3	LOI
Bituminous	0-4	0-5	5-35	20-60	0-3	1-12	0-4	10-40	0-15
Sub-bituminous	0-2	1-6	20-30	40-60	0-4	5-30	0-2	4-10	0-3
Lignite	0-6	3-10	10-25	15-45	0-4	15-40	0-10	4-15	0-5
Anthracite	0-1	1-4	18-36	28-57	0-4	1-27	0-9	3-16	1-8

CFAs have typically a hydrophilic surface and has more fine particles formed upon exiting the combustor, therefore tend to have a disordered structure that enhances the reactivity [43]. Generally, CFA of Type F is produced when anthracite, bituminous or sub-bituminous coal is burned and is typically low in lime and contains more silica, alumina and iron oxide; whereas CFA of Type C origins from lignite coal that contains more lime [44]. The range of chemical composition of CFAs produced from these coal types is shown in Table 2.1 [37].

The composition and mineralogical phase content of CFA is mainly dependent on the origin and type of coal burned in power plants. For instance, according to XRD analysis, most of the CFA samples contain inorganic phases as mullite, quartz, and hematite or various ferric oxide forms [18,45–47]. The principal chemical components of CFA are silica, alumina, ferrous oxide and calcium oxide with varying amounts of remaining carbon and trace elements. Table 2.2 summarizes a comparative chemical composition of CFAs from different countries.

Table 2.2. The chemical composition of CFAs from different continents [11]

Compound	Regions and component (wt.%)				
	Europe	US	China	India	Australia
SiO_2	28.5-59.7	37.8-58.5	35.6-57.2	50.2-59.7	48.8-66.0
Al_2O_3	12.5-35.6	19.1-28.6	18.8-55.0	14.0-32.4	17.0-27.8
Fe_2O_3	2.6-21.2	6.8-25.5	2.3-19.3	2.7-14.4	1.1-13.9
CaO	0.5-28.9	1.4-22.4	1.1-7.0	0.6-2.6	2.9-5.3
MgO	0.6-3.8	0.7-4.8	0.7-4.8	0.1-2.1	0.3-2.0
Na_2O	0.1-1.9	0.3-1.8	0.6-1.3	0.5-1.2	0.2-1.3
K_2O	0.4-4.0	0.9-2.6	0.8-0.9	0.8-4.7	1.1-2.9
P_2O_5	0.1-1.7	0.1-0.3	1.1-1.5	0.1-0.6	0.2-3.9
TiO_2	0.5-2.6	1.1-1.6	0.2-0.7	1.0-2.7	1.3-3.7
MnO	0.03-0.2	no data	no data	0.5-1.4	no data
SO_3	0.1-12.7	0.1-2.1	1.0-2.9	no data	0.1-0.6
LOI	0.8-32.8	0.2-11.0	no data	0.5-5.0	no data

The chemical characteristics of CFA have been thoroughly investigated and it is recognized that CFAs comprise multiple components at concentrations of higher than 50 mg/kg. Some of those components may entail an environmental issue [48]. Table 2.3 presents the concentrations of trace elements in 23 European samples of CFA. They are generally in accordance with the elemental composition of Australian CFA interpreted by Jankowski *et al*.. [49]. It is remarkable that heavy metals, such as Ba, Cr, Ni, Rb, Pb, Sr, Zn, and V are existing in a notable amount. Because of this, mobility studies have been carried out to evaluate the probability of those elements leaving to the surrounding environment. The leachability of the elements is closely associated with the phase with that they are correlated and the leaching states such as the solution pH [50].

Table 2.3. The trace element content of CFAs (ppm)

Elements	As	Ba	Cr	Cu	Li	Ni	Pb	Rb	Sr	V	Zn
Median value	55	1302	148	86	185	96	80	108	757	228	154

2.1.3. Utilization fields of coal fly ash

The main application fields of CFA is currently attributed to construction, ceramic, environmental and agricultural sectors. According to statistics, the industrialized countries as the US and EU states predominantly utilize the fly ash in concrete and cement production, waste stabilization, mining applications, as structural fills and embankments, for reclamation and restoration that in total accounts for more than 60-70% of all CFAs [9].

Environmental applications

The physical and chemical properties of CFA is favorable for retention of various organic and inorganic pollutants and it is broadly examined as an adsorbent in different environmental fields. The unburnt carbon containing in CFA adds some additional advantages, which increases an adsorption capacity of the material. Numerous studies have been carried out on the application of CFA for heavy and toxic metals removal from both gaseous and aqueous environment. The first studies were conducted in 1984, where CFA was used as an adsorbent of divalent copper (Cu^{2+}) from industrial wastewater [51]. More recently, Cho *et al.* examined the adsorption of Zn^{2+} and Cd^{2+} in batch experiments at room temperature under various pH values of 3 to 10. According to the results, the adsorption underwent by the Freundlich model and the experiments with real wastewater solutions suggested that CFA could be used as a low-cost adsorbent [52]. CFA has also been studied for removal of other heavy metals, such as Pb^{2+}, Ni^{2+} and Cr^{3+} [53–55]. Some research groups also investigated the hazardous metals as Hg (II), As (III) and As (V). The experiments on adsorption elemental Hg using CFA showed attractive outcomes [56–58], however, there are still gaps on understanding the detailed mechanism of adsorption that might occur due to the interaction of unburnt carbon with Hg or fly ash and Hg, hence these variables require further investigations.

CFA has been successfully used for adsorption of organic pollutants. For example, CFA has adsorbed phenol with adsorption capacity reaching 27.9 mg/g that is comparable with commercially used activated carbon that shows an adsorption capacity of 108 mg/g [59]. Yet another study on adsorption of halogenated phenols using CFAs showed the adsorption capacities of 98.7 mg/g and 118.6 mg/g for 2-chlorophenol and 4-chlorophenol, accordingly [60]. CFA has also been considered as an effective adsorbent for removal of polychlorinated

biphenyls [61], chrysoidine R dye [62], herbicides, such as metribuzin and atrazine [63] from aqueous media.

Another environmental application of CFA includes the adsorption of greenhouse emissions, namely CO_2, SO_2, and NO_x flue gases. The recent investigations on desulfurization of the flue gas using $Ca(OH)_2$ enriched CFA show that adsorption increase with the ratio of CFA to $Ca(OH)_2$ [64]. According to experimental results obtained by Lu and Do on adsorption of NO_x using CFA, the authors claim the positive effect of unburnt carbon on adsorption capacity, which could further improve the performance of material upon activation [65]. A more recent study on capturing CO_2 applying CFA based composites demonstrated that relatively cost-effective and abundant material could be an efficient alternative for CO_2 capture [66]. Other environmental applications of CFA include the adsorption of phosphates [67,68], humic acids [69] and pesticides [70].

To sum up the pollutant removal potential of CFA, it could be concluded that chemical and physical properties of CFA are favorable and in some cases, the crucial effect might occur owing to the presence of unburnt carbon as it has a high surface area, which is important for adsorptive methods of remediation.

Construction industry

It is widely known that the predominant field of utilization of CFA worldwide is the construction industry. Figure 2.6 shows the breakdown of CFA utilization in China and India, two major countries that produce a huge amount of CFA annually [9]. It is clearly seen that in China a huge proportion of CFA is utilized in the manufacturing of bricks and tiles, as well as in cement (41%) and concrete production (19%). The statistics of India is similar in terms of cement production (44.76%), followed by reclamation (16.72%) and mine filling (9.1%). The remaining proportion of CFA is shared with other application sectors, such as road construction and embankments, agricultural use and others.

There are certain reasons why the CFA is used for cement and concrete production as it is cheap and abundant. Also, the pozzolanic nature of some CFAs makes them useful for cement replacement in concrete production [71]. CFA could also improve the long-term durability properties of concrete by reducing the ingress of aggressive agents such as chloride ions [72]. The studies on low lime CFA show that 45wt.% of material with portland

cement could allow designing practical strength although with the initial strength to be reduced to some extent [73]. The demand and interest of scholars in high volume fly ash (HVFA) concrete has increased over the last decade, as it is more environmentally and economically feasible material. There are many studies on a laboratory scale and field trials up to 50-75% CFA in concrete production and testing [74]. According to literature the main benefits of HVFA concrete compared with conventionally used types are improved stability and dimensional stability, superior durability [11] and enhanced chloride permeability [75].

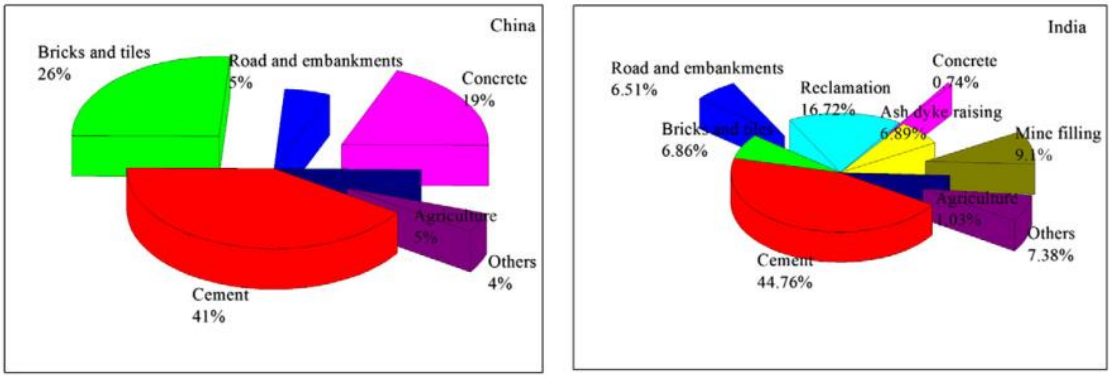

Figure 2.6. CFA utilization fields in China and India (taken from [9])

It is important to note that recent studies on geopolymers, which could be produced from aluminosilicate rich CFA by alkali-activation technology, become a promising cement alternative in civil engineering. Geopolymers possess attractive physicochemical and mechanical properties that include low density, shrinkage, improved mechanical strength, micro and nanoporosity, thermal stability and chemical resistance [11]. All these properties of geopolymers advance the production of this material from CFA and application in the construction sector. Geopolymers produced from CFA usually harden instantly at ambient temperature and have mortar compressive strength of 80-120 MPa [76,77] and concrete strengths of about 70 MPa [78] as reported in the literature. Another study on CFA based geopolymer mortar manufacturing with varying content of sand aggregate demonstrates that material has 60 MPa compressive strength and 2.27 GPa Young's modulus with insignificant change of these values up to 50wt.% of sand aggregate content [79].

The predominance of CFA in the construction industry is justified with low cost and easiness in processing, and the above-mentioned new trends in materials manufacturing further

expand the utilization fields, lower the expenses and adverse environmental impacts of conventional construction approaches.

Agriculture

The literature documents numerous studies on the application of CFA in soil amelioration processes as an agent for different purposes. The advantage of CFAs in the agricultural sector is their physical and chemical properties that allow controlling and adjusting the pH level depending on surrounding conditions. CFA consists of chemical elements that typically present in soil that includes macro- and micronutrients, namely Ca, K, P, Mg, Zn, Fe, S, Cu, Mn, Co, Mo and B which in turn expands the potential of CFAs to be utilized in soil amelioration [37]. As mentioned in previous sections, CFAs have different chemical compositions: Class F fly ashes has a lower content of CaO, while Class C fly ash has higher CaO amount. It is commonly known that most of the crops require an appropriate pH level that varies from alkaline to acidic phase. For instance, if the soil needs an alkaline pH level to grow crops, CFAs enriched with Ca, Na, Al and hydroxyl ions could be placed to raise the pH, which is explained by the gradual release of these ions into soil environment [80].

One study reports the increase of pH up to 2.3 points when CFA derived from coal containing the equivalent value of 2.43% $CaCO_3$ [81]. According to Jala and Goyal [82], the CFA-enriched soil system that experienced Ca to Na exchange, preserved the friability with subsequent positive vegetative grown. This is especially important when soil fertility is low and requires additional amelioration approaches. A comprehensive study on the effect of CFAs for soil amendment demonstrated that both pH and biomass amount increased after application of fly ash [83]. Another study examined that CFA also allows controlling the amount and leaching of inorganic and organic phosphorus in soil that further expands the benefits of utilization. Innovative applications of CFAs include an ornamental plant production [84,85] and insecticide applications [86,87].

Ceramic production

The vitrification technology, where the waste material is converted into a new value-added raw material becomes popular in the last decade. CFA is a promising candidate material that could be used for the production of ceramics [37]. CFA could be used for manufacturing of glass and ceramics without adding additives and almost without prior treatment [88].

In some cases, a mixture of CFA with conventional raw materials demonstrates enhanced physical and mechanical properties that allow to reduce the costs and improve the properties [89]. Jing *et al.* [90] manufactured ceramic granules using CFA, clay, and diatomite and used them in trickling filters. The results showed that newly prepared granules possess high porosity and large pore area that is suitable for biofilters. Kockal [91] studied the effect of CFA addition and sintering conditions on the body of ceramic tiles, which indicated that CFA enriched ceramic tiles show comparable properties as of commercial ceramic materials. There are many studies on CFA utilization as a replacement for kaolinite in the production of ceramic cordierite [92,93], pressed ceramic tiles [94] and brick [95,96].

Materials production and recovery

CFA could be recycled for the production of various composite materials. For example, CFA containing aluminum alloy composites produced by stir casting method demonstrated comparable hardness, elastic moduli and improved wear abrasive resistance, which allows the composites to be applied for manufacturing of pulleys, oil pans and valve covers [97]. The composites produced from a combination of nickel and CFA was found to be enhanced wear resistant rather than simple nickel coating. The superior performance of composite is considered to be due to the excellent bonding between CFA particles and nickel [98]. Another aspect that is important when fabricating composites is the density of the material, which usually should be light and strong. In such cases, CFA could be used to reduce the overall density of metal composites, which usually possess a higher density, with cenospheres (hollow particles) that present in CFA that could add advantageous properties as improved buoyancy, insulation, reduced shrinking module and warpage values [99].

CFA is also used for the production of mullite. Ohtake *et al.* [100] for example heated CFA enriched with gamma alumina up to 1400ºC and produced synthetic mullite with 80% yield. The properties of sintered synthetic mullite were comparable with commercial mullite. Similar studies carried out by Hwang *et al.* [101] also show that high-quality mullite could be produced from CFA and alumina upon conventional sintering at 800-1000°C combined with microwave treatment. It is interesting to note that microwave-assisted sintering produced more dense and strong material with a crystalline mullite content [102].

Materials recovery is another field of application of CFAs. According to literature, CFA could be a source of valuable metals as Ge, Ga, V, Ti and Al [9]. These metals are important

because they could be applied for manufacturing of diodes, infrared optics, photovoltaics, and other optoelectronic devices that are in high demand. Ge, for example, could be recovered from CFA by leaching followed by separation from other elements that include precipitation, distillation, flotation, complexation, solvent extraction and other approaches [9]. Ga is another metal that could be recovered from CFAs, which is 6-10 folds higher in amount than in parent coal due to enrichment after combustion [9]. This metal might also be leached out by using strong acids followed by a two-step solvent extraction [103].

Recent studies report that CFA that is processed over arc-typed reactor might produce up to 90% of iron and ferrosilicon alloy with Si content of up to 40% [104]. Chromium could be recovered from CFA upon acidic conditions using packed bed CFA pellets with kaoline used as a binder [99]. Silica and alumina extraction is also considered as potential materials to be recovered from CFA. Silica is usually recovered from CFA in an amorphous form, while alumina could be recovered in the solid state in the form of alpha or gamma alumina [105].

2.2. Mercury and iodide contamination

2.2.1. Mercury: speciation and contamination

Mercury is one of the most toxic and hazardous heavy metals found in nature. It is commonly used in many industries, such as electronics, paper, and pulp manufacturing, metallurgy, polymers production, pharmaceutical, oil refinery and others [106,107]. The worst scenario of the waste mercury generation is that after being used it is usually discharged to water resources. Mercury could exist in three oxidation states, +1 as in HgCl, +2 as in $HgCl_2$ and +4 as in HgF_4, the latter state is identified in exceptional conditions [108]. The widely spread compound form pf this metal is mercury (II) chloride that is typically used in polyvinyl chloride production and exists as Hg^{2+} form in the aqueous environment.

Mercury might also bind with organic compounds, as in highly toxic methylmercury (CH_3Hg). One of the unique and unfortunately negative sites of Hg is the capability of volatilization, persistence, and bioaccumulation in different food products, animals and even in human body. The organic form of Hg has a bio-accumulative property, which could accumulate in high concentrations in fish, shellfish, and animals that eat fish [109]. The adverse effects of Hg inhalation and exposure to Hg-containing compounds include negative

impacts in the immune system, disorders, and malfunctions of human organs, such as brain, kidneys, heart, and lungs [110,111]. More recently it has been identified that children and unborn babies, who are exposed to Hg or fed with Hg-containing food could have adverse effects, namely destruction of the nervous system and decrease of intellectual quality [112].

According to literature, more than 100 000 kg of Hg was produced due to human activities and discharge from various industries, annually [108]. The power stations that mostly use different types of coal has hugely contributed to the current total Hg emissions [108]. Both gaseous and aqueous phase Hg have mainly produced from these coal-fired power plants [113]. The recent studies on Hg contamination report that all forms of Hg, including the metallic mercury (Hg^o), the ionic form of mercury (Hg^{2+}) and organic mercury (CH_3Hg), have made their way to the environment and human health [114]. Currently, the pollution with Hg and its species is widely spread and could be detected in water resources, rocks, soil and even in air [111,115]. In 2013, after the catastrophic incident in Japan [116], the Minamata convention was designed to preserve the human health and environment that regulates the Hg-containing products and apply stricter emission standards.

As mentioned previously, Hg is a bio-accumulative, toxic and hazardous metal that may harm the human health and environment, and may exist both in water and air. Therefore, researchers from all over the world are trying to resolve this issue and find the solution of remediation of Hg from water and flue gas. According to the literature, one of the efficient ways of removal is by applying adsorption methods due to its convenience and practicality among other existing separation technologies [108]. The recent year studies demonstrate that Hg^{2+} removal by this separation approach has been improving.

2.2.2. Iodide: isotopes and contamination

The commonly known and used isotopes of iodine (^{127}I) and the ionic form of it (I^-) is not potential harm to human and environment. It is generally used as an vital precursor of iodinated products applied for the disinfection of drinking water [34]. The issues arise if the radioactive isotopes of iodine, such as ^{129}I and ^{131}I are formed, which could readily be dissolved in water and sublimated in air by causing various harms to the ecosystem [34,117].

The continuous demand for energy throughout the world expanding the use of nuclear energy, which inevitably produces various radioactive wastes, including radioactive isotopes

of iodine that is discharged and used in uranium fission [118]. The requirement for proper utilization of radioactive waste rose globally after the nuclear power accidents in Japan, which caused the emission of 1.5×10^{17} Bq of ^{131}I. The earlier disaster in Ukraine caused the discharge of 1.76×10^{6} TBq of iodine, which in turn was the source for radioactive I^- that drastically harmed the environment [117]. The radioactive isotopes of iodine may cause long-term risks owing to their prolonged half-life. For instance, ^{129}I and ^{131}I can stay in the ecosystem for approximately 16 million years and 8 days, that might negatively affect the human metabolic processes for an extended duration [117,119,120].

It is important to emphasize that both a radioactive and non-radioactive iodine could easily be transformed into species of iodide, iodate, and triiodide in water solutions. Thus, it requires the knowledge of the state of the species in the aquatic environment. Comprehensive research conducted by Kireev and Shnyrev [121] indicates that UV-Vis spectroscopy might be used for qualitative and quantitative analysis of these species. Similarly, other research groups applied the UV-Vis to measure the I^- concentration in removal studies [34,117,118,122]. The transformation of species might follow a single or combination of these chemical reactions depending on environmental conditions [121]:

$$I_2 + H_2O \rightarrow HIO + H^+ + I^- \quad (2.1)$$

$$3HIO \rightarrow 3H^+ + IO_3^- + 2I^- \quad (2.2)$$

$$I_2 + I^- \leftrightarrow I_3^- \quad (2.3)$$

$$HIO_3 \rightarrow H + IO_3^- \quad (2.4)$$

2.2.3. Adsorbent development for removal of mercury and iodide

There are several existing purification approaches that are typically applied for removal of Hg^{2+} and I^- from aqueous media, particularly removal *via* physical and chemical adsorption. The ionic form of Hg^{2+}, for example, is removed from simulated water using adsorbents produced from wastes. Synthetic zeolite (Linde type A) derived from CFA was used for Hg^{2+} remediation under different dosage and concentration [21]. As it was expected, the synthetic zeolite indicated a linear dependence on adsorbent dosage, demonstrating an improved removal when a higher amount of adsorbent is used. The optimum conditions allowed to remove 94% of Hg^{2+} from solution using CFA based zeolite that was comparable with commercially used carbon samples.

Table 2.4. Adsorbents for the removal of Hg^{2+} from aqueous phase

Adsorbent type	Concentration of Hg^{2+} [g/m^3]	Volume of Hg^{2+} [cm^3]	pH	Adsorbent dosage, [g]	Removal of Hg^{2+} [%]	Reference
Activated carbon from organic sewage sludge	200	100	5.0	4-10	83-100	[123]
Weathered coal	3	100	6.0	0.8	>99	[124]
Chitosan-coated magnetite NPs	6.2	50	5.0	0.67	>99	[125]
Ag/graphene	100	100	5.0	0.1	98	[126]
Ornamental rock solid waste	10	125	2-8	2	>90	[127]
Flower-like titanate nanomaterial	100	50	5.0	0.01	98	[128]
LTA CFA derived zeolite	10	10	2.5	0.1-1.0	94	[21]
ZSM-5-mesoporous/HAPT	2	100	2-12.5	0.02	94	[129]
Ag-X CFA derived zeolite	13.2-575	100	5-6	10	90	[16]

A similar investigation was carried out by Wdowin *et al.* [16], where authors utilized CFA derived zeolites ion-exchanged with silver. The results of the research revealed that silver-exchanged zeolites had a lower surface area due to partial blockage of pores by silver. It decreased from 260 m^2/g for pristine zeolite to 203 m^2/g for silver-exchanged zeolite. However, the removal of Hg^{2+} was on average 90% for both pristine and modified samples. Some research groups have investigated the utilization of activated carbon from sewage sludge, weathered coal, graphene supported silver, commercial zeolites, titanate-based nanomaterial, and ornamental rock waste, which are summarized in Table 2.4.

It should be noted that most of the Hg^{2+} removal experiments were conducted at pH 4.0 or higher, which in combination with a high Hg^{2+} concentration may result in insoluble Hg complexes, rendering the adsorption results uncertain. Moreover, the studies have not covered a detailed analysis of the removal mechanism that is open for further research.

The I^- has also been removed from aqueous media by means of various porous and non-porous adsorbents doped with metal nanoparticles (NPs) and metal oxides. A classic example of adsorbent that is usually used for remediation purposes is activated carbon (AC). Hoskins and Karanfil [130] examined the adsorption capacity of silver-impregnated AC. The authors varied the silver content (0.05wt.% and 1.05wt.%) impregnated into AC, pH (3.0, 7.0 and 8.0) and studied the stability of adsorbed iodide by conducting leaching experiments. According to their hypothesis, the I^- is sequestrated from water *via* the precipitation reaction of Ag^+ and I^- in the form of AgI. The leaching experiments showed that an adsorbed iodide (118 μmole/g) remained in AC pores that suggested 1:1 ratio of Ag^+ and I^-.

Table 2.5. Adsorbents for the removal of I^- from the aqueous phase

Adsorbent type	Surface area [m^2/g]	Temperature [ºC]	pH	Adsorption capacity [mg/g]	Ref.
Silica-coated magnetite NPs	-	-	7.0-8.0	140.84	[131]
Micro/nanostructured bismuth oxide	26.6	20	-	285	[132]
MIL-101(Cr)-SO_3Ag	-	30	7.5	244.2	[133]
Bimetallic AgCu/Cu2O hybrid	-	25	3.0	65.9	[134]
AgII-doped MIL-101	1045	25	3.0	270	[135]
Chinese soils	-	25	5.05	222.2	[136]
3D Ag_2O–Ag/TiO_2	153.7	25	-	207.6	[137]
Montmorillonite-magnetite NPs	148.8	35	3.0	322.42	[117]
Ag_2O grafted titanate nano alumina	143	-	-	428	[118]

More recently, an I^- removal was studied by organically modified montmorillonite doped with magnetite NPs that was synthesized *via* co-precipitation method [117]. The research outcomes revealed an adsorption capacity of 322.42 mg/g under optimum conditions that

was confirmed with response surface methodology. Table 2.5 summarizes the most common and recent adsorbents utilized for I^- remediation with general information of experimental conditions applied.

However, the main drawback of these studies is that they have not mentioned the partial dissolution of precipitated or adsorbed AgI into solution and have not confirmed the formation of AgI *via* microscopic and chemical characterization methods, such SEM, TEM, and XRF. This entails a further detailed examination of the mechanism of adsorption and proper quantification of adsorbed and leached I^-.

2.3. Synthesis of zeolites from coal fly ash

One of the most attractive and desirable transformations of CFA into a value-added product is the synthesis of zeolitic sorbents. The main reason behind its possible utilization is the similarity of CFA composition and physical-chemical properties to naturally occurring zeolites from volcanic materials [18]. The research into synthetic zeolite production boomed after the first experiments carried out by Holler and Wirsching back in 1985 when scientists used CFA as a raw material for synthetic zeolite manufacturing [138]. Since then there have been numerous articles published and patents filed in the world on using CFA for production of zeolites. The elemental composition of zeolite and CFA is comparable, yet the primary distinction separating those two is the structure of crystalline. CFA is normally formed of an amorphous structure, wherein a zeolite has a well-defined crystalline structure [139]. Figure 2.7 shows the crystal structures of two commonly known zeolite frameworks.

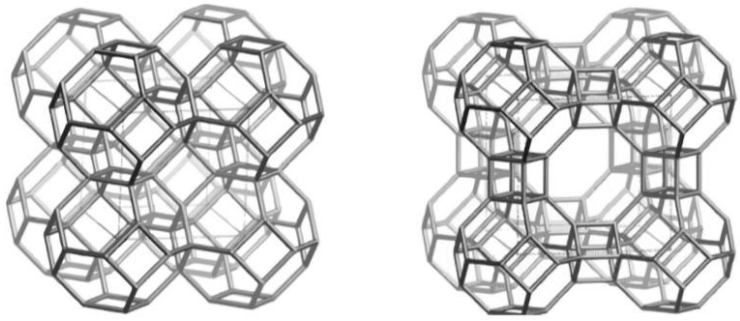

Figure 2.7. Structures of common zeolites: Sodalite (left) and Linde type A (right)

Table 2.6. Common porous structures produced from CFA

Zeolite type	Formula	JCPDS code
NaP1 zeolite	$Na_6Al_6Si_{10}O_{32}\cdot 12H_2O$	39-0219
Phillipsite	$K_2Al_2Si_3O_{10}\cdot H_2O$	30-0902
K-chabazite	$K_2Al_2SiO_6\cdot H_2O$	12-0194
Zeolite F Linde	$KAlSiO_4\cdot 1.5H_2O$	25-0619
Herschelite	$Na_{1.08}Al_2Si_{1.68}O_{7.44}\cdot 1.8H_2O$	31-1271
Faujasite	$Na_2Al_2Si_{3.3}O_{8.8}\cdot 6.7H_2O$	12-0228
Zeolite A	$NaAlSi_{1.1}O_{4.2}\cdot 2.25H_2O$	43-0142
Zeolite X	$NaAlSi_{1.23}O_{4.46}\cdot 3.07H_2O$	39-0218
Zeolite Y	$NaAlSi_{2.43}O_{6.86}\cdot 4.46H_2O$	38-0239
Perlialite	$K_9NaCaAl_{12}Si_{24}O_{72}\cdot 15H_2O$	38-0395
Analcime	$NaAlSi_2O_6\cdot H_2O$	19-1180
Hydroxy-sodalite	$Na_{1.08}Al_2Si_{1.68}O_{7.44}\cdot 1.8H_2O$	31-1271
Hydroxy-cancrinite	$Na_{14}Al_{12}Si_{13}O_{51}\cdot 6H_2O$	28-1036
Kalsilite	$KAlSiO_4$	33-0988
Tobermorite	$Ca_5(OH)_2Si_6O_{16}\cdot 4H_2O$	19-1364

There have been continuous studies in the search for better crystallinity, yield along with a suitable cation exchange capacity (CEC), high specific surface area, efficient pollutant removal, and viability for production. Over the past years, numerous research on the synthesis of zeolites from CFA polished several commonly applied methods, such as conventional alkaline hydrothermal treatment, fusion followed by hydrothermal treatment, microwave-assisted production, ultrasound-assisted synthesis, and a multi-step approach. Table 2.6 summarizes some of the research work carried out on the synthesis of zeolites and other neomorphic phases from CFA with Joint Committee Powder Diffraction Standard (JCPDS) codes for XRD diffraction [139].

2.3.1. Hydrothermal treatment

One of the extensively employed approaches for production of zeolite is the hydrothermal conversion by means of alkaline solutions [12,15,19]. According to this technique, the raw

CFA is dissolved in the alkaline solution to extract aluminate and silicate constituents and then go through elevated temperature treatment to produce zeolitic crystals. There are four main steps during zeolitization of CFA: first, a dissolution of Si and Al, then a condensation followed by nucleation and crystallization [8]. The ratio of aluminate or silicate is generally varied to obtain a desired type of zeolite. Depending on reaction conditions as temperature, pressure, reaction time, Si/Al ratio, alkaline solution, pH, and seeding of initial CFA this method allows producing numerous synthetic zeolites, such as zeolite X, zeolite P [1,140], analcime [2,141], chabazite [142] or hydroxyl-sodalite [143,144]. Murayama *et al.* [145] studied the effect of alkali solution nature on the mechanism of zeolite formation by varying the activation agent (NaOH, KOH, Na_2CO_3, NaOH/KOH, Na_2CO_3/KOH). It was identified that sodium ions in alkali solutions improved the zeolite synthesis, while the co-existence of potassium with sodium ions decreased the yield of production.

It should be noted that there some drawback of conventional hydrothermal treatment, such as the partial dissolution of Si derived from CFA and a lower rate of dissolution of Al as compared with Si, which is due to low solubility and inertness of mullite containing in CFAs [37]. These factors slightly restrict the application of this method since it might not fully dissolve the Si and Al content present in raw CFA, thus producing zeolites with relatively low yield.

2.3.2. Fusion-assisted hydrothermal treatment

In the search for improvement of yield and crystallinity of zeolites produced from CFAs, Shigemoto [146] suggested using a fusion step before conventional hydrothermal treatment. The samples of CFA with sodium hydroxide (NaOH) were fused at 550ºC prior to conventional elevated temperature treatment without stirring. This novel approach enabled to produce synthetic zeolite Na-X with a high conversion rate, CEC, and improved crystallinity. A similar synthetic route was investigated by Berkaut and Singer [147], where authors fused a NaOH and CFA at slightly elevated fusion temperature 170-180ºC to produce aluminosilicate gel, which then followed by hydrothermal treatment at 100ºC to yield a synthetic Na-P zeolite without aging and Na-X zeolite after 12-hour of aging. Another research group also used the pre-fusion step before hydrothermal treatment of CFA to produce zeolite P and faujasite [148]. The authors emphasized that the fusion-assisted

method improved the dissolution of Si and Al content from parent CFA, hence enhancing the yield of zeolite synthesis.

The literature generally supports that a pre-fusion step improves the traditionally used hydrothermal treatment that has been confirmed with numerous research. The main drawback could be the elevated temperature treatment (500-600 ºC) that adds up the costs of the method and has to be considered before large-scale production.

2.3.3. Sonication approach

Application of ultrasound energy is another emerging approach in the synthesis of zeolites from CFA. The major advantage of this energy is that it enables to accelerate the dissolution of Si and Al content in CFA, thus facilitating a faster poly-condensation process and transition of semi-crystalline phase into crystalline phase [8,149,150]. There are number of research, where authors applied an ultrasonic treatment on the synthesis of zeolites from CFA. More recently, Woolard *et al*. [151] produced a synthetic hydroxyl-sodalite using CFA, while Musyoka [152] synthesized a zeolite-A through the combination of ultrasound and microwave energies. The latter observed that a sonication for 40 minutes before conventional hydrothermal treatment improved the crystal formation of zeolite and considerably reduced the reaction duration. Wang and Zhu [153] applied ultrasound energy along with conventional hydrothermal incubation of CFA to produce zeolite. According to their research findings, the surface area and adsorptive properties were comparatively higher and the treatment time was dramatically decreased in comparison with synthesis that does not involve sonication.

It is obvious from the literature that ultrasonic energy facilitates the crystal growth and lowers the required synthesis temperature, which in turn reduces the costs of production. Moreover, there is a possibility to increase the crystallinity of zeolites *via* sonication as it allows to saturate the crystalline phase during the nucleation stage.

2.3.4. Microwave-assisted synthesis

Another approach to improve the conventional hydrothermal treatment is the application of microwave for a short time during synthesis. For instance, Querol *et al.* [154] tried to use both conventional and microwave irradiation and were able to produce zeolite-A in a comparatively faster mode. According to the results, the yield of zeolite was similar,

however, the microwave-assisted method allowed to reduce the time required for activation step from a typical 24-48 hours used in the traditional approach to 0.5 hours. Similarly, another group of scientists produced zeolite Na-P1 from CFA in a microwave-irradiated closed-oven that also allowed to optimize the synthetic route [155]. Generally, the zeolite formation *via* this approach could be separated into three phases: firstly, the dissolution of Si and Al content in CFA; secondly, the development of intermediate aluminosilicate gel; and lastly, the transformation of gel into a zeolite and growth of zeolitic crystals [156].

Generally, it could be established that the major advantages of microwave-assisted approach are the facilitation of reaction activation time and the possibility to produce relatively smaller zeolite crystals. In addition to this, the lessening of total synthesis time allows cutting the costs and might be economically feasible for large-scale production of CFA derived zeolites.

2.4. Applications of coal fly ash derived materials

2.4.1. Heavy metals removal

One of the main application fields of synthetic zeolites produced from CFA is remediation of heavy metals from water. Penilla *et al.* [157], for instance, produced a synthetic zeolite from a Spanish low-lime containing CFA of Class F using conventional hydrothermal treatment with NaOH as an activation agent. The results revealed that the synthetic zeolites P and analcime of GIS framework were the primary species of production, which allowed to remove all tested metals (Cs, Pb, Cd, and Cr) from mine waters to some extent. Another study observed that hydrothermal conversion of CFA into zeolites could also be used for removal of Hg^{2+} and Pb^{2+} cations [158]. According to the research outcome, CFA derived zeolite was able to remove 30% and 95% of mercury and lead from water, correspondingly.

Woolard *et al.* [159] carried out a comparative examination of two types of synthetic zeolites derived from CFA. The authors produced synthetic zeolites Na-P1 and hydroxy-sodalite, then tested both zeolites for retention of Pb^{2+} from the water. The results demonstrated that synthetic zeolite Na-P1 is more effective in removing lead ions than hydroxy-sodalite. Similar studies on removal of Pb^{2+} from water using CFA-based zeolites could be found elsewhere [160–162]. Some studies include a pilot-scale production of synthetic zeolites from CFA that was applied for wastewater treatment from heavy metals, such as Ni^{2+}, Cd^{2+},

Zn^{2+}, Pb^{2+}, Cu^{2+} and Cr^{3+} [140,163]. The results of the pilot-scale testing showed that the CEC of synthetic zeolites varies from 68-260 meq per 100 g of sample. Moreoever synthetic zeolites have also been reported to remove metals, such as Ar [164], Cu [14,165], U [166], Ni [46,47], Co [167,168], Zn [165,169].

2.4.2. Inorganic and organic pollutants removal

Some research groups applied CFA-derived zeolites to remove inorganic pollutants. Zhang *et al.* [170], for example, used synthetic faujasite to remediate ammonium from water solutions. They found out that adsorbent is effective and demonstrate acceptable kinetics and thermodynamics. Another study carried out a simultaneous removal of ammonium and phosphate by utilizing synthetic zeolites produced by fusion method and pre-saturated with cations, such as Al^{3+}, Ca^{2+} and Fe^{3+} [171]. The results revealed that the removal efficiency of inorganic pollutants has been improved by the enrichment of cations. Similarly, Zhang *et al.* [172] observed that ammonium and phosphate removal using synthetic zeolite treated with sulfuric acid enhances the adsorption efficiency.

CFA derived synthetic zeolites have also been explored for remediation of organic pollutants. Bandura *et al.* [173] studied the removal of aromatic hydrocarbons, such as benzene, toluene, and xylene, so-called as BTX, by means of synthetic Na-X zeolite. According to authors the improved adsorption capacity of zeolites are linked with the typical framework of faujasites that usually have wide channels suitable for BTX pollutants. The same group has examined another synthetic zeolite Na-P1, which removed 99% of xylene, 77% of toluene and 35% of benzene [174]. These results led to the assumption that the adsorption capacity of BTX is inversely related to the degree of hydrophobicity and molecular weight of pollutant. Synthetic zeolites functionalized with alkyltrimethoxysilane groups have also found application in oil spill cleanup [175]. The alkyl chains facilitated the floating effect in water owing to their hydrophobicity that in turn allowed adsorbing the spilled oil from the surface of the water.

2.4.3. Molecular sieves

The porous structure of synthetic zeolites facilitates the capture of different pollutant gasses, namely CO_2, SO_2, volatilized Hg, and NH_3. Scrinivasan *et al*. [176] produced synthetic zeolites X, Y and Na-P1 using a Class F CFA. They examined the produced zeolites for the

capture of SO_2 from a stack gas that initially contained 2000 mg/L SO_2. The results revealed that the optimized CFA based synthetic zeolite demonstrated an adsorption capacity of 6-7 mg SO_2 per 1 g of adsorbent. Similarly, Querol *et al.* [177] studied the capture of CO_2 and SO_2 by utilizing CFA derived zeolites. They determined that the adsorption capacity of produced zeolites reached 74 mg of CO_2 per and 297 mg SO_2 per 1 g of adsorbent. The group also investigated the adsorption of SO_2 and NH_3 using synthetic sodalite and analcime [139]. The maximum adsorption capacities of these two gases were as low as 1-6 mg per 1 g of adsorbent, which was mainly due to the small or tight size of channels (about 2.3 Å) rather than required minimum diameter. Principally, the adsorption capacity of adsorbents used for flue gas purification and separation depends on the size of channels and molecular size of targeted species. Figure 2.8 shows the size of pores of some commonly known synthetic zeolites derived from CFA.

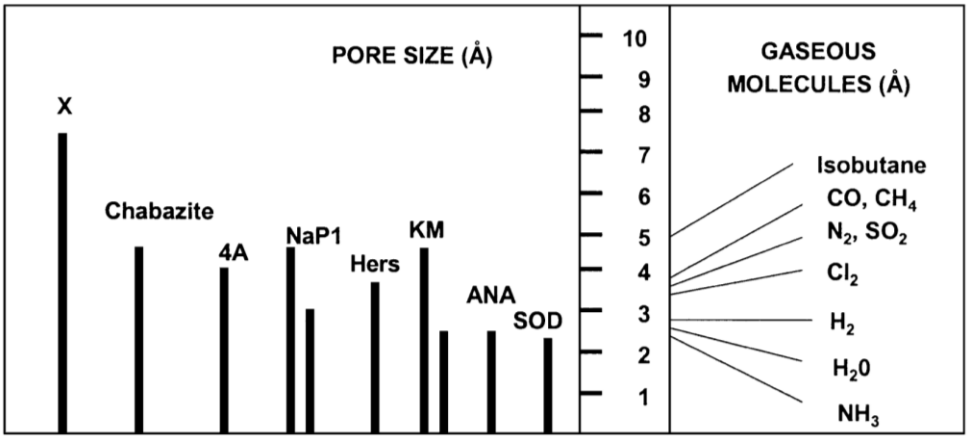

Figure 2.8. The pore size of synthetic zeolites (in Å) and molecular sizes of gases

Another study conducted to examine the adsorption of CO_2 using CFA based zeolite report adsorption of 52 mg CO_2 per 1 g of adsorbent [178]. Synthetic zeolites could be utilized for adsorption of hazardous metals like Hg from flue gas. Wdowin *et al*. [22,23] examined two different synthetic zeolites derived from CFA impregnated with Ag NPs to capture gaseous Hg from the flue gas stream. According to results, the impregnation of silver into the zeolite matrix significantly improved the adsorption capacity with Hg breakthrough varying between 15-40%. The authors also reported that Hg adsorption from a flue gas stream depends on sorbent grain (powder or granulated), the flow rate of gas, temperature and contact time, which requires an optimization study.

2.4.5. Catalysis

An alternative application field of synthetic zeolites produced from CFA is catalysis, particularly zeolite as a substrate for catalysts. A recent study conducted by Fotovat [179] demonstrated that Co NPs impregnated synthetic zeolites could successfully be applied in Fischer-Tropsh reaction. The synthesis reaction carried out with pristine zeolite and CFA based zeolite loaded with Co NPs showed a comparable activity. Rios *et al.* [180] examined the use of synthetic Na-X zeolite modified with ammonium and hydrogen ions in catalytic cracking reactions used for a petroleum refinery. Similarly, Yamamoto [181] mentioned that an ion exchange of zeolites structure with dissolved cations could enhance the performance of catalysts. The author describes those synthetic zeolites ion-exchanged with transition metal ions have been used as catalysts in various organic reactions. For example, the synthetic zeolites were used in polypropylene pyrolysis that was mentioned in research works carried out by Nam *et al.* [182] and Kim *et al*. [183].

The literature mentions several major utilization fields of synthetic zeolites produced from CFAs. The benefits of synthetic zeolites derived from CFAs are the low cost and diversity, which could enable to produce numerous types of zeolites depending on target pollutant and contamination conditions, such as pH, temperature and dosage. Some of these investigations went beyond the lab-sale and reached a pilot-scale production, testing, and feasibility studies. It is clear from the literature that the primary interest of scientists is the application of CFA based zeolites to entrap and remove heavy metals from gaseous and aqueous media, which has already reached some degree of feasibility.

CHAPTER 3

MATERIALS, SYNTHESIS, AND CHARACTERIZATION

3.1. Materials

All reagents in this work were of scientific grade and used as obtained without prior purification. Characteristic CFA specimens, particularly Ekibastuz, Karazhyra, and Maikuben CFAs, were accumulated from the electrostatic precipitators of Astana and Oskemen city power plants (Kazakhstan, 252 MW). Silver nitrate ($AgNO_3$, 99.8%) and sodium hydroxide pearls (NaOH, 99.5%), mercury (II) chloride ($HgCl_2$, 99.7%) mercury (II) nitrate ($Hg(NO_3)_2$, 99.8%), mercury (II) sulphate ($HgSO_4$, 99.9%), mercury (II) acetate ($Hg(COO)_2$, 99.9%) were provided by Sigma-Aldrich, sodium borohydride ($NaBH_4$, 99.5%) and potassium iodide (KI, 99.8%) was acquired from Fischer-Scientific (UK). Concentrated and dilute solutions of hydrochloric acid (HCl) and sodium hydroxide (NaOH) was used for pH level adjustments that are required for adsorption analyses.

To clarify the notation of raw and derived substances, following code names were given for CFAs, their derived synthetic zeolites, and nanocomposite materials: Ekibastuz, Karazhyra, and Maikumen CFAs were expressed as E-CFA, K-CFA, and M-CFA, respectively. The synthetic zeolites (ZFA) derived from corresponding CFA samples expressed as E-ZFA, K-ZFA, and M-ZFA; wherein the nanocomposites with Ag NPs were marked as Xwt.%-Ag-Y-ZFA, where X is the quantity of Ag NPs and Y is the variety of synthetic zeolite used for nanocomposite production. The reduced forms of zeolites that followed the same treatment procedure without adding silver nitrate solutions labelled as Y-R-ZFA.

3.2. Synthesis of zeolites

Synthetic zeolites from various Kazakhstani CFAs (E-CFA, K-CFA, and M-CFA) are produced *via* the conventional alkaline hydrothermal treatment approach. Sodium hydroxide (NaOH) was taken as an activation agent, as it enables to achieve higher conversion performance under the identical laboratory conditions compared with potassium hydroxide (KOH) or sodium carbonate (Na_2CO_3). The general procedure of zeolite synthesis *via* alkaline hydrothermal treatment is as follows. A 50 g of as received dry and homogenized CFA was placed in a 1L heavy-walled chemically stable reactor and gradually heated at

110°C with a concentration of activation solution (NaOH) of 3 mole/L. The reaction duration was fixed at 48 hours and mixing was constantly applied at 125 rotations per minute (rpm) for all trials. Following that, the mixture was filtered and thoroughly washed with deionized water several times until the pH of the filtered solution was close to a neutral value (pH of 6.5-7.0). After that, the obtained synthetic zeolite was dried at 70^{o}C overnight and stored in a tightly closed bottle for characterization and following experiments.

3.3. Optimization of zeolite production

3.3.1. Factorial analysis of zeolite synthesis from coal fly ash

There are certain parameters that influence the zeolitization process, which include an alkali concentration, reaction time and temperature, loading ratio (volume of the alkali solution to the weight of CFA, i.e, liquid to solid ratio, L/S), and Si/Al ratio in CFA. Depending on those stipulations it is probable to acquire various purity and sort of synthetic zeolites, such as zeolite A, zeolite Na-P, sodalite, etc. The open data in the literature on the hydrothermal alteration of zeolites from CFA to highlight the impact of method parameters on the yield of production are summarized in Table 3.1.

Table 3.1 shows strong, non-monotonic, and to some extent, the stochastic interdependence of yield on method parameters. For instance, an insignificant variation in loading ratio from 2 to 1.25 greatly enhances yield from 20% to 75% (as in points No. 1 and 7). Though, rising the loading ratio to 18 results in conversion to 50% (as in points No. 1 and 15). There are numerous other correlations that can be performed to emphasize random performance. The values described in the literature are all empirically learned and hence might be constrained to mathematical inaccuracies, but it is considered that all the values are repeatable.

To produce synthetic zeolites and investigate the influence of factors, E-CFA experienced alkaline hydrothermal processing at 90-110°C, applying NaOH with concentrations of 1 or 3 M as an activation solution, in a 1L heavy-walled glass reactor. The incubation duration was altered from 24 to 48 hours and a mixing rate was fixed constant at 125 rpm for whole trials. After a set duration, the mix-up was filtrated and rinsed many times till NaOH was not identified. Factorial analyses were performed employing three parameters, specifically the reaction temperature, reaction time, and concentration of an alkaline solution, that

entailed the design of 8 experiments, as displayed in Table 3.2, to examine the impacts of the reaction parameters on the amount of zeolitic phase growth and development.

Table 3.1. The effect of process conditions on hydrothermal synthesis of synthetic zeolites

No.	Conc.[a] (M)	Time (h)	Temperature (°C)	L/S[b] (ml/g)	Si/Al	Conv.[c] %	Ref.
1	1	24	80-130	2	1.29	20	{d}
2	1	48	122-166	2	1.29	60	{d}
3	1	48	126-192	2	1.29	80	{d}
4	1	48	100-130	2	1.29	75	{d}
5	2	24	92-114	1.25	1.29	75	{d}
6	2	24	100-110	1.25	1.29	75	{d}
7	2	24	90-100	1.25	1.29	75	{d}
8	2	48	80-130	1.25	1.29	65	{d}
9	2	22	125-187	2	1.29	60	{d}
10	2	72	120-190	2	1.29	80	{d}
11	2	72	130-160	2	1.29	80	{d}
12	2	24	131-174	2.5	1.29	65	{d}
13	2	48	110-180	2.5	1.29	75	{d}
14	2	48	110-160	2.5	1.29	60	{d}
15	1	24	90	20	1.44	19.8	{e}
16	1	24	110	20	1.44	45.3	{e}
17	1	48	90	20	1.44	48.3	{e}
18	3	24	90	20	1.44	39.6	{e}
19	1	48	110	20	1.44	47	{e}
20	3	24	110	20	1.44	55.9	{e}
21	3	48	90	20	1.44	35.5	{e}
22	3	48	110	20	1.44	78	{e}
23	0.5	24	150	18	2.9	44	{f}
24	1	24	150	18	2.9	50	{f}
25	0.5	24	150	18	2.7	44	{f}
26	3.5	24	150	18	2.7	21	{f}
27	1	24	150	18	2.7	60	{f}
28	2	24	100	18	2.7	17	{f}
29	3	24	100	18	2.7	48	{f}
30	3.5	24	100	18	2.7	35	{f}
31	3	24	75	20	1.88	50	{g}

a: Concentration of alkali; b: volume of the alkali solution to weight of CFA; c: Total conversion of CFA to zeolite; irrespective of the type of zeolite formed; d: As reviewed by Wang *et al*.[141], e: Our experiments; details mentioned below, f: Experiments by Cardoso *et al*. [184], g: Experiments by Derkowski *et al*.[165].

Table 3.2. Factorial analysis parameters applied in the production of ZFA from CFA*

Experiment No.	Concentration (M)	Time (h)	Temperature (°C)
1	1	24	90
2	1	24	110
3	1	48	90
4	3	24	90
5	1	48	110
6	3	24	110
7	3	48	90
8	3	48	110

*L/S = 20 ml/g and Si/Al = 1.44 are constant in all experiments

3.3.2. Fuzzy system architecture

The introduced fuzzy logic based system is further recognized as Takagi-Sugeno (TS) fuzzy system which was first presented by Takagi and Sugeno [185] and has been widely used in various purposes over disciplines. Typically, there are three principal building blocks which are required to be determined in generating a fuzzy based system. Fuzzification of antecedent and resulting variables is the first block, while construction of a rule-base, representing the correlation among variables, is another building block. Formulation of an inference mechanism to render numerical values of output or consequent variables is the third building block of the fuzzy systems. The fuzzy system originated during this research is farther described in terms of these building blocks in the subsequent section.

Fuzzification

Fuzzification is the method whereby crisp antecedent and consequent variables are defined as fuzzy variables. In the present investigation, there are five antecedent variables viz, molar concentration, temperature, time, mixture loading ratio (L/S), and Si/Al ratio. The output variable is the percentage of zeolite conversion (Conv.) from Table 1. First, the antecedent variables are transformed into fuzzy variables by applying fuzzy sets. Gaussian distribution is chosen for the shape of the Activation Functions (AFs) as they accommodate a smooth shift between AFs. Succeeding, the number of AFs and their parameters such as mean and standard deviation are determined. Number of AFs for i^{th} input (M_i), can be two or more depending on the precision of outcomes demanded. Nevertheless, the points of minimum

fuzziness (or center points of AFs shown by B and C in Figure 3.1) and standard deviations (σ_i) of AFs along with the series of variables (R_i) can be automatically calculated employing extreme values (i.e. minimum and maximum) of variables (v_i) while execution of the algorithm using Eq. (3.1-3.3).

$$R_i = (1.25 * \max(v_i) - 0.75 * \min(v_i)) \tag{3.1}$$

$$A_i = 0.75 * \min(v_i)\,;\; B_i = A_i + \frac{R_i}{(2M_i - 1)}; C_i = B_i + \frac{R_i}{(2M_i - 1)}; D_i = 1.25 * \max(v_i) \tag{3.2}$$

$$\sigma_i = R_i/(2 * (2M_i - 1)) \tag{3.3}$$

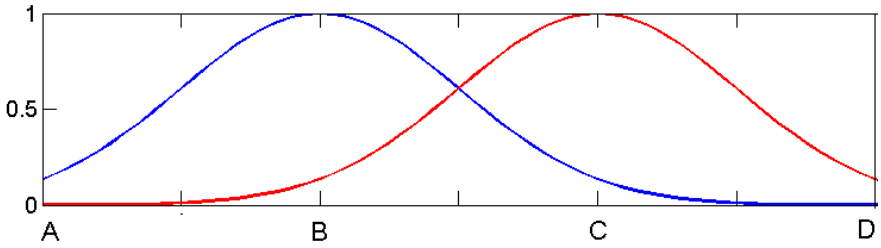

Figure 3.1. Minimum fuzziness points of a Gaussian AF

Heuristic models such as the currently considered model might be evaluated based on two parameters particularly, interpretability and accuracy. Unfortunately, these two parameters are conversely related and the authors usually have to trade off the accuracy for the purpose of interpretability. Consequently, in order to have enough interpretability and avoid overfitting of data, the antecedent variables are all defined using only two AFs as shown in Figure 3.1. The AFs, in order to achieve accurate values, are named as Low (L) and High (H).

The consequent variables are not defined in the beginning preferably these are acquired through the course of the algorithm. A set of real numbers is collected for consequent variables while applying a zero-order TS fuzzy system. Higher order fuzzy systems, which provide polynomial functions for consequent variables, are not examined in the present case due to their non-linearity and subsequent higher complexity. It is also noted that in Table 3.1, specific data points have a scale of values for temperature; and in such cases, an average value was used.

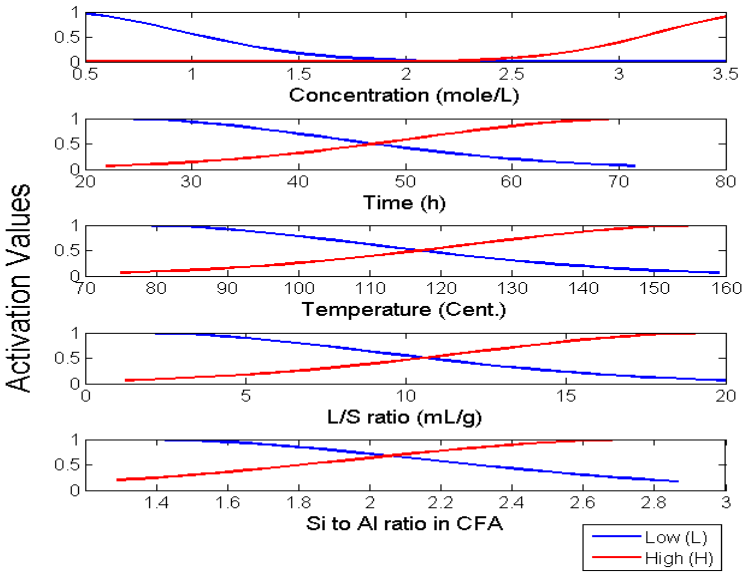

Figure 3.2. Fuzzification of antecedent variables of the fuzzy system

Rule-base Development

Throughout the design of fuzzy systems, development of a rule-base is an essential assignment which entails proficient expertise and accurate data interpretation. The rule-base of a TS fuzzy system correlates the fuzzy antecedent and crisp consequent variables applying *if-then descriptions* and has the resulting structure.

$$If conc.\,is\ low, time\ is\ high, \ldots\ldots\ldots then\ the\ output\ (CR)\ is\ y_i$$

Primarily, the overall number of rules (N_r) is resulting from the number of input variables (n) and AFs (m_k) by means of following the relation.

$$N_r = \prod_{k=1}^{n} m_k \tag{3.4}$$

Accordingly, in the existing system where there are five input variables and each of these is defined using two AFs, the total number of rules in the rule-base is 2^5=32 (see Table A1). Therefore, the set of consequent variables (y_i) should likewise have 32 real numbers for the present zero-order TS fuzzy system. The consequent variables (y_i) are identified by applying the pseudo-inverse operator in the inference mechanism block as described in the following section.

Inference mechanism

To estimate output conversion of zeolite ($Conv.$) from the fuzzy model for given inputs, a weighted average from all the individual rules is calculated and multiplied with the set of consequent variables. In fact, the calculation of output from the fuzzy model is a two-step scheme which is based on a weighted average defuzzifier [186]. First of all, degrees of fulfillment (w_i) for k^{th} input (I_k) is assessed from all the rules using (3.5-3.8). Here activations of input variables in 'Low' and 'High' AFs are given by $A_{kL}(I_k)$ and $A_{kH}(I_k)$ respectively and calculated using (3.5 and 3.6). Constant 'a' in the equations is given by $1/(\sigma\sqrt{2\pi})$, while e designates the Euler's number. The degrees of fulfillment (w_i) for i^{th} input from all the rules are calculated using a product operation (3.7). In the subsequent step, the final output ($Conv.$) is computed by means of a weighted average of the individual rule fulfillments using (3.8). P_{ik} is the selection vector which determines the activation function to be used in input k and rule i.

$$A_{km}(I_k) = ae^{-\frac{(I_k-\bar{I}_{km})^2}{2\sigma_{km}}}; \qquad where \quad m = L, H \tag{3.5}$$

$$A_k(I_k) = [A_{kL}\ A_{kH}]^T \tag{3.6}$$

$$w_i = \prod_{k=1}^{5} P_{ik} A_k(I_k) \tag{3.7}$$

$$Conv. = \frac{\sum_{i=1}^{N_r}(w_i.y_i)}{\sum_{i=1}^{N_r} w_i} \tag{3.8}$$

Here w_i are the degrees of fulfilment for an input from all the rules, and y_i as described in the preceding subsection, is a set of 32 real numbers, which is the consequent part of the rule-base and lacks to be obtained.

Moreover, it should be emphasized that the equation (3.8) might be altered as (3.9 and 3.10), where $\overline{w_i}$ as the normalized degree of fulfilment ($\frac{w_i}{\sum w_i}$).

$$Conv. = \overline{w_i}^T y \tag{3.9}$$

$$\text{Or } Conv. = [w_1\ w_2\ \ldots\ldots w_{32}] \begin{bmatrix} y_1 \\ y_2 \\ y_3 \\ \vdots \\ y_{32} \end{bmatrix} \tag{3.10}$$

Following if multiple experimental observations (of inputs and corresponding outputs) are available, equation (3.10) can be reflected concurrently to present a system of equations as shown in (3.11).

$$CONV = W * Y \tag{3.11}$$

The consequent vector (Y) be able to be acquired by a regression method. Typically, the regressor matrix (W) is non invertible, and consequently, its pseudo-inverse is applied to solve for Y (3.10).

$$Y = W^{-1} * Conv. \tag{3.12}$$

$$Y = (W^T * W)^{-1} * W^T * Conv. \tag{3.13}$$

By means of (3.12 and 3.13) a vector of consequent parameters could be acquired that will minimalize the error among the predicted $Conv.$ and the target $Conv.$ from trials.

3.3.3. Optimization of the fuzzy model

To start with, the parameters of the fuzzy system such as mean and standard deviation of the fuzzy AFs are determined by an intuitive approach. Yet, this type of system might not explicitly reproduce the zeolitization process and hence fuzzy system parameters are obliged to be tuned in order to optimize the fuzzy model for improved correctness. In other words, the fuzzy model requires to be optimized in such a way so that the prediction error from the model is decreased. Considering the parameters are tuned within their limiting values; it is a constrained optimization problem which involves multiple variables that may be non-linear in nature. The accessible information (set of inputs and zeolite yield) could be utilised to attune fuzzy parameters and generate the desired system model. The tuning of fuzzy parameters could be obtained by employing a gradient descent algorithm, which reduces an objective error function (E) as explained below.

Minimize

$$E = \frac{1}{N}\sum_{p=1}^{N}\left[\frac{1}{2}(|C_p| - |C_p^e|)^2\right] \tag{3.14}$$

Here, E is the assumed value of the squared errors for the magnitude of zeolite yield, whereas N stands for the total number of experimental observations. Further, the output from the fuzzy model is indicated by C_p while C_p^e is the zeolite yield from p^{th} experiments for the

same set of inputs. The stated zero order TS fuzzy model has five inputs and each of these is defined using two AFs (Figure 3.2), meaning that the total number of AFs is 10. Also, each of the Gaussian AF can be defined by two parameters: mean and standard deviation. Thus, there are 20 parameters for the antecedent fuzzy variables that are needed to be tuned.

Applying a gradient descent method, the fuzzy parameters could be updated to reduce the objective error function (3.14). The update rule for various parameters expressed as (3.15).

$$p_{km}(t+1) = p_{km}(t) - \frac{\alpha}{N}\sum_{p=1}^{N}\frac{\partial E^p}{\partial p_{km}} \tag{3.15}$$

Here in equation (3.16), p_{km} is the vector of antecedent fuzzy AF parameters for k^{th} input and m^{th} AF. The number of epochs is given by 't', constant 'α' is used for the learning rate that normally decides the quantum of change in the parameters following every iteration and 'N' denotes the number of observations accessible for tuning. Partial derivatives for the parametric updates shown in (3.15) can be computed applying following series rule.

$$\frac{\partial E_p}{\partial p_{km}} = \sum_{p=1}^{N}\left(\frac{\partial E_p}{\partial C_p}\cdot\frac{\partial C_p}{\partial w_i^p}\cdot\frac{\partial w_i^p}{\partial A_{km}^p}\cdot\frac{\partial A_{km}^p}{\partial p_{km}}\right) \tag{3.16}$$

The partial derivatives in the chain rule can be further calculated as below.

$$\text{Since} \quad E_p = \frac{1}{2}(|C_p| - |C_p^e|)^2; \qquad \frac{\partial E_p}{\partial C_p} = (|C_p| - |C_p^e|) \tag{3.17}$$

$$\text{Further since} \quad C_p = \frac{\sum_{i=1}^{Nr}(w_i.y_i)}{\sum_{i=1}^{Nr} w_i}; \qquad \frac{\partial C_p}{\partial w_i^p} = \frac{(y_i^p - C_p)}{\sum_{i=1}^{Nr} w_i^p} \tag{3.18}$$

$$\text{Using} \quad w_i^p = \prod_{k=1}^{5} P_{ik} A_k^p(I_k^p); \quad \text{for} \quad \frac{\partial w_i^p}{\partial A_{km}^p} = P_{ik}\frac{\partial A_k^p}{\partial A_{km}^p}\prod_{K\neq k} P_{iK} A_K^p(I_K^p) \tag{3.19}$$

Lastly, partial derivative $\frac{\partial A_{km}^p}{\partial p_{km}}$ where $A_{km}^p(I_k^p) = ae^{-\frac{(I_k - \bar{I}_{km})^2}{2\sigma_{km}}}$ could be calculated with regard to a couple of parameters specifically, $\bar{I}_k$ a and σ_k are responsible for the activation values that should constantly be higher than zero. Hence, having received all the partial derivatives, the chain rule mentioned in (3.18) is calculated and applied to the update equation (3.15) to revise the parameters and decrease the error function. The results are presented in Figure 3.3. Consequent variables in fuzzy model (y_i) are not optimized, rather these are determined to apply pseudo-inverse of earlier acquired regressor matrix (3.14).

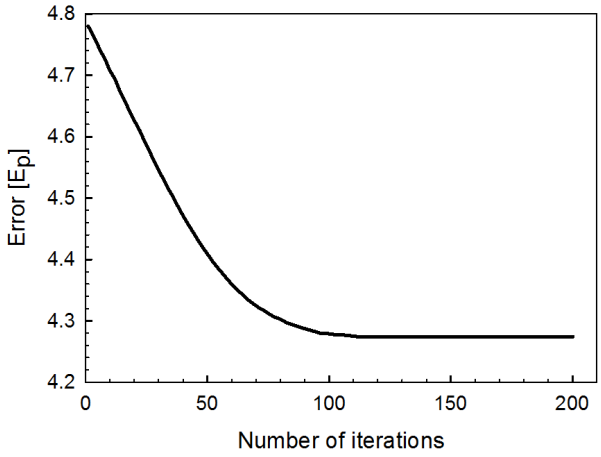

Figure 3.3. Minimization of the expected value of the squared errors

The gradient descent method explained in this work operates iteratively in a couple of stages. Initially, the pseudo-inverse operation is conducted to distinguish the consequent variables for the initially estimated antecedent parameters and later the antecedent parameters are updated using the error signal and the update equation (3.15). The assumed value of the squared errors, E_p, diminishes steadily with the number of iterations, reaching a minimum index of 4.3 within around 100 iterations. Moreover, Table 3.3 gives the values of the vector, y_i after optimization, while the analogous indexes of parameters B, C, and sigma are specified in Table 3.4.

Table 3.3. The vector of optimized consequent parameters (W) used in the fuzzy model for conversion prediction

y_1	y_2	y_3	y_4	y_5	y_6	y_7	y_8
865172.0	-4372720	-117809.0	510856.0	-119494.0	574073.0	15231.11	-64196.02
y_9	y_{10}	y_{11}	y_{12}	y_{13}	y_{14}	y_{15}	y_{16}
64706.02	341811.8	4192.489	-8472.62	-2940.70	43662.40	8661.60	34265.87
y_{17}	y_{18}	y_{19}	y_{20}	y_{21}	y_{22}	y_{23}	y_{24}
-13166.55	-8997.181	489.3450	2049.933	-6313.479	193230.8	3220.417	-22374.79
y_{25}	y_{26}	y_{27}	y_{28}	y_{29}	y_{30}	y_{31}	y_{32}
12235.96	1252.068	1835.888	-9821.161	-30171.53	8724.090	4004.200	-6834.360

Table 3.4. Points of minimum fuzziness (B and C in Figure 3.1), and standard deviation (σ) before and after optimization, for all five variables

Parameter	B		C		SIGMA	
	Initial values	After optimization	Initial values	After optimization	Initial values	After optimization
Concentration	01.71	00.33	03.04	03.74	00.80	00.62
Time	41.00	22.03	65.50	72.03	14.70	21.26
Temperature	103.75	75.01	151.25	159.00	28.50	35.68
L/S	08.96	01.26	16.98	19.97	04.81	07.99
Si/Al	01.85	01.33	02.74	02.79	00.53	00.82

3.4. Synthesis of composites with silver nanoparticles

On the basis of full characterization of all ZFAs synthesized under optimum parameters and preliminary adsorption results, it was decided to work with K-ZFA and M-ZFA for impregnation of Ag NPs to yield nanocomposites. The doping of Ag NPs into the microstructure of synthetic zeolite is carried out in two key steps. The Ag^+ ions were exchanged by sodium cations and followed by reduction (Figure 3.4).

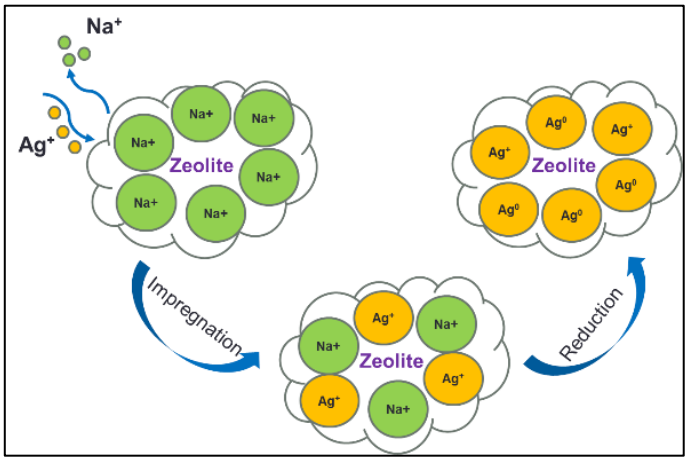

Figure 3.4. Schematic diagram of nanocomposite production from synthetic zeolite

First, zeolite samples were fully dried at 300ºC for 3 hours to evaporate any residual water or entrapped matter in the microstructure of the material. Then, a dilute solution of $AgNO_3$ (1 equivalent, 10 mmol/L) was added, where the volume of solution was varied depending on the loading of Ag NPs (1-10 mL per 1 g of zeolite) and left to soak for 12 hours. The

containers were covered with a double layer of aluminum foil to avoid oxidation of Ag^+ ions due to the effect of light. Then, the produced ion-exchanged zeolite slurry was dried at 130ºC for 3 hours, followed by a second soaking step (1-10 mL of 10 mmol/L $AgNO_3$) to obtain fully silver ion-exchanged zeolitic material (Ag^+-K-ZFA or Ag^+-M-ZFA). The obtained silver ion-exchanged zeolites, so-called nanocomposites, were dried at 130ºC for 3 hours, filtered and washed with deionized water until pH reached a neutral value.

Following that, the collected Ag^+-ZFAs were annealed at 500ºC for 3 hours and accompanied by 4 hours of reduction of Ag^+ ions into Ag NPs applying reducing agent $NaBH_4$ (5 equivalents) to obtain nanocomposites with different amount of Ag NPs (Xwt.%-Y-ZFA). The same circle of experiments was done without adding $AgNO_3$ solution to consider the impact of reduction on zeolite microstructure and adsorption performance. The materials collected after this synthesis are labeled as K-R-ZFA and M-R-ZFA, correspondingly. All produced nanocomposited and reduced zeolites were collected in tightly closed containers for farther characterizations and adsorption analyses.

3.5. Characterization and analysis methods

All raw CFAs, ZFAs and their respective nanocomposites and reduced materials were subjected to several physical and chemical characterization methods and analysis before (pre-) and after (post-) adsorption experiments.

3.5.1. Mineralogical characterization

X-Ray Diffraction (XRD)

XRD was used to acquire data on mineralogical phases that present in raw CFAs, synthesized ZFAs and Ag-ZFAs. The CFA and produced ZFA and Ag-ZFA samples were examined as received with no preceding purification and separation, while the synthetic zeolite and nanocomposite after adsorption of Hg^{2+} and I^- were thoroughly washed with deionized water and fully dried at 40ºC overnight before characterization. The XRD pattern was recorded by Bruker D8-Focus (Germany) on a diffractometer with Ni-filtered CuKα radiation (k = 1.5406 A°) at 40 kV and 40 mA with a diffraction angle of 2θ and a scanning range of 5 to 70° (Figure 3.5). The solid materials after adsorption of Hg^{2+} and I^- were subjected to XRD analysis to confirm the formation of an amalgam and precipitate.

Figure 3.5. Sample analysis on XRD

X-Ray Fluorescence (XRF)

XRF instrument Axios Max (PANalytical, Netherlands) was applied to obtain the chemical composition of all produced and raw materials. The pristine CFA sample was studied as received with no prior purification, while all derived materials were thoroughly washed with deionized water and dried before characterization. The sample to binder proportion was fixed at 10 g to 3 g, correspondingly (total mass of 13 g) with a diameter of a tablet of 5 cm and a thickness of 0.5 cm. XRF pattern was recorded at 20 kV and 10 mA The quantitative analyses were conducted in a nitrogen atmosphere with duplication. Typical sample preparation steps are shown in Figure 3.6.

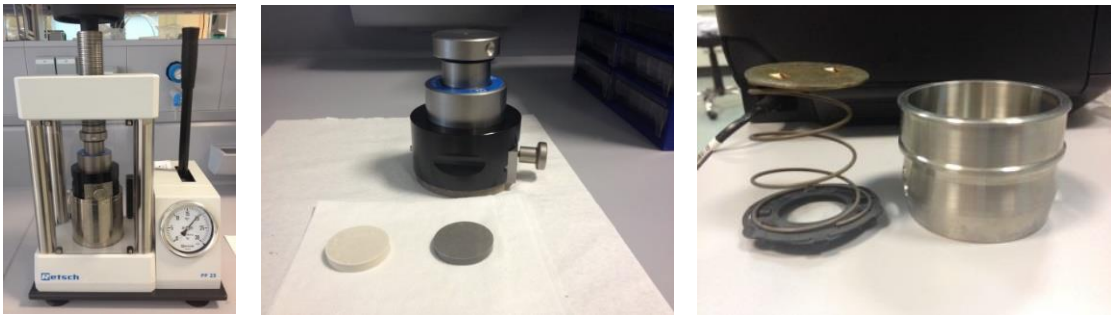

Figure 3.6. Sample preparation for XRF analysis

3.5.2. Microstructural characterization

Particle size analyzer (PSA)

PSA was used to acquire data on volume percent of the size of particle and distribution of size between the range of 0.01 μm to 10 mm (Figure 3.7). Deionized water was chosen as a

dispersant for all sample measurements in Mastersizer 3000 (Malvern Instruments, UK) on Hydro-MV mode, which is in-consistency with adsorption experiments. The obscuration level was set between 10 to 15% to ensure homogeneous distribution of samples. The PSA readings were conducted three times and mean values with standard deviations are presented.

Figure 3.7. Sample analysis on Mastersizer 3000

Nitrogen Porosimeter (PN)

PN Autosorb IQ (Quantochrome, USA) was used to get information on the specific surface area (SSA), total specific volume and average pore size of materials. The BET method of calculation was primarily applied for analysis of results (unless otherwise stated). The sample preparation step for BET measurements includes a 3-hour degassing of the sample prior to analysis at a step by step heating starting from 50°C to 200°C. The maximum degassing temperature was set at 110°C for samples after adsorption experiments of Hg^{2+} and I^-. For all BET analysis, the 9 mm borosilicate sample holder without rod was used. Typical sample analysis experiment is shown in Figure 3.8.

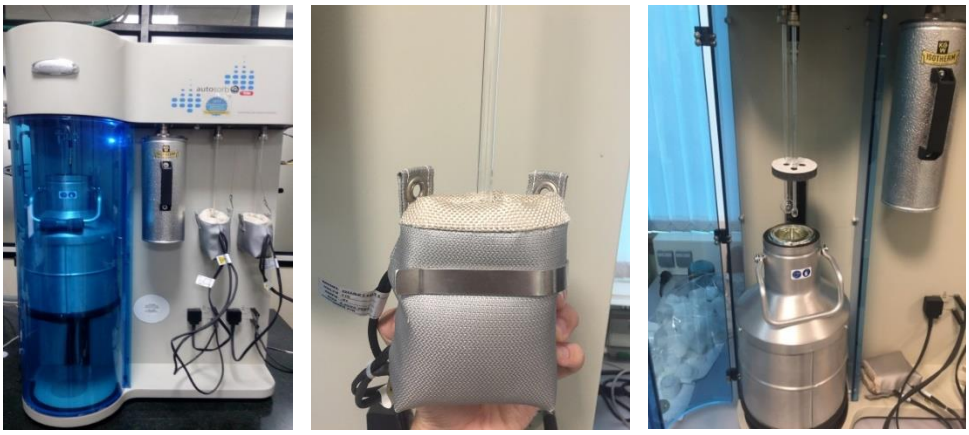

Figure 3.8. Sample analysis on Autosorb IQ

3.5.3. Microscopic analysis

Scanning Electron Microscopy (SEM)

The morphology of samples (~0.1 g) was studied using a 6380LV SEM (JEOL, Japan) operating in LV mode, at 20 kV, fitted with a backscattered electron detector. The spot and area analyses were conducted using a Si (Li) Energy-Dispersive X-ray spectrometer (INCA X-sight, Oxford Instruments) that has a connection with SEM.

High-Resolution Transmission Electron Microscope (HRTEM)

The nanoscale examination was achieved with a high-resolution JEM-2100 LaB6 HRTEM (JEOL, Japan) operating at 200 kV. The samples (~0.2 g) were suspended in a solution of alcohol and treated with ultra-sonication to de-agglomerate the fused particles. A drop from the suspension was then placed on a 300-mesh carbon coated copper grid to dry the sample overnight. The grain microstructure was similarly examined using a bright field detector in scanning (STEM) mode. The analysis of elements was conducted employing the Oxford X-Max 100 Silicon Drift Energy Dispersive X-ray spectrometer that has a connection with TEM. The probe size ranging from 2 nm to 5 nm was used in STEM mode.

3.5.4. Thermal properties

Thermogravimetry and differential scanning calorimetry analyzer (TG-DSC)

In order to evaluate the thermal properties of solids and correlation of weight loss due to entrapped water and Hg evaporation from produced materials thermal analyzer STA 6000 (Perkin Elmer, USA) with a simultaneous TG and DSC units was used (Figure 3.9). The range of temperature used was started from 50°C to 950°C with a heating rate of 10°C/min under nitrogen atmosphere and static conditions. The isothermal heating of the sample was set at 50°C for 1 minute to and a minimum of 10 mg of sample was used for all analysis.

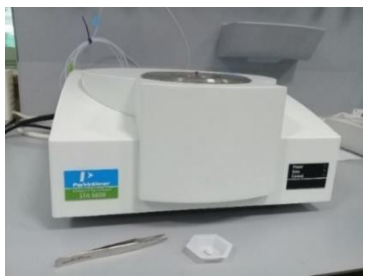

Figure 3.9. Sample analysis on STA 6000

3.5.5. Chemical and zeta potential analysis

Zeta Potential (ZP)

In order to study the surface chemistry of pristine and synthesized materials, the zeta-potential (ZP) at different pH values were determined on Zetasizer Nano ZS (Malvern Instruments, UK). The ZP was recorded at pH 2.0; 4.0; 6.0; 8.0; 10.0 and 12.0 that covers all three major phases: acidic, neutral and basic. The ZP was measured using 0.5 g of the sample that was dispersed in pH-adjusted water solutions with a dispersant refraction index of 1.330, the viscosity of 0.08872 cP and dielectric constant of 78.5. The experiments were conducted at room temperature and all analyses were carried out in triplication and the average results are presented (Figure 3.10).

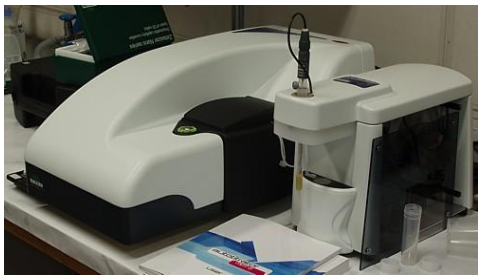

Figure 3.10. Sample analysis on Nano ZS

Total carbon (TC)

TC analysis of CFA samples was conducted by applying Multi-analyzer N/C 3100 (Analytik Jena, Germany) designed for solid and liquid samples (Figure 3.11). A sample mass of 100 mg was used for measurements with a step-wise heating up to 950°C under a pure oxygen atmosphere. The experiments conducted in triplication and the average results are presented.

Figure 3.11. Sample analysis on Multi-analyzer N/C 3100

Microwave-assisted reaction system (MARS)

In order to have data on metal content all CFA samples were digested on MARS (Multiwave Pro, Anton Paar, Austria) and further studied on Atomic absorption spectroscopy (AAS) for metal amount quantification using metal-specific columns. The digestion experimental conditions and amount of samples that were used for each analysis are presented in Figure 3.12 and Table 3.5.

Figure 3.12. Microwave digestion of samples on Multiwave Pro

Table 3.5. Microwave digestion of CFAs under different conditions

Microwave digestion method	Run-1 (Temperature-controlled)	Run-2 (Temperature-controlled)	Run-3 (Power-controlled)	Run-4 (Power-controlled)
Weight of sample (g)	0.3	0.3	0.15	0.15
Volume of HCl (ml)	1	1	2	2
Volume of HF (ml)	2	2	2	2
Volume of HNO_3 (ml)	5	5	6	6
Volume of H_2O (ml)	-	-	10	10
Temperature (°C)	-	-	200	210
Power (W)	1200	1000	-	-
Digestion time (min)	10 ramp/ 60 hold	10 ramp/ 50 hold	10 ramp/ 40 hold	10 ramp/ 50 hold

3.5.6. Spectroscopic analysis

Mercury Analyzer (MA)

MA RA-915M (Lumex, Russia) is a portable multifunctional atomic absorption spectrometer at 254 nm with Zeeman background correction (Figure 3.13). It was applied to calculate the amount of adsorbed Hg^{2+} in samples before and after adsorption experiments. After a set period of time, depending on initial concentration a volume of 0.05 to 0.3 mL of aliquots were taken from adsorption containers and transferred to a sample holder with loaded activated carbon (0.5-1 g per sample) to burn and analyze the samples in pyrolysis attachment of the instrument. The Hg^{2+} detection limit is 0.5 ng/L (0.5 ppt) in the water phase. All adsorption experiments were duplicated and the average results are presented.

Figure 3.13. Sample analysis on RA-915M

The equilibrium, kinetics of adsorption and removal efficiency of Hg^{2+} from aqueous solutions were calculated using the following equations:

$$q_e = \frac{(C_0 - C_e) \times V}{m} \tag{3.20}$$

$$q_t = \frac{(C_0 - C_t) \times V}{m} \tag{3.21}$$

$$\%, Removal = \frac{(C_0 - C_e)}{C_0} \times 100 \tag{3.22}$$

where, q_e is the equilibrium adsorption capacity in [mg/g]; q_t is the adsorption capacity at time t in [mg/g]; C_0 is the initial concentration of solution in [mg/L]; C_e is the equilibrium

concentration of solution in [mg/L]; C_t is the concentration of solution at time *t* in [mg/L]; V is the volume of the aqueous solution used for adsorption experiment in [L]; m is the weight of the adsorbent used for adsorption experiment in [g].

Ultraviolet-visible (UV-Vis) spectrometer

UV-Vis (PhotoLab 6600, Germany) spectrometer as shown in Figure 3.14 was applied to quantify the initial and residual amount of I^- after adsorption. A 1 cm wide quartz cuvettes with a volume of 3 mL were used for analysis. The sample volume was varied between 100 µL to 300 µL and diluted up to 3 mL (by a factor of max. 60) using ultra-pure water. The calibration curve that was used for UV-Vis measurements is shown in Figure 3.15.

Figure 3.14. Sample analysis on photoLab 6600

The adsorption equilibrium, kinetics of adsorption and removal of I^- from water solutions were calculated using the equations 3.20, 3.21 and 3.22, respectively.

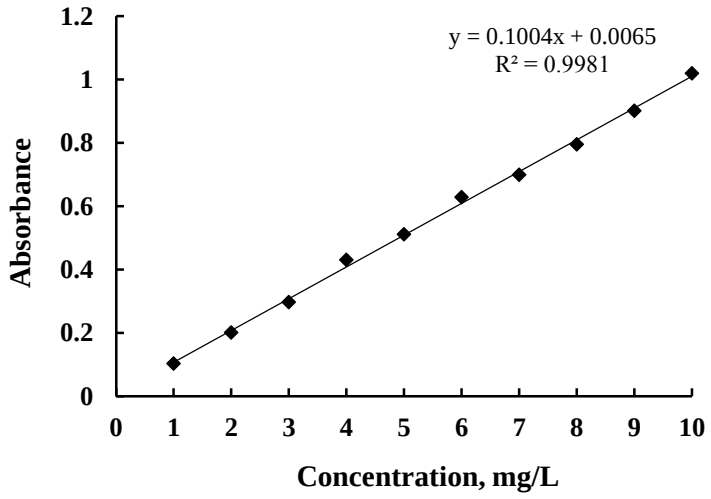

Figure 3.15. The calibration curve used for I^- quantification on UV-Vis

Fourier Transform Infrared (FTIR) spectrometer

The samples were examined on FTIR Nicolet iS5 (Thermo Fisher Scientific, USA) with attenuated total reflection (ATR) unit to find and relate the functional groups present on the surface of solid samples (Figure 3.16). The sample mass of 0.1 g was used for each analysis at room temperature with duplication of measurements.

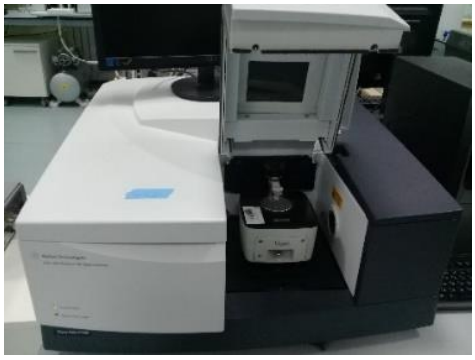

Figure 3.16. Sample analysis on FTIR

Atomic absorption spectroscopy (AAS)

The amount of metal was quantified using AAS (AAnalyst 400 AA, Perkin Elmer, USA) performed with acetylene/oxidant gas mixtures (7.5 mL/min and 6.0 mL/min) by utilising fitting lamps for a specific metal set as displayed in Figure 3.17. All solid matters were first digested and then filtrated by 0.45 μm hydrophilic filters, wherein the solutions are instantly infiltrated and employed for examination. The calibration curve was built for each metal, where the least value of concentration should not be less than 1 mg/L. A dilute solution of 1-2% HNO_3 was employed for washing and keeping the instrument under idle mode. The estimated volume of supernatant per study varies from 5 to 10 mL.

Figure 3.17. A typical set up of AAnalyst 400 AA with metal-specific lamps

3.6. Adsorption studies of mercury and iodide from water

3.6.1. Adsorption kinetics and equilibrium isotherms of Hg^{2+}

The water solution of $HgCl_2$ with a concentration of 100 ppm was applied during the investigation except contrarily stated. All adsorption kinetics tests were replicated at static conditions and room temperature. The starting quantity of $HgCl_2$ was set at 40 mL with pH 2.0 strong acidic phase and adsorbent dosage of 0.2 g. The aliquots were tested from each bottle after a set duration of time (0.08h, 0.15h, 0.5h, 1h, 2h, 4h, 6h, 8h, 24h, 48h and 72h) and determined on MA (RA-915M) for remaining Hg^{2+} ions. A control solution with equal starting concentration without sample and sample in a reference ultra-pure water with the same pH were studied to perform a correlation and eliminate divergence.

Adsorption equilibrium isotherms were performed in 40 mL solution of $HgCl_2$ and KI with starting concentrations of 100, 200, 300, 400, 500 mg/L under the dosage of 0.2 g adsorbent. The experiments were carried out at room temperature and static conditions. The aliquots volume of 50-100 μL were taken from adsorption containers to measure the residual concentrations on MA or UV-Vis till equilibrium attained. The experiments were conducted in duplication and the average values are presented.

3.6.2. Adsorption kinetics and equilibrium isotherms of I^-

The adsorption kinetics and equilibrium were carried out using 0.2 g sample of the nanocomposite placed into a container with I^- solutions of 40 mL and initial concentrations of 75 ppm to 450 ppm with initial adjustment of pH at 2.5. Aliquots of 50-100 μL diluted up to 3 mL were sampled after a set period of time to measure the residual I^- concentration on UV-Vis spectrophotometer (PhotoLab 6600) at a wavelength of 227 nm. All adsorption experiments were conducted at ambient temperature and static conditions in duplicate. Kinetic experiments were continued until no concentration changes were observed, i.e. until equilibrium was attained. In order to control the adsorption experiments, two types of references were used in all adsorption experiments. The first reference contained the same solution of I^- used in adsorption experiment (40 mL with pH 2.5) to evaluate the effect of the adsorption on container walls and change of the concentration due to evaporation, while the second reference contained the nanocomposite with ultra-pure water (0.2 g and 40 mL with pH 2.5). The latter was used to quantify any leached Ag^+ ions from the nanocomposites into acidified water. The analysis of leached Ag^+ ions was made on AAS (AAnalyst 400, Perkin

Elmer). The average removal in reference containers was below 1.5%. The iodide-loaded materials were labeled as 2wt.%-Ag-K-ZFA-*I-C* and 2wt.%-Ag-M-ZFA-*I-C*, where the I is the iodide and C is the initial concentration of I^-.

In order to exclude the effect of I^- peak masking on UV-Vis during pH change over adsorption experiment chloride and nitrate anions were first studied. The initial I^- concentration and volume of investigated solutions were set at 5 ppm and 40 mL, respectively. The pH values of these solutions were adjusted to acidic phase either with c. HCl or HNO_3, while the concentrated solution of NaOH was used to adjust to basic phase. The wavelength range of 190-500 nm were applied for all measurements with duplication at room temperature. It was observed that the masking of I^- peak occurred when c. HNO_3 is used, whereas c. HCl did not affect the intensity neither mask it. The strong basic phases of pH <10 mask the I^- peak, therefore the adsorption experiments were started from acidic phase to avoid the masking and possible misinterpretation of experimental data. The experiment on identification of lowest detectable I^- concentration using 0.1 ppm, 0.25 ppm, 0.5 ppm, 1 ppm, 5 ppm and 10 ppm displayed that the UV-Vis is able to firmly measure 0.25 ppm I^- with distinct peak, which entails that the aliquots should be diluted to concentrations not lower than this value.

3.6.3. Model equations and background theory of adsorption kinetics of I^-

The models used for the uptake of a solute on a solid phase may commonly be categorized as the reaction kinetics and diffusion-based models. In the classic diffusion-based models adsorption of species from a fluid phase into a porous solid comprises three steps: (1) mass transfer by diffusion from the bulk fluid phase through the boundary fluid film to the external surface of the solid (film diffusion); (2) mass transfer by diffusion into the solid phase (intra-particle diffusion) by in sequence or in parallel pore diffusion and surface diffusion; (3) adsorption (physical or chemical) on the surface of solid. In solids with bi-dispersed pore structures, for example, activated carbons and zeolites, macropores act as a pathway for the adsorbate to enter the interior of the particle and mass transfer is influenced by pore diffusion. In micropores, the adsorbent migrates on the surface of the adsorbent and the diffusion is named a surface diffusion [187]. The models that are based on diffusion basically vary in the combinations of the mass transfer resistances, i.e., fluid film, pore fluid (macropore) and surface (micropore) diffusion steps. There are many analytical and

comparative solutions to the models based on diffusion, and empirical equations are widely applied in the literature [188]. Nevertheless, on numerous instants, those uncomplicated models are employed without recognizing the assumptions behind the solutions, viz. the mechanism of diffusion, boundary conditions and equilibrium relationships.

On the other hand, the majority of the models based on reaction kinetics analyze the adsorption or chemical reaction kinetics on the surface of the solid phase considering that mass transfer is sufficiently fast to be omitted. Rigorously conversing, those models are appropriate in chemisorption on solids that are either non-porous or porous presenting high diffusion coefficients. These models are usually experimental and many of them neglect the mass transfer mechanisms that exist in all heterogeneous systems, particularly when porous materials are concerned. The primary obstacle of those models, principally when implemented on physisorption and ion exchange, is the lack of any physical importance and the insufficient value of the experimental kinetic parameters determined by their utilization on empirical data. Presumably, the common models of this type are the pseudo-first-order (PFO) and the pseudo-second-order (PSO) rate equations [189,190]. Limiting the discussion on the removal of I^- by use of solid adsorbents, reaction-kinetics models are common and problematic, as explained above. For instance, PFO has been applied on Ag-doped carbon aerogels [191], PSO on Ag_2O-Ag/TiO_2 composites and Ag@Cu_2O nanoparticles [119,137] and both on hierarchically porous bismuth oxide/layered double hydroxide composites, metal-incorporated porous metal-organic framework (MIL), Cu_2O/Cu modified activated carbon, magnetite nanoparticles-doped organically modified montmorillonite and Ag-Ag_2O modified carbon spheres [117,133,192–195].

Diffusion-based models assume the non-existence of chemical reactions. If a chemical reaction happens, then the models based on reaction-diffusion, namely the shrinking core model, are compatible with the physical reality and could be studied [183]. However, if the reaction is fast and mass transfer is the controlling mechanism diffusion-based models in combination to irreversible equilibrium can be used. Moreover, is well known that adsorption on zeolites and similar materials is controlled by the diffusion in the solid phase. Based on these theoretical observations and taking into account the experimental conditions Boyd's equation can be used, which is based on the homogeneous solid diffusion model (HSDM). The equation can be used if the surface diffusion control either under the infinite

solution volume condition or in the finite solution volume, $\Lambda \leq 1$ and rectangular isotherm [187,188]:

$$\overline{X}(T) = 1 - \Lambda \cdot U(T) \tag{3.23}$$

where $\overline{X} = \overline{C_t} / \overline{C_o}$ is the dimensionless averaged fluid and solid concentrations and where $\overline{C_t}$ and $\overline{C_o}$ is the average fluid phase concentrations at time (t) and the initial, respectively and (Λ) is the partition ratio:

$$\Lambda = \frac{M \cdot \overline{q_o}}{V_L \cdot \overline{C_o}} \tag{3.24}$$

where M is the solid mass, V_L is the fluid volume and $\overline{q_o}$ is the average fluid phase concentration at equilibrium with $\overline{C_o}$, i.e. the maximum solid phase loading for the specific kinetics. The *U(T)* is the fractional attainment of equilibrium as given by Boyd's equation, but for simplicity Vermeulen's approximation can be used [196]:

$$U(T) = [1 - \exp(-\pi^2 \cdot T)]^{0.5} \tag{3.25}$$

Vermeulen's and Boyd's equation give practically the same results the whole range of U(T) [188]. The dimensionless time (T) is defined as follows:

$$T = \frac{D_s \cdot t}{r_p^2} \tag{3.26}$$

where r_p is the particle radius and D_s is the constant surface diffusion coefficient.

3.6.4. Speciation studies of Hg^{2+} and I^-

The solutions of Hg^{2+} and I^- with diverse complex forming anions, namely Cl^- and NO_3^-, the solution concentrations and pH were examined employing Medusa speciation software. The speciation analysis enables to predict the nature of species that might co-exist at circumstantial laboratory conditions, predominantly under particular pH and concentration of initial solutions. All adsorption tests were first examined on this software to determine the co-existing species and to choose the optimum experimental conditions to by-pass any possible precipitation and masking due to the accumulation of insoluble compounds or co-existing species of Hg^{2+} and I^-.

3.6.5. Effect of the anions on Hg^{2+} and I^- adsorption

In order to study how anions affect the removal of Hg^{2+}, different mercury salts were used. Four types of water-soluble mercury salts were selected, namely $HgCl_2$, $Hg(NO_3)_2$, $HgSO_4$ and $HgAc_2$. All four mercury salts were analyzed under the same conditions: 0.2 g of 2wt.%-Ag-SOD was put in a container with 40 mL mercury (II) salts of 100 ppm concentration and pH value corrected to 2 using concentrated HCl. Then, 0.05 mL aliquots from each container were tested after a set interval of time and measured on Mercury analyzer for residual Hg^{2+} ions. All the tests for each type of mercury (II) salt were replicated and the average result is displayed in this work.

To examine the effect of competing and co-existing anions on adsorption behavior, the I^- solution with an initial concentration of 300 ppm and an excess chloride solution with an initial concentration of 1000 ppm were selected. The mass of the nanocomposite 2wt.%-Ag-K-ZFA was set at 0.2 g in 40 mL solution of I^- with an excess amount of chloride anions with an adjusted pH to 2.5. The effect of the co-existing anions, on the other hand, were studied using Cl^-, Br^-, CrO_4^{2-}, and CO_3^{2-} with the same initial concentrations of 300 ppm. The kinetics of I^- adsorption with competing and co-existing anions were measured after a specified time up to 168h with the aliquot volume of 50-100 µL diluted to 3 mL was used on UV-Vis spectrophotometer at 227 nm wavelength. The experiments were conducted under ambient temperature and static conditions in duplicate.

3.6.6. Leaching studies of Hg^{2+} and I^-

In order to assess and compute the performance of Hg^{2+} ions after adsorption K-samples were tested for potential leaching of Hg^{2+} in acidic (pH 2.0) and neutral phases (pH 7.0). First, 0.75 g of adsorbent was put inside a vessel filled with 50 mL Hg^{2+} solution with an initial concentration of 150 ppm. All sample vessels were sealed and left for 6 days at room temperature under static conditions. After a fixed interval of time, the samples were filtrated, completely rinsed with deionized water to attain a neutral pH and dried in a vacuum oven at 70ºC. Then, the dehydrated samples were evenly divided and allocated inside of 2 bottles to examine any leaching effect: one container with 0.3 g of dried sample filled with 50 mL deionized water with an acidified solution and the other container with the same mass and volume under neutral conditions. The aliquots for investigation were collected after 6 and

12 days from each container and experimented for residual Hg^{2+} ions on MA. All the leaching experiments for each type of adsorbent were duplicated and the average result are presented in this work.

The leaching or desorption of adsorbed I^- was examined using both 2wt.%-Ag-K-ZFA and 2wt.%-Ag-M-ZFA samples. Firstly, 0.4 g of nanocomposites were placed in a container with an initial I^- concentration of 350 ppm and 450 ppm for adsorption. The two samples reached equilibrium after 12 days, after that they were air-dried overnight and stored in a closed container. Secondly, the iodide-containing nanocomposites were separated into two sets with 0.2 g of sample and 40 mL water solution in each container. The water solution of the first batch of the experiment was adjusted to a strong acidic phase by using c. HCl at pH 2.5, while in the second batch the water solution with neutral phase pH 7.0 was used. The aliquots of 3 mL were taken from each container after 4 days, 8 days and 12 days to measure any leached amount of I^- on UV-Vis at 227 nm wavelength and immediately placed back into solution container after measurements. The experiments were conducted under room temperature and static condition with an average value of duplication for each set of experiment.

3.6.7. The maximum adsorption capacity of Hg^{2+}

Samples of K-ZFA and 2wt.%-Ag-K-ZFA were examined by the procedure of renewed batch equilibrations. A known amount of sample (0.25 g) was allocated to a container with documented volume (50 mL) and concentration (10 ppm) of Hg^{2+} solutions at ambient temperature. The initial pH was corrected to 2.0, comparable to adsorption tests and 0.05-0.3 mL of aliquots were collected to measure the remaining Hg^{2+} concentration after every 3 days. Then, the used solution of Hg^{2+} in the container was fully substituted with a fresh solution of Hg^{2+} that has the equal volume, concentration, and pH till there is no further adsorption of samples were detected.

3.6.8. Effect of silver loading in nanocomposite on Hg^{2+} adsorption

With the aim to investigate how the doped or impregnated Ag NPs quantity within the matrix of nanocomposite influence the adsorption profile of Hg^{2+} ions, three distinct Ag-K-ZFAs were applied with Ag NPs quantity at 0.15wt.%, 0.34wt.% and 0.92wt.%. In order to perform this research, the 10 ppm of freshly prepared Hg^{2+} solution was applied with an adjusted pH of 2.0. The starting volume of simulated Hg^{2+} solution was fixed at 40 mL with 0.3 g of adsorbent mass. The aliquots of 0.2 mL were collected for analysis after 48 h (2 days), 216 h (9 days) and 288 h (9 days) to measure the residual concentration in adsorption container. To study the potential effect of containers walls on adsorption the same containers were examined with a control solution that had the same starting concentration in a container without sample and sample in reference deioninzed water solution with the same pH were examined to make a comparison and exclude deviation. The adsorption studies were carried out at room temperature and static conditions and each measurement was duplicated.

CHAPTER 4

SYNTHESIS AND OPTIMIZATION OF ZEOLITE PRODUCTION

4.1. Introduction

Environmental Protection Agency measures an outflow of CFA, a by-product from the combustion of coal in power plants, to as huge as 140 million tons annually [1]. Recognizing the enormous volumes of CFA produced and the evidence that it provokes severe ecological and health difficulties [8,11,197], requires a meticulous research on utilization of CFA. One of the practical steps of turning CFA to a valuable product is generating synthetic zeolites [46,198], which have a broad spectrum of purposes, especially in the area of horticulture, pollution remediation, and catalysis [19]. Synthetic zeolites could be generated employing numerous crude supplies as clay [199] and siliceous minerals [200], wherein CFA is recognized as proper stock material due to its reduced cost, sufficient volume, and the probability to generate various zeolites *via* modification of the parameters of reaction [140].

The elemental composition of zeolite and CFA are comparable; yet, those two diverge in their crystallinity: CFA is largely formed of an amorphous arrangement, whereas zeolite possesses a distinct crystalline structure [15]. Furthermore, zeolites typically have higher cation exchange capacity (CEC), surface area, and also exhibits enhanced thermic resistance [201] than CFA and therefore further improves utilization areas. There are certain parameters that influence the zeolite formation process, viz., alkali concentration, reaction time and temperature, loading ratio (liquid to solid ratio, L/S), and Si/Al ratio in CFA [15,184,201]. Depending on those settings it is probable to produce varying pureness and sort of zeolites, namely zeolite A [198], zeolite Na-P [202], sodalite [46,203], analcime [141], etc.

Optimization of synthetic zeolites generation by utilizing CFA as a crude material is growing of highest interest with its expanding share in commercialization. This, though, demands a precise knowledge of the zeolitization method and relevant reaction mechanisms. The selected practical generation approach for the synthesis of zeolites is the hydrothermal treatment of CFA in a strong alkali solution at high temperatures. The method comprises diverse parameters, including reaction temperature and time, the concentration and quantity of alkali solution, and silica content in CFA that affect in a substantial way to the conversion. Those parameters resemble to have an arbitrary influence on the yield of zeolite.

4.2. Focus of the chapter

Empirically, it is essential to conduct substantial processing to define the optimum parameters of zeolite synthesis from CFA, which is unfavorable in terms of both time and expenditure. Therefore, various optimization procedures as the Taguchi method, artificial neural networks, response surface methodology, fuzzy logic, and a genetic algorithm can be applied to laboratory outcomes so as to attain optimum process parameters. Fuzzy logic is type of heuristic approaches where the usable numerical data is transformed into qualitative data and logical inference is illustrated employing suitably devised rule-base. In the existing study, a fuzzy logic-based system is elaborated to recognize and model the mechanism of zeolite formation process.

The introduced approach will intrinsically support in a reliable perception of zeolitization mechanism and in determining optimum reaction parameters, which correspondingly maintains the demand for this kind of analysis. The chapter focuses on aspects of investigations performed to transform CFA to synthetic zeolites employing factorial analysis, the full characterization of parent and produced materials accompanied by the architecture of the fuzzy system used.

4.3. Coal fly ash and synthetic zeolite characterization

The detailed XRF data on chemical composition of raw CFAs and produced zeolites are presented in Table 4.1. The results reveal that the major fraction of chemical elements containing in parent CFAs are Al, Si, Fe and Ca, as it was estimated. It is evident from the data that the amount of iron is relatively high in E-CFA (27.786%) in comparison with K-CFA (16.076%) and M-CFA (18.138%), and considerably greater than in CFAs from other regions of the world [139,140,143,204], that might bring another advantage in terms of utilization paramagnetic properties. Another noticeable fact in the chemical composition of CFAs is that M-CFA and E-CFA have a comparable amount of CaO (6.775% and 6.077%), which is almost twice much than in K-CFA (2.798%). In general, M-CFA is richer for alkaline metals with the amount being 11.187%, which in turn indicates an inherently basic nature of material.

The high amount of aluminosilicates and iron (II) oxides indicates the bituminous origin of all CFAs. The Si/Al ratio of M-CFA, K-CFA and E-CFA is 1.80, 1.70 and 2.15,

correspondingly. The obtained ratio is analogous with results of literature elsewhere [140,184,205]. The chemical composition of zeolites, on the other hand, has slightly been changed due to alkaline hydrothermal treatment. The amount of Na has substantially been increased to 4.447% and 5.858% for K-ZFA and M-ZFA, respectively.

Table 4.1. The elemental composition of Kazakhstani CFAs (wt.%)

Compounds	E-CFA	K-CFA	K-ZFA	M-ZFA	M-CFA
Na_2O	0.187	0.678	4.447	5.858	0.763
MgO	0.628	0.716	0.708	1.145	1.423
Al_2O_3	18.071	25.761	30.888	24.859	21.750
SiO_2	44.128	49.802	32.488	32.343	44.425
SO_3	0.204	0.237	0.086	0.874	2.248
K_2O	0.514	1.324	0.150	0.260	1.857
CaO	6.077	2.798	2.390	4.696	6.775
TiO_2	1.353	1.636	1.258	0.959	1.169
Cr_2O_3	0.035	0.033	3.104	3.387	0.024
MnO	0.608	0.216	0.411	0.608	0.432
Fe_2O_3	27.786	16.076	23.066	23.578	18.138
CuO	0.032	0.042	0.028	0.034	0.035
ZnO	0.013	0.052	0.040	0.036	0.024
BaO	0.103	0.143	0.119	0.273	0.369

The aluminosilicates has also experienced some changes. In both synthetic zeolites in comparison with parent CFAs the Si/Al ratio has been decreased, which is essentially due to dissolution of aluminosilicates under strong alkaline phase and high temperature treatment. This in turn resulted in formation of crystalline phase ZFAs as opposed to more amorphous phase CFAs. All CFAs and ZFAs retain the negligible amount of trace heavy metals with weights below 1% (Mn, Cu, Zn, Cr).

The metal composition of CFAs was also investigated on AAS after microwave digestion process that involved a dissolution with strong acids. Table 4.2 shows the average results of

metal contents obtained for E-CFA, K-CFA and M-CFA, which additionally confirms the high amount of iron.

Table 4.2. The metal composition of CFAs after microwave digestion (mg/g)

Metals	E-CFA	K-CFA	M-CFA
Na	2.883	2.733	3.508
K	1.373	1.297	1.183
Ca	3.637	1.537	5.455
Mg	0.518	0.086	0.285
Zn	0.058	0.177	0.104
Fe	41.383	29.233	34.833
Cu	0.025	0.104	0.075
Co	0.180	0.072	0.038
Ni	0.030	0.126	0.066
Mn	2.617	0.885	1.092
Pb	0.004	0.021	0.023
Cd	0.001	0.002	0.002

The mineralogical phase content of CFAs were examined on XRD. The major phases that were detected in parent raw CFAs are mullite, quartz, magnetite. The high amount of magnetite (Fe_2O_3) along with the average total content of aluminosilicates (Al_2O_3 and SiO_2) in CFAs, double confirms the bituminous nature of coals that were used for the production of CFAs in power plants. The spectrums of ZFAs formed from parent CFAs demonstrate the development of crystals of the zeolitic phases, such as Analcime and Sodalite as major types. Overall, the content of the zeolitic phase in both produced materials corresponds 51-60%. Figure 4.3 shows the XRD spectrums of K-CFA, K-ZFA, and M-ZFA.

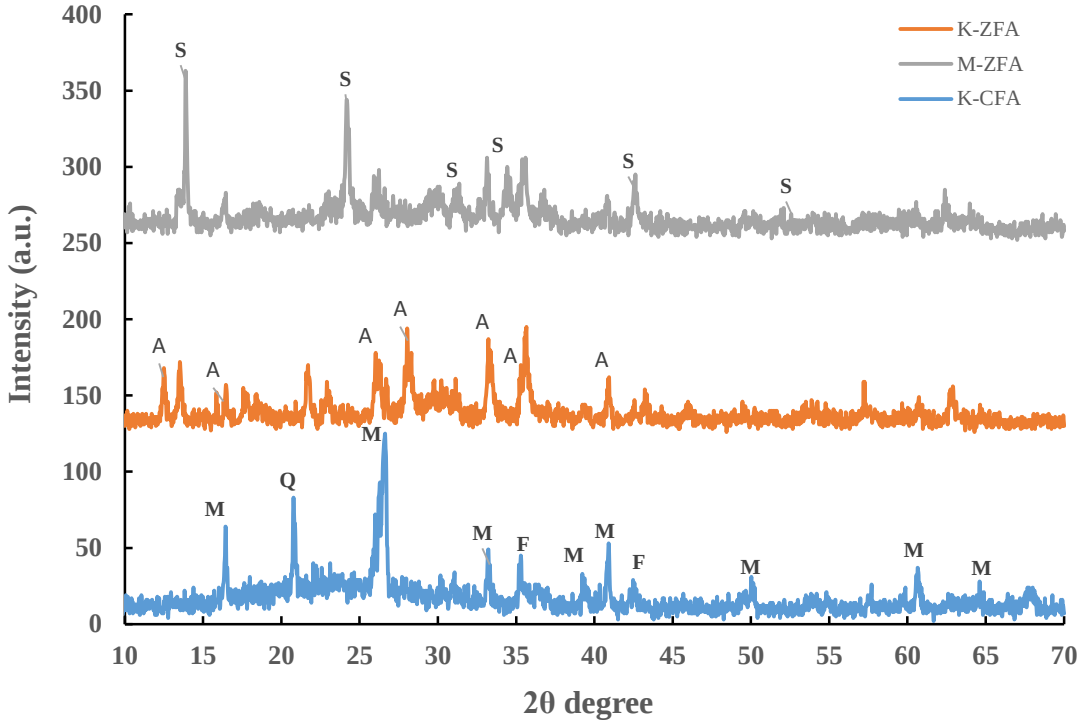

Figure 4.1. A comparative XRD spectrum of K-CFA, K-ZFA and M-ZFA
(S: sodalite; A: analcime; M: mullite; Q: quartz; F: magnetite)

Table 4.3 presents the results of porosimetric analysis of CFAs and zeolites. The results indicate that all CFAs have similar specific surface areas (SSA) calculated by BET method that ranges between 18 to 23 m^2/g, whereas the average pore diameter slightly differs. The smallest pore size was observed for E-CFA (5.5 nm), while the M-CFA showed the relatively wide pores (15 nm) with pore volumes at 0.07 cm^3/g.

The average size of the pores calculated using the BET method according to literature varies between 0.7 nm [198] and spread up to 27 nm [19,45]. The SSA values, on the other hand, might be expanded from 1.1 to 15.6 m^2/g subject to phase content and pore type, whereas the total volume of pores may fluctuate from 0.004 to 0.022 cm^3/g [12,17,18,45]. It should be highlighted that the SSA of ZFAs has considerably improved, from 18 m^2/g to 56 m^2/g for K-ZFA and from 20 m^2/g to 61 m^2/g for M-ZFA. The increase in the SSA has affected the pore volumes that has also expanded for both zeolites. The average pore size has slightly changed for zeolites that might be due to saturation with sodium and variations in coordination of molecules and the elevated reaction temperature that mildly suppressed or widen the pores.

Table 4.3. The porosimetric analysis of CFAs and ZFAs

CFA type	Average pore diameter [nm]	Specific surface rea [m^2/g]	Total pore volume [cm^3/g]
K-CFA	10±2.0	18±15	0.04±0.02
M-CFA	15±4.0	20±7.0	0.07±0.05
E-CFA	5.5±1.4	23±4.8	0.03±0.01
K-ZFA	14 ± 0.2	56 ± 12	0.25 ± 0.01
M-ZFA	17 ± 3.0	61 ± 12	0.26 ± 0.08

The PSD analysis displayed in Table 4.4, indicates that the CFAs have much larger particles in contrast with produced zeolites. For example, the average size of K-CFA is 57 μm, while the corresponding zeolite K-ZFA shows 25 μm. The same tendency could be observed for M-CFA and M-ZFA that demonstrate 67 μm and 28 μm, respectively.

The average particle size of zeolites, on the other hand, varies in a tight range 25-28 μm. The small size of particles could facilitate the kinetics of reaction during adsorption experiments and should be accurately identified in comparative studies.

Table 4.4. The particle size analysis of CFAs and ZFAs

CFA type	Dv(10), μm	Dv(50), μm	Dv(90), μm
E-CFA	15±1.4	109±8.3	260±12
K-CFA	22±2.4	57±0.03	161±5.7
M-CFA	9±2.4	67±0.03	428±5.7
K-ZFA	6 ± 0.3	25 ±0.8	66 ±0.8
M-ZFA	8 ± 0.3	28 ±0.8	157 ±0.8

Another important property of solid materials is their surface charge under various conditions. Figure 4.2 shows how the zeta potential of parent CFAs and derived zeolites has changed over pH increase from acidic to basic phases. The results reveal that the zeta potential steadily decreases with some minor fluctuations from pH 2-4 up to pH 8-10, after that it slightly goes upward towards reaching strong basic conditions. CFAs have slightly

less positive charge (3.51-7.82 mV) under acidic conditions in comparison with ZFAs, which is explained by the saturation of sodium in zeolites. The overall trend is alike in materials, where the point of zero charge (pH_{ZPC}) is reached in acidic phase 3.5-5.0.

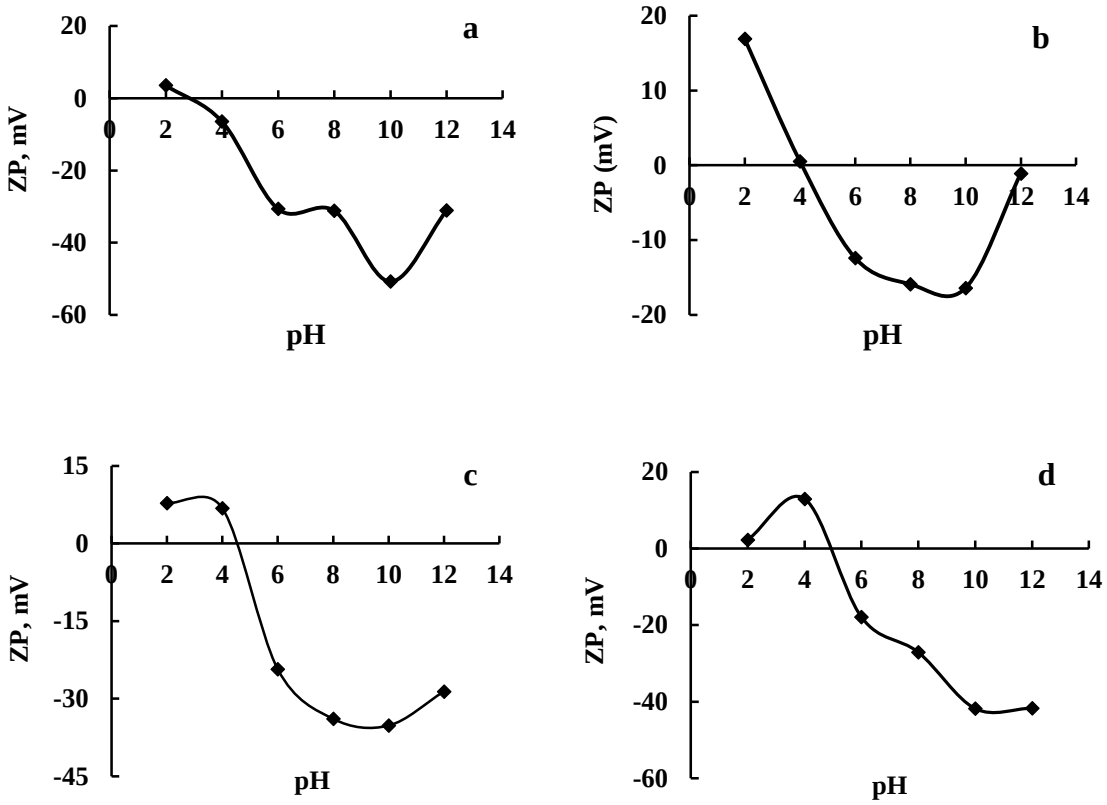

Figure 4.2. Zeta potential values of CFAs and ZFAs at various pH:
K-CFA (a); K-ZFA (c); M-CFA (b); M-ZFA (d)

The surface morphology and composition of initial CFAs and zeolitic phase growth on the surface of CFAs was examined on SEM as shown in Figure 4.3. In general, the shape of CFAs could be considered as spherical with some irregularities. The Figure 4.3c shows the growth of crystalline zeolite phase of K-ZFA, while Figure 4.3d displays the cross-section of M-ZFA particle with a sponge-like structure that has irregular voids of different sizes, which create the active sites for potential molecules and adsorbates. Additional SEM micrographs of CFAs and ZFAs could be found in Figures B1-B2. The FTIR characterization of K-CFA and M-CFA along with respective synthetic zeolites could are presented in Figures B3-B4.

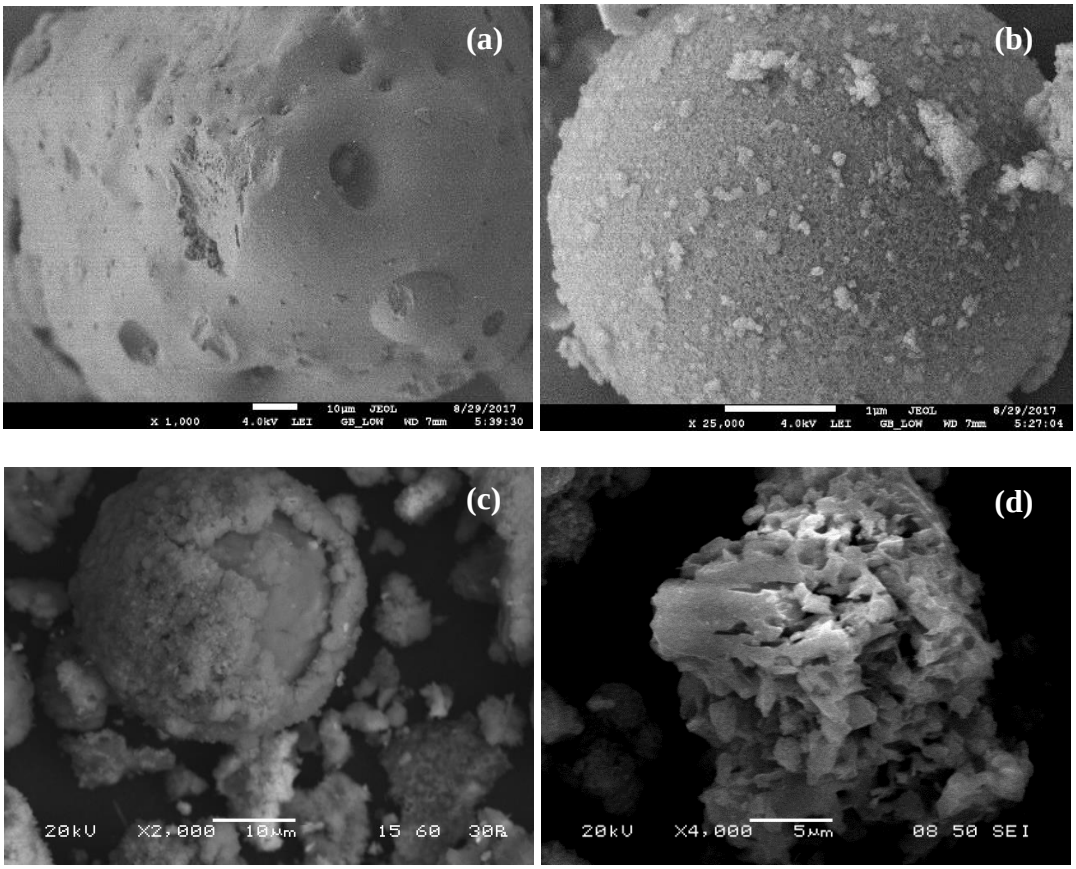

Figure 4.3. SEM images of CFAs: K-CFA (a), M-CFA (b) and K-ZFA (c), M-ZFA (d)

According to thermographs of CFAs, E-CFA has lost nearly 4.6% of initial mass while heating up to 950°C. The most noticeable peak of loss was observed at 641.67°C (-0.012 mg) with more visible weight loss peaks at 73.51°C (-0.006 mg) and 337.96°C (-0.003 mg). In general, the thermographs of E-CFA demonstrated a steady loss through the set range of temperature. The thermographs of M-CFA shown in Figure 4.4, revealed a distinctive double step weight loss over temperature under examination.

According to obtained results, the initial set of loss was observed at 123.1°C (-0.199 mg), which was followed by a smooth weight loss until it raised to the temperature range between 565.8-667.25°C (-0.071 mg). The results indicate that the M-CFA sample lost 0.85 mg or 2.4wt.% in total, which is nearly twice as less as in E-CFA. The comparable findings show that M-CFA sample has less of original coal that was used for M-CFA production, less amount of entrapped water and other species within moieties. The least amount of loss was observed for K-CFA that indicated a total mass loss index at around 0.28 mg or 0.57wt.% with a stable decline over temperature.

The results obtained on Multianalyzer, the total carbon amount in E-CFA, K-CFA and M-CFA showed 2.15wt.%, 0.58wt.% and 0.82wt.%, respectively. These values are corroborated with the weight loss indexes demonstrated on thermal analysis, where the E-CFA showed the maximum mass loss, whereas the K-CFA sample indicated a minimum amount of mass loss.

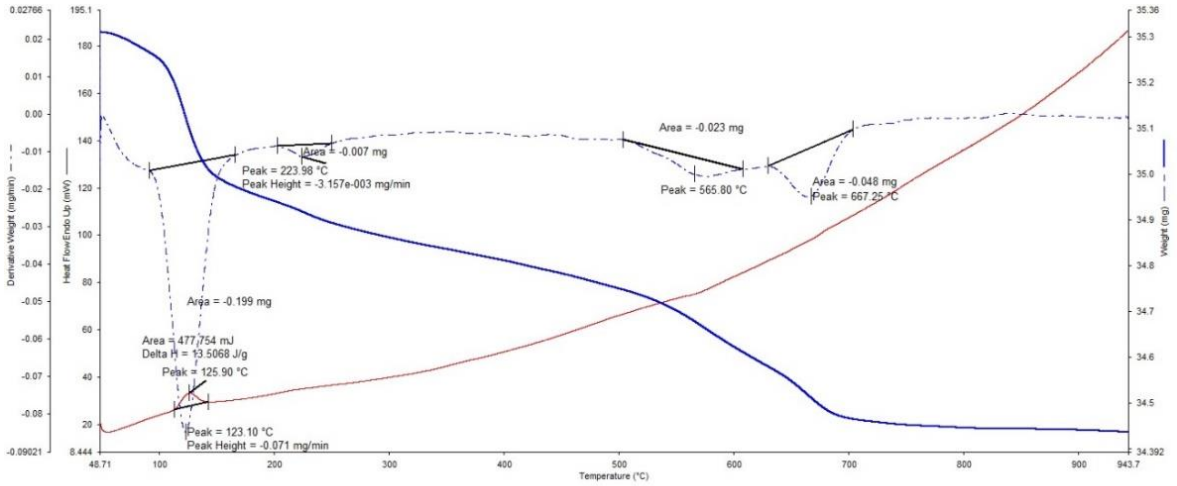

Figure 4.4. A typical TGA/DSC thermograph of M-CFA

4.4. Factorial analysis of zeolite synthesis from coal fly ash

The factorial analyses of zeolite production from CFA was conducted using the E-CFA. The key parameters of the zeolite synthesis reaction, such as a concentration of the initial alkaline solution, a reaction time and temperature were changed in order to evaluate the effect of each and group of parameters. The L/S ratio remained constant at 20 mL/g, while the Si/Al ratio fixed at 1.44. Each set of experiment were duplicated and the reported conversion index has a standard deviation of less than 5% for all synthesis.

The factorial analysis results as presented in Table 4.5 revealed that if the influence of one investigational parameter is considered, whereas the other parameters were kept constant, it could clearly be observed that the effect of synthesis reaction temperature and time is significant. Furthermore, it indicates that the effect of alkali concentration on conversion of CFA into zeolite is minor in comparison with other parameters, whereas the synergetic behavior of two synthesis parameters, namely the reaction temperature in correlation with synthesis time and initial alkali concentration could significantly increase the conversion

index into synthetic zeolite. It should be noted that within the experimental range set for these synthesis reactions the maximum progressive impact in relation to conversion index was obtained when all investigational parameters were set to maximum values.

Table 4.5. CFA derived ZFA production based on factorial analysis

No.	No. as in Table 3.1	Concentration (M)	Time (h)	Temperature (°C)	Conversion (%)	Factor(s) effect (%)
1	15	1	24	90	19.8	0
2	16	1	24	110	45.3	25.5
3	17	1	48	90	48.2	28.4
4	18	3	24	90	39.6	19.8
5	19	1	48	110	47.0	27.2
6	20	3	24	110	55.9	36.1
7	21	3	48	90	35.5	15.7
8	22	3	48	110	78.0	58.2

4.5. Optimization results using the fuzzy model

The results for the fuzzy model and its optimization were mentioned in the previous sections along with the model. In this section, comparative data points of the fuzzy model output with the experimental indexes are presented, which is followed by the effect of parameter discussion on zeolitic phase development. Figure 4.5 displays the percentage conversion of CFA into ZFAs, for all 31 points as computed from the model, in comparison with the experimental values as noted in Table 3.1. The experiments carried out under this research is presented by points 15-22 with the standard deviation of < 5%. The percentage error of the fuzzy model in a predicted conversion index is shown in Figure 4.5.

The results revealed that the output of the optimized fuzzy model is in close correlation with the experimental values. As mentioned previously, points 15 to 22 are based on experiments conducted in this research, while other conversion indexes are extracted from the literature. Furthermore, Figure 4.5 shows the percentage error between the outputs of the experimental work and the fuzzy model, where the average error is found to be 4.7 % and the maximum error is 18.6 % for point №30.

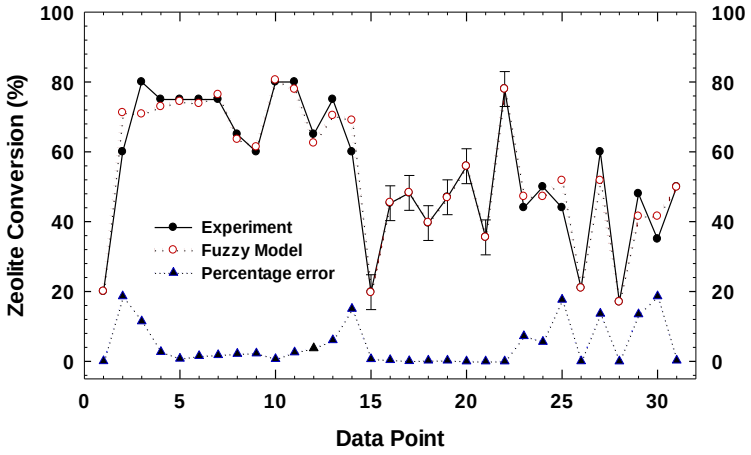

Figure 4.5. CFA to zeolite conversion: fuzzy model vs. experiments

Following this, the effects of single parameters, namely an initial alkali concentration, reaction time, reaction temperature, L/S and Si/Al ratio on conversion of CFA into ZFA is considered. The experimental results along with the statistical data from other related research from the literature on the influence of reaction parameters on yield are deliberated, where the fuzzy model was applied to examine and consider the influence of specific parameters on yield. In order to systematically construct the dependence graphs based on the fuzzy model the lowest, average and highest values of parameters were applied, whereas the remaining parameters set at their average values. For instance, to estimate the effect of the reaction time on conversion into zeolite the reaction temperature, initial concentration of alkali solution, and L/S ratio were set constant at their average indexes.

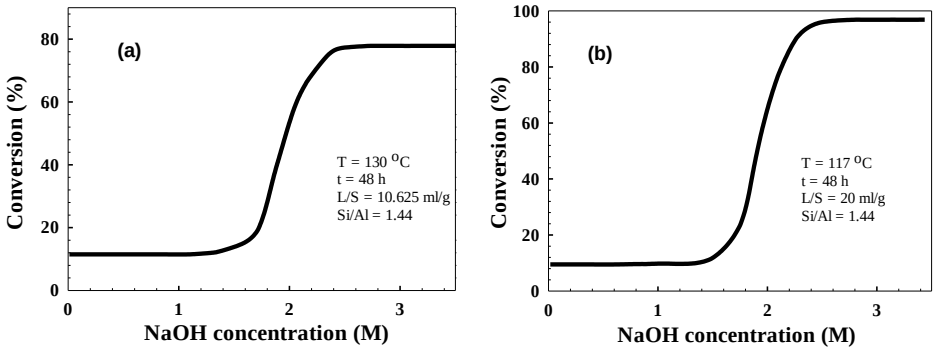

Figure 4.6. The dependence of CFA conversion into zeolite on concentration of NaOH

Figure 4.6 shows the correlation of CFA conversion into ZFA on initial alkali concentration used for the synthesis. In Figure 4.6a the reaction temperature was kept at 130°C, time at

48 h, and L/S ratio at 10.625 ml/g, whereas in Figure 4.6b, the values were 117^{o}C, 48 h, and 20 ml/g, respectively. It should be noted that in these particular analyses the Si/Al was set fixed at 1.44, which is a constraint of these experiments to some extent.

It could be observed from Figure 4.6 that in both cases the CFA into zeolite conversion increases with initial alkali concentration reaching the highest indexes of roughly 80% and 95%, correspondingly. Moreover, it is interesting to emphasize that the conversion is improved by 15% when the L/S ratio has been changed from 10.625 to 20, while the reaction temperature has been decreased from 130^{o}C to 117^{o}C. The positive improvements might be taking place owing to the zeolite crystal growth initiated by the excess amount of alkali concentration, wherein the higher value of L/S creates the structural environment for a better reaction by allowing to form more active sites for Na^{+} ions to further develop zeolitic phase. Furthermore, a positive effect of the reaction time on conversion of CFA into zeolite was observed on the fuzzy model as shown in Figure 4.7a and 4.7b, which in turn was also in agreement with the experimental synthesis results. As in the previous fuzzy modeling, there are several parameters that were set constant on their initial average values.

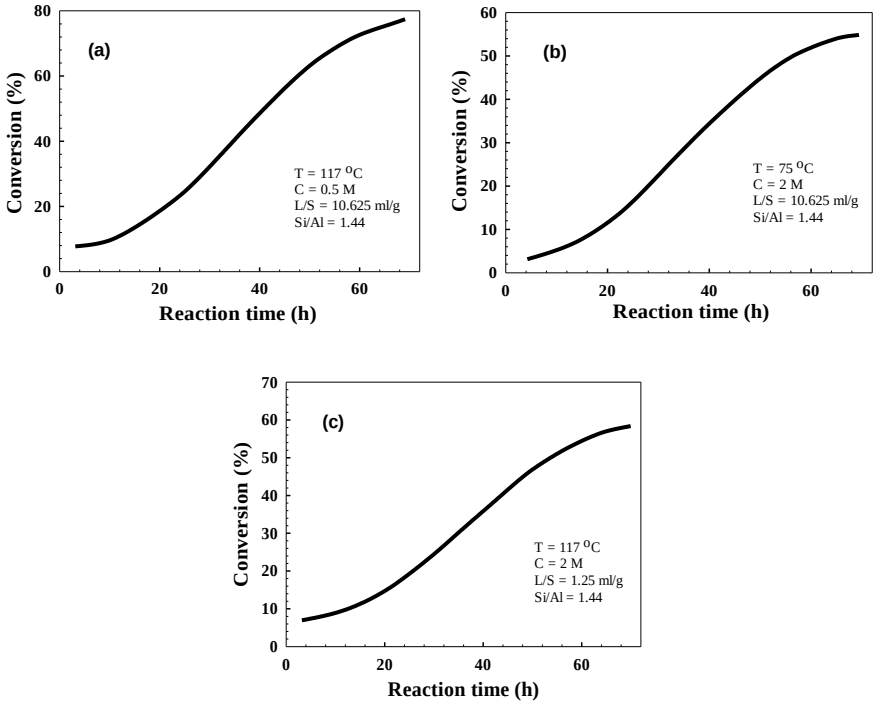

Figure 4.7. The dependence of CFA conversion into ZFA on reaction time

According to fuzzy modeling results, the conversion of CFA to zeolite progressively increases over reaction time and reaches nearly 80% and 60%, respectively. It is interesting

to note that when the temperature of the reaction has been increased by over 40°C from 75°C to 117°C, the CFA conversion to zeolite was considerably raised up to 20%. This type of trend was also observed in the experimental studies, wherein the reaction temperature significantly affected the conversion as compared with other reaction parameters. The fundamental reasons for these type of patterns, i.e. the increase of conversion over reaction time and temperature, might be interpreted by the fact that the crystal growth is a direct function of time: the more time it is allowed for crystals to grow, the higher the formation of crystals, thus CFA to ZFA conversion, which is facilitated by reaction temperature [206].

Despite the fact that the initial alkali concentration is relatively high in experimental conditions presented in Figure 4.7b, it could be seen that the effect of this parameter change is comparatively close to 0.5 M alkali concentration in terms of factors influence. In addition, in Figure 4.6 it could be observed that the *transition point*, i.e. the beginning of the curvature in the sigmoidal graph, is nearby to 2 M alkali concentration, which in turn indicates that at concentrations less than 2 M of alkali concentration, the dependence of conversion of CFA into zeolite considerably low. Figure 4.7c, double confirms the experimental outcomes and supports the hypothesis that, if the L/S ratio is reduced, it reversely affects the CFA conversion into zeolite, since less active sites of CFA are available for reaction to occur, thus for crystals to develop and grow.

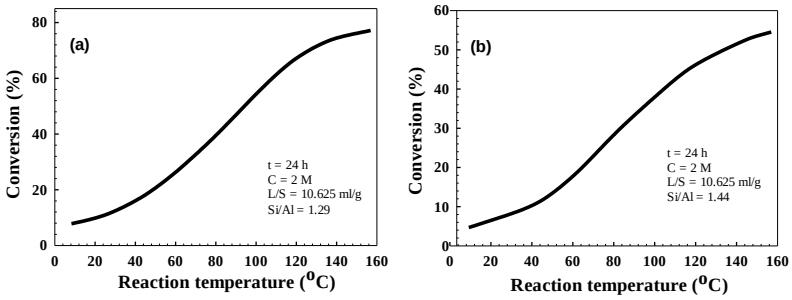

Figure 4.8. The dependence of CFA conversion into zeolite on reaction temperature with a change in Si/Al ratio

In the same way, the kinetics of zeolite synthesis has been positively affected by the reaction temperature, which in turn facilitates the development of more crystal phases that are functioned as the building blocks of zeolitic crystal formation and growth as opposed to amorphous nature of CFA (see Figure 4.8a and 4.8b). Although, there are certain constraints under experiment conditions, the effect of the Si/Al ratio has also been analyzed on

conversion of CFA into zeolite. As it is known from literature [207,208], a relatively rich Si content in parent CFA may increase the speed of crystal formation, which in turn results in improved synthesis of zeolites upon annealing at elevated temperatures provided that there is a suitable alkaline condition. The Si and Al are the main building blocks of zeolites to be converted from CFA. The more Si fraction in parent CFA may require less energy for nucleation and create more active sides for zeolite crystals to grow and propagate. Matching the Figure 4.8a and 4.8b, it could be revealed that at a comparatively moderate alteration in Si/Al ratio (from 1.29 to 1.44), a substantial positive effect in terms of conversion is observed, with about 22% increase in CFA to zeolite conversion. Additionally, Figure 4.9 shows the effect of L/S ratio on the CFA conversion into ZFAs, where a gradual ascending tendency towards higher L/S ratio could be observed, which is in corroboration with previously proposed explanations.

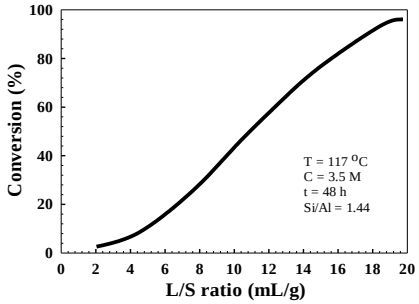

Figure 4.9. The dependence of conversion of CFA to zeolite on L/S ratio

4.6. Summary of the chapter

In order to acquire the structural and morphological data and insights of the zeolite production method, this chapter introduced a factorial analysis of CFA derived zeolite synthesis, full characterization of produced zeolites along with a conversion model employing the zero-order TS fuzzy system to optimize it. The model is devised and elaborated, utilizing the data from the literature and experiments, and is later optimized to render reliable results. The achieved results represent that the model is capable of precisely envisage the yield percentage of zeolite (up to 80%) for an addressed set of reaction parameters. The average divergence of model predictions and experiments for zeolite yield is noted to be up to 5%. Furthermore, the model helps in identifying the relationship of conversion on specific parameters that farther scatters light on mechanism of zeolite growth.

CHAPTER 5

MERCURY REMOVAL STUDIES FROM WATER

5.1. Introduction

The pollution of water resources with heavy metals, especially with Hg^{2+} and its species, is a severe global environmental issue. Mercury, due to its vaporization, persistence and bioaccumulation characteristics, is recognized as one of the most poisonous elements that seriously harm humans and the environment [104]. According to last directions of the US Environmental Protection Agency (EPA) the maximum contaminant level (MCL) of Hg^{2+} concentration in drinking water is 0.2 ppb [198]. Directive 2008/105/EC of the European Parliament and Council set up a stricter Environmental Quality Standard with maximum allowed concentration (MAC) of Hg^{2+} in surface waters of 0.07 ppb [199].

Numerous methods for the remediation of Hg^{2+} from wastewater have been employed, including the use of electrochemical treatments (electro-coagulation, electro-flotation, and electro-deposition), physicochemical processes (chemical precipitation, ion exchange) and adsorption (activated carbon, carbon nanotubes, rice husk, etc.) [200]. Of all those methods, the adsorption by utilization of waste materials is of utmost interest, as they might be a low-cost and efficient in the treatment of hazards. There are various examinations on the elimination of elemental Hg from flue gas [18,20,201,202], though, insufficient investigations were carried out on Hg^{2+} ions remediation from simulated and industrial water, especially with the utilization of CFA, ZFAs, and their composites with nanoparticles.

5.2. Focus of the chapter

Amongst all metal and metal oxide comprising composites Ag NPs containing zeolite nanocomposites have drawn significant concentration as they maintain an unusual property to develop an amalgam with Hg. Even though there are other noble metals that may form amalgams or alloys, they are comparably more pricy than silver. There are some studies in the literature on utilization of zeolites based on CFA for mercury removal, but, the investigation on Ag NPs impregnated CFA-derived zeolites for the remediation of Hg from aqueous and gaseous phases is very restricted. In the present research, CFA-based zeolites and novel Ag NPs impregnated zeolitic porous nanocomposites have been produced,

characterized and examined for Hg^{2+} removal from water solutions. The impact of the anions nature, Ag NPs loading and leaching of the adsorbed Hg^{2+} was meticulously considered. Furthermore, the study offers a detailed removal mechanism of Hg^{2+} on the nanocomposites that are endorsed by advanced characterization techniques.

5.3. Nanocomposite synthesis and characterization

The phase content of all materials was determined by XRD. The main phases of two types of Kazakhstani CFAs, ZFAs, R-ZFAs and their respective nanocomposites are shown in Figure 5.1 and 5.2. The CFA usually has 2 and more phases, wherein the major phases are mullite and quartz. Depending on location, it could also contain minerals like calcite, magnetite, hematite, etc. [165,202,209,210]. As it is clearly seen in Figure 1, K-CFA contains the mullite and quartz as predominant phases, whereas magnetite as a minor phase. After synthesis of zeolite from CFA we could observe peaks of new phases as analcime (major zeolite) and philipsite-Na (minor zeolite); while based on the intensity of peaks we could estimate that the amount of quartz and mullite are considerably diminished owing to new phase formations. If we look at the spectrum of nanocomposite 2wt.%-Ag-K-ZFA, we can clearly see the corresponding peaks of Ag NPs, which confirms that impregnation into the zeolite structure was successful.

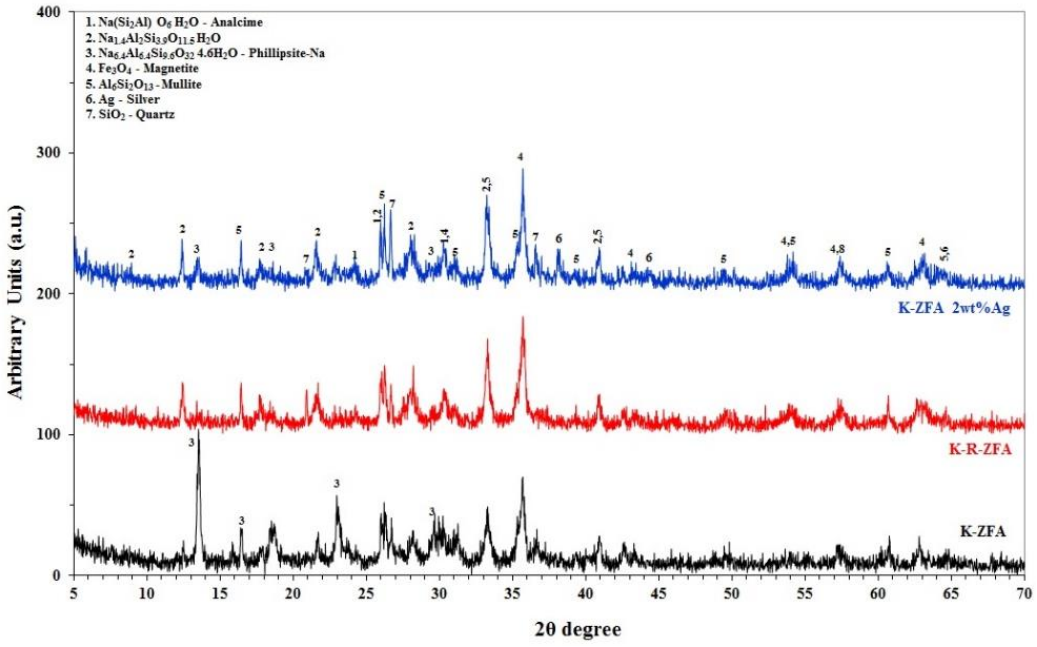

Figure 5.1. XRD spectra of K-ZFA, K-R-ZFA and 2wt.%-Ag-K-ZFA

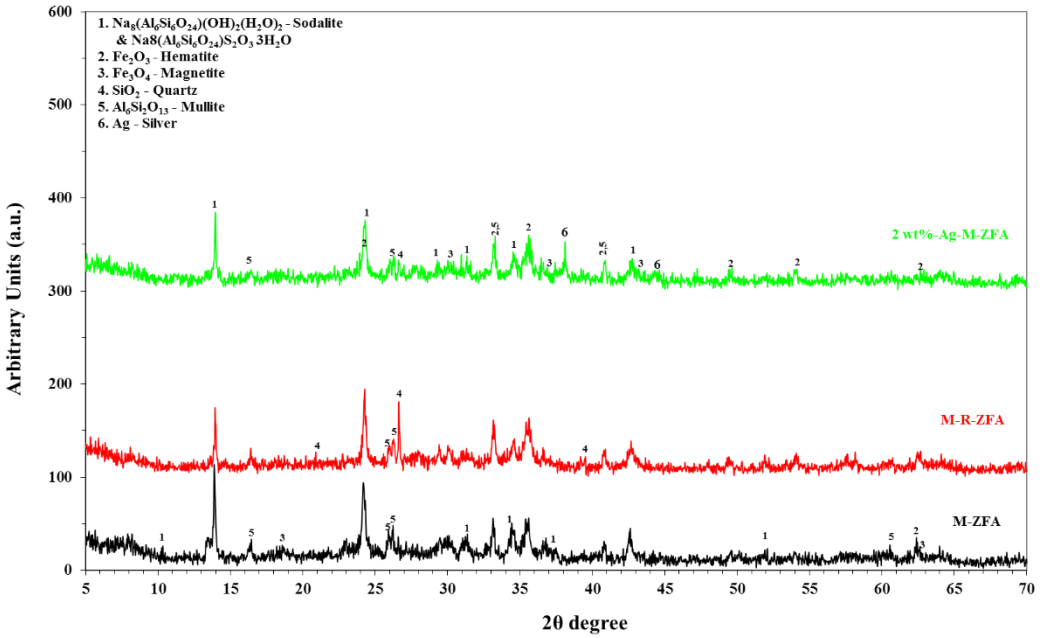

Figure 5.2. XRD spectra of M-ZFA, M-R-ZFA and 2wt.%-Ag-M-ZFA

M-CFA contains similar phases as K-CFA, which are mullite, quartz and magnetite/hematite. As shown in Figure 5.2, we could observe the comparative spectrums of M-ZFA, M-R-ZFA, and 2wt.%-Ag-M-ZFA. It is obvious from the spectrums that in addition to mullite, quartz and magnenite/hematite, M-ZFA contains another type of synthetic zeolite sodalite. These changes might be due to difference in mullite/quartz ratio in parent CFAs. If we compare M-ZFA with M-R-ZFA, we could state that there are no distinctive changes in reduced zeolite, although we assume that it may have some structural changes due to calcination. As for spectrum of 2wt.%-Ag-M-ZFA, we could observe the Ag NPs specific peaks, which confirm the formation of nanocomposite. A considerable fraction of the amorphous substrate (owing to comparatively fast cooling of CFA) has also been detected in the range of 15°-35°, wherein a characteristic diffused wide band reveals the formation of glassy phase. In case of synthetic zeolite, it is noticeable that in the course of hydrothermal treatment zeolitic phases of two types were formed. Analcime was detected as the main zeolitic phase in K-samples, wherein a sodalite was the major phase in M-samples with minor presence of Na-P zeolites. Concurrently the amounts of mullite and quartz have been substantially diminished primarily owing to their fractional dissolution and the subsequent zeolite phase growth. The spectrum acquired for the nanocomposites established

the occurrence of the metallic Ag NPs in the zeolitic matrix, by the characteristic XRD peaks of silver at 38.18º, 44.33º and 64.52º.

Table 5.1. Chemical composition of two types of CFAs, ZFAs and Ag-ZFAs

Compounds	K-CFA	K-ZFA	2%-Ag-K-ZFA	2%-Ag-M-ZFA	M-ZFA	M-CFA
Na_2O	0.678	4.447	3.405	4.796	5.858	0.763
MgO	0.716	0.708	0.646	1.139	1.145	1.423
Al_2O_3	25.761	30.888	28.245	25.882	24.859	21.750
SiO_2	49.802	32.488	30.959	31.099	32.343	44.425
SO_3	0.237	0.086	0.047	0.696	0.874	2.248
K_2O	1.324	0.150	0.119	0.234	0.260	1.857
CaO	2.798	2.390	2.089	4.533	4.696	6.775
TiO_2	1.636	1.258	1.142	0.939	0.959	1.169
Cr_2O_3	0.033	3.104	3.359	3.460	3.387	0.024
MnO	0.216	0.411	0.463	0.574	0.608	0.432
Fe_2O_3	16.076	23.066	22.389	23.105	23.578	18.138
Co_3O_4	0.028	0.061	0.060	0.088	0.070	0
NiO	0.032	0.432	0.383	0.475	0.477	0.023
CuO	0.042	0.028	0.025	0.046	0.034	0.035
ZnO	0.052	0.040	0.033	0.027	0.036	0.024
SrO	0.195	0.206	0.167	0.286	0.309	0.342
Ag_2O	0	0	2.510	2.252	0	0
BaO	0.143	0.119	0.109	0.248	0.273	0.369
CeO_2	0.126	0	0.055	0.093	0.054	0.068

The chemical composition of produced materials, on the other hand, were determined using XRF. In this method of characterization, we aimed to quantify the amount of each compound present in parent CFAs, zeolites and nanocomposites and compare two types of nanocomposites produced from different parent materials. As it is summarized in Table 5.1, we could observe that CFAs of both origin are rich in aluminosilicates (more than 65%) that

means it is of pozzolanic nature and has low amount of CaO, which in turn corresponds to Class F fly ash type according to ASTM. The Si/Al ratios of K-CFA and M-CFA are 1.65 and 1.80, respectively.

The zeolitization procedure and the formation and growth of synthetic zeolite crystals on the fly ash particles were also detected on SEM analysis. The micrographs of samples K-CFA and M-CFA along with produced ZFAs and Ag-ZFAs illustrated in Figure 5.3 indicat that the parent CFA was primarily of granular and spherical in shape, with the particle size in the range of 4 to 55 μm.

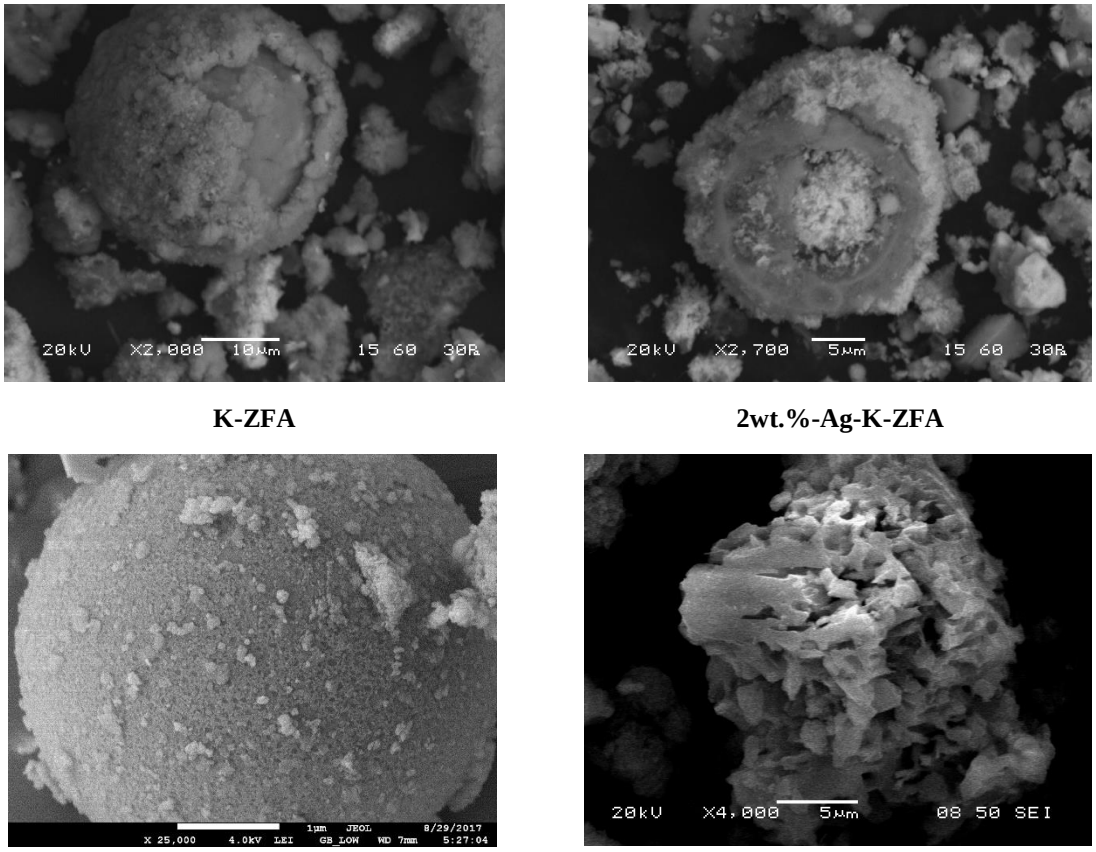

K-ZFA **2wt.%-Ag-K-ZFA**

M-CFA **2%-Ag-M-ZFA**

Figure 5.3. SEM images of K-ZFA, 2wt.%-Ag-K-ZFA and M-CFA, 2wt.%-Ag-M-ZFA

The aluminosilicate and silicate compounds of pristine CFAs, such as quartz, mullite and amorphous glass were performed as the substrate for the formation, growth and transformation of zeolite phase into Na-aluminates and silicates. Further, the formed phase facilitated the necessary nucleation sites for the evolution of zeolitic phase and triggered the

fractional growth of needle-like or fibrous Na-P1 zeolite on and inside the CFA spheres. The estimated length of zeolitic fibrous range between 1 to 2 μm. The elevated Na^+ concentration appears to have operated as the preservative of the sub-micron constructing units of the developing zeolite crystal-like structure. The formation of finer structures could be attributed to the existence of insignificant fraction of amorphous or sodalite nature developments during the transformation of zeolite that has a lower aluminum amount. In contrast, the structure was not considerably affected by the presence of Ag NPs in zeolite matrix. The agglomeration of Ag NPS on the substrate was not detected, which indicates the formation of uniform matrix with well spread particles.

The existence of Ag NPs was spotted on XRD spectrum, which is in corroboration with TEM images of Ag NPs impregnated zeolites (nanocomposites) as shown in Figure 5.4. The corresponding TEM images revealed that the metallic Ag NPs are well spread in the zeolite structure, with a negligible degree of agglomeration, which ranges from 4 to 45 nm. In majority of cases the shape and size of particles are explicit and spherical with a mean size of 10 to 15 nm. The presence of Ag NPs were confirmed with EDS elemental analysis. Additional FTIR spectrums of nanocomposites and TEM images and of nanocomposites before and after Hg^{2+} adsorption could be found in Figures C1-C4.

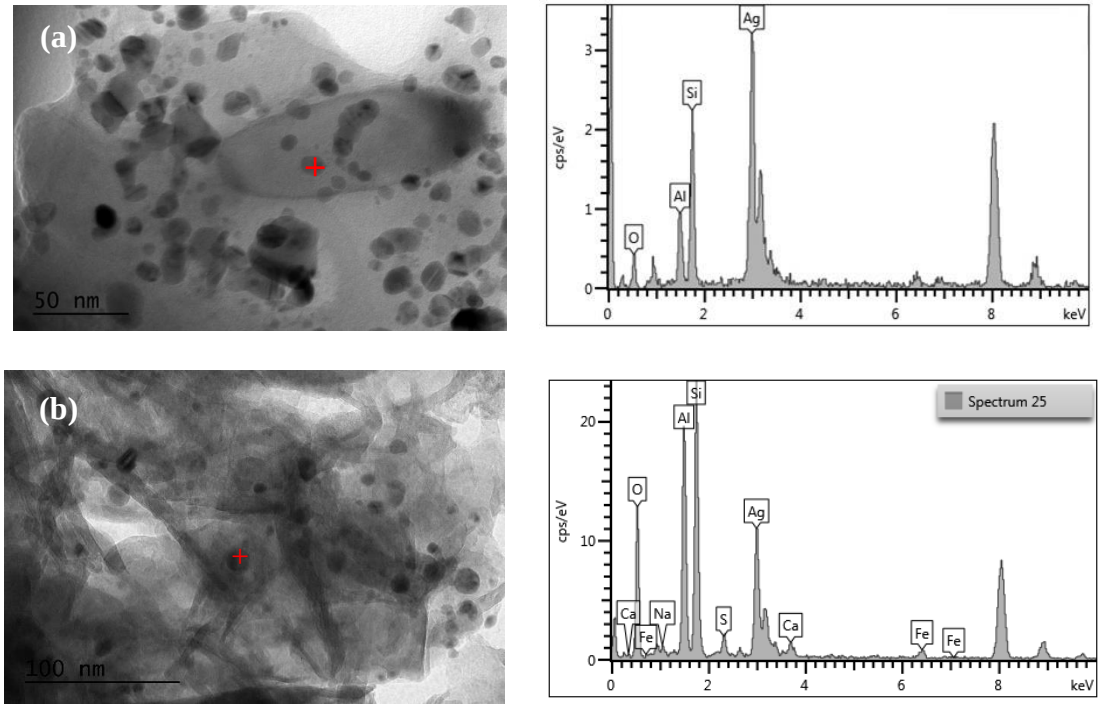

Figure 5.4. TEM and EDS of 2wt.%-Ag-K-ZFA (a) and 2wt.%-Ag-M-ZFA (b)

The specific surface area (SSA) results as shown in Table 5.2 reveals that the BET surface area of parent CFA is the lowest for both samples as expected. It is generally condidered that the CFA based ZFAs normally have the specific surface area (SSA) that starts from 8 m^2/g and could reach up to 75 m^2/g [211–213] with predominantly micro- and meso-porous structure. The literature results are in agreement with the acquired data, as the BET values of the produced sodalite and analcime demonstrated 56 and 61 m^2/g. The reduced zeolites (R-K-ZFA and R-M-ZFA) have on average ~30% lower SSA than zeolites, which in turn could be linked to high temperature calcination process during synthesis, which possibly caused the transformation of the primary matrix with a relatively fine pores and resulted in shifting to a larger pores. The nanocomposites of both samples show a decreased BET surface of 34 and 51 m^2/g, also the average pore size and pore volume is relatively lower, indicating fractional blockage of the micro- and mesopores due to Ag NPS impregnation, which is similar to results obtained by Wdowin *et al*. [22].

Table 5.2. BET surface areas of materials

Material type	BET surface area [m^2/g]	Average pore size [nm]	Total pore volume [cm^3/g]
K-CFA	18 ± 15	10 ± 2.0	0.04 ± 0.02
M-CFA	20 ± 7.0	15 ± 4.0	0.07 ± 0.05
K-ZFA	56 ± 12	14 ± 0.2	0.25 ± 0.01
M-ZFA	61 ± 12	17 ± 3.0	0.26 ± 0.08
R-K-ZFA	38 ± 8.0	15 ± 0.1	0.16 ± 0.09
R-M-ZFA	47 ± 3.0	16 ± 4.0	0.27 ± 0.12
2wt.%-Ag-K-ZFA	34 ± 12	15 ± 3.9	0.22 ± 0.07
2wt.%-Ag-M-ZFA	51 ± 1.0	10 ± 0.1	0.13 ± 0.05

Table 5.3 shows the results of particle size analysis of parent CFAs, ZFAs and nanocomposites. According to analysis, the reduced samples (8.5±0.3 μm) and Ag NPs containing composites (16.6±0.36 μm) revealed a smaller average particle size than the raw CFAs and ZFAs. The average particle size of K-ZFA and M-ZFA ranges between 25±0.8

and 28±0.8 μm. The corresponding values for Ag-ZFAs were at 13.2±0.02 and 20±0.70 μm, respectively. These results could be correlated to the agglomeration phenomena of the tiny particles of freshly prepared zeolites that have been eliminated after annealing, largely due to the removal of entrapped water at higher temperatures. This may influence the kinetics, as the adsorption rate is faster when the particle size is smaller.

Table 5.3. PSD analysis of materials (μm)

PSD	K-CFA	M-CFA	K-ZFA	M-ZFA	2wt.%-Ag-K-ZFA	2wt.%-Ag-M-ZFA
Dv(10)	22±2.4	9 ±2.4	6 ± 0.3	8 ± 0.3	2.44±0.01	4±0.15
Dv(50)	57±0.03	67±0.03	25±0.8	28 ±0.8	13.2±0.02	20±0.70
Dv(90)	161±5.7	428±5.7	66±0.8	157±0.8	55.7±0.05	57±0.07

5.4. Adsorption kinetics and mechanism studies

In the course of kinetic experiments pH increased from 2.0 to 3.5 for the CFA and about 6.25 for the rest of samples, whereas the conductance reduced from 2680 μS/cm to 840 μS/cm and 980 μS/cm for K-CFA and M-CFA, respectively. The other samples decreased to ca. 750-760 μS/cm. The final pH of the solution and conductance values were detected for the ZFAs in blank solutions, i.e. ZFA in ultra-pure water. Therefore, the decrease in the conductance could be correlated with the cation exchange reaction of H^+ in solution and Na^+ on the surface owing to the substantial variance in corresponding conductivities, which is 34.96 mS m^2/mol for the former and 5.01 mS m^2/mol for the latter at 25°C [214].

The adsorption kinetics of nanocomposites 2wt.%-Ag-K-ZFA and 2wt.%-Ag-M-ZFA show that it reached equilibrium removal of ~99% in less than 24 hours, while it took 14 days and 12 days for K-ZFA and M-ZFA to remove and reach the equilibrium at 91.3 % and 82%, respectively. The reduced samples of corresponding ZFAs revealed a much lower removal profile at 77.5% and 66% for R-K-ZFA and R-M-ZFA only after 21 days and 14 days, whereas the lowest and slowest removal profile were established by CFAs (Figure 5.5). The fast and efficient sequestration of Hg^{2+} reveals a combination of removal mechanism in

nanocomposites in contrast with zeolites and reduced zeolites. The parent CFA of both nanocomposites demonstrated a poor adsorption behavior of Hg^{2+} ions from water as expected, which is explained by the low BET surface area and less active sites for physisorption. Therefore, the removal rate and maximum removal at equilibrium for studied materials follow this order: 2wt.%-Ag-ZFA > ZFA > R-ZFA >> CFA. This order is in alignment with the BET values pattern of the parent and produced solids, which in turn confirms that the adsorption is the principal mechanism of retention in parent CFAs, ZFAs and R-ZFAs, while the retention of Hg^{2+} ions with Ag-ZFAs is predominantly *via* amalgamation followed by adsorption or surface precipitation.

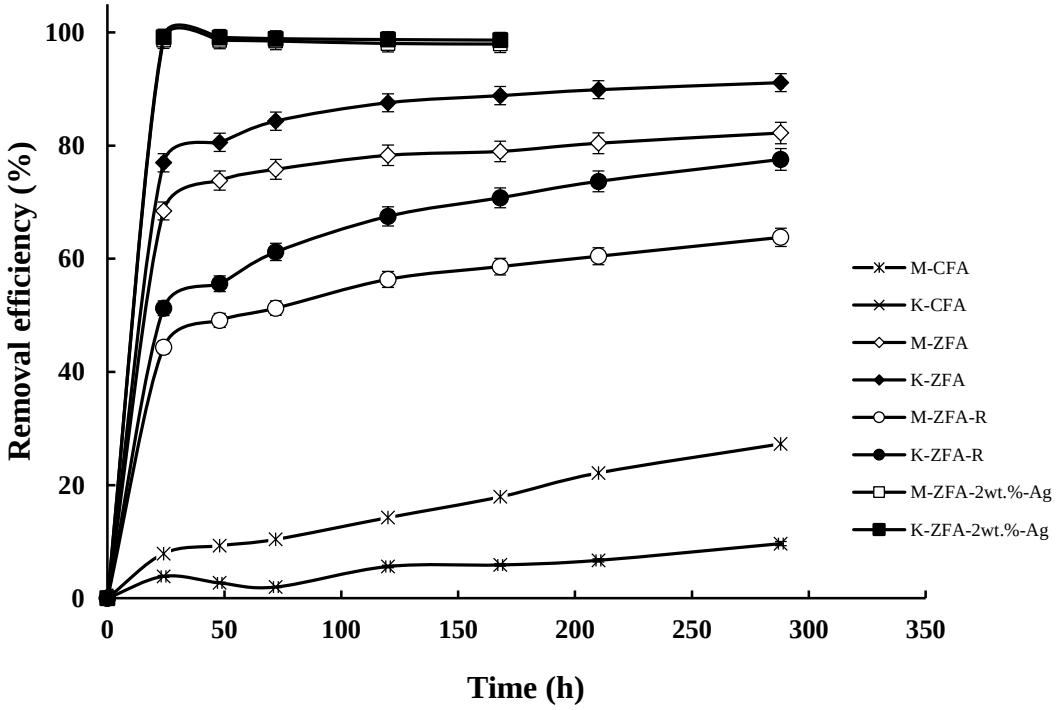

Figure 5.5. Adsorption kinetics of Hg^{2+} in water (10 ppm; 0.3 g in 40 mL; pH 2.0)

The characterization results reveal that on average the size of particle of the nanocomposite is smaller than of parent zeolite, which might affect the adsorption rates in the former. However, despite the fact that R-ZFAs have even smaller size of the particles they demonstrate considerably slower adsorption kinetics profile in comparison with Ag-ZFAs. This assist to propose a hypothesis that the adsorption rate in nanocomposites is not only controlled by the particle size. Therefore, the SSA of material, shape and size of the particle

may not fully explain the outcomes. According to proposed hypothesis of mechanism of Hg^{2+} removal, there is additional prominently contributing factor that could be related to the reduction and oxidation reactions between $Ag°/Ag^{+}$ (+0.80 V) and $Hg^{2+}/Hg°$ (+0.85 V) [215,216], which take place owing to similar values of the standard redox potentials of these two metals. This work supports the hypothesis of co-existing removal mechanisms, which combines the typical surface adsorption, the precipitation of Hg^{2+} reduced to Hg° on the surface of material and amalgamation or alloy formation between two metals (Ag_xHg_y). The research carried out on the development of selective sensors for detection of Hg and adsorption of trace amounts of Hg by means of Ag NPs doped matrix claim to have an amalgam formation of two metals *via* Hg-Ag interaction [217,218]. The work on the possible reactions that take place between Hg and Ag carried out by Pang and Ritchie [219] in 1982 describes a comparative study of the dissolution and displacement reactions, wherein the two metals undergo the amalgamation reaction.

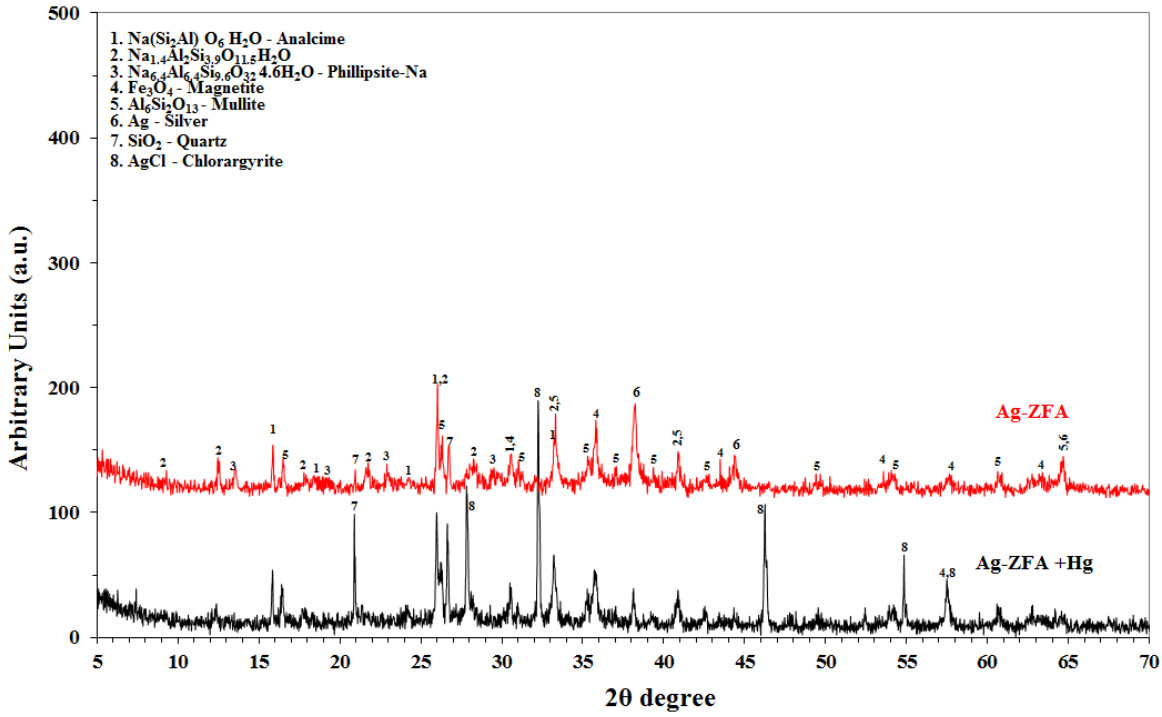

Figure 5.6. XRD spectra of ZFA and Ag-ZFA with Hg^{2+}

Figure 5.6 shows the comparative XRD characteristic spectrums of Ag NP impregnated 2wt.%-Ag-K-ZFA before and after adsorption of Hg (II). It is clearly seen from the XRD spectrums that the major characteristic peaks of Ag NPs in mercury-adsorbed

nanocomposite have significantly decreased in intensity. This was followed by the formation of high intensity silver chloride (AgCl) peaks on XRD spectrums of 2wt.%-Ag-K-ZFA after adsorption. These noticeable alterations in spectrums, in turn, support the hypothesis of Hg^{2+} removal mechanism as shown in Figure 5.7. Likewise, fading of Ag NPs characteristic peaks upon contact with Hg was also detected elsewhere [216], wherein the authors discovered the growth of paraschachnerite Ag_3Hg_2 with orthorhombic crystalline structure. The reduction of Hg^{2+} followed by amalgam formation with silver were also observed by other researchers [33,215], wherein authors suggested the probable mechanism of reactions between two metals. The reaction mechanism according to this approach includes the amalgamation and reduction of Hg (II):

$$Ag_m + (m/2)\ Hg^{2+} \rightarrow {}_mAg^{+} + (m/2)\ Hg \tag{5.1}$$

$$Ag_n + Hg^{2+} \rightarrow Ag_{(n-2)}Hg + 2Ag^{+} \tag{5.2}$$

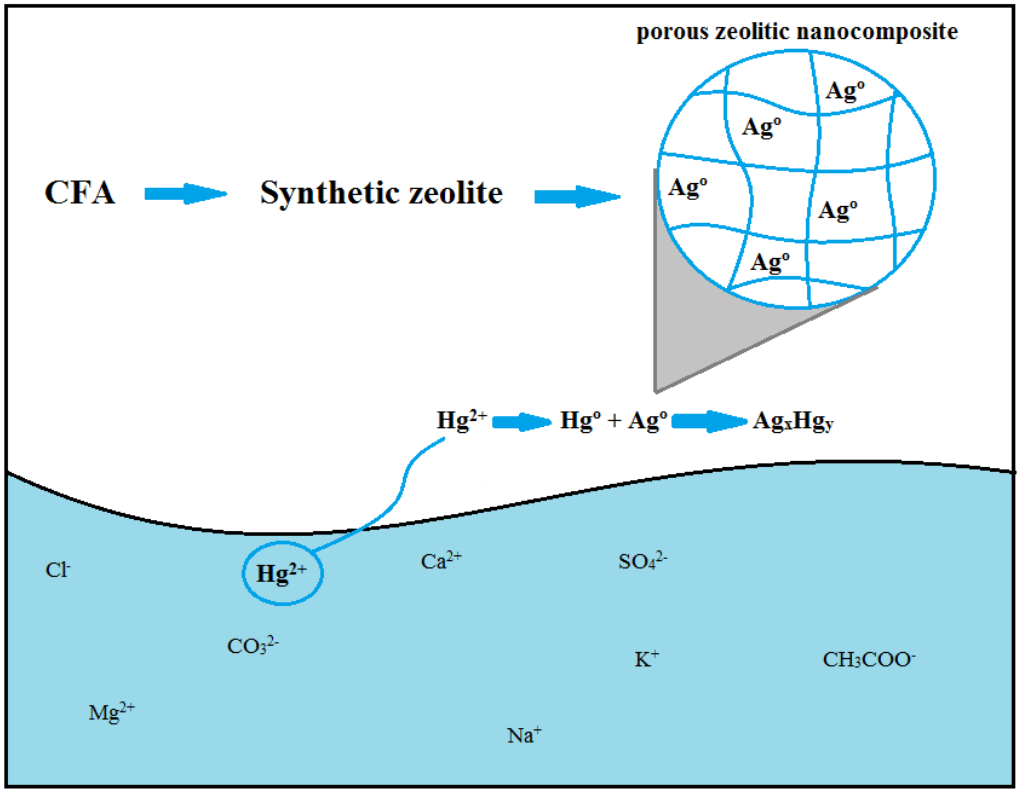

Figure 5.7. Schematic diagram of Hg^{2+} removal using nanocomposites *via* amalgamation

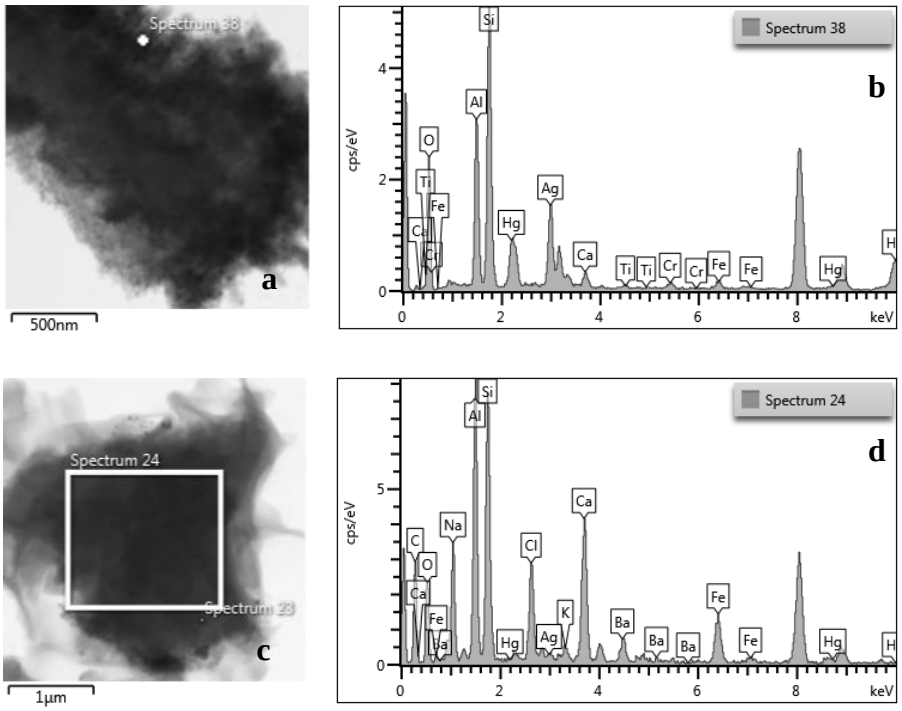

Figure 5.8. TEM and EDS analysis of 2wt.%-Ag-K-ZFA (a, b) and 2wt.%-Ag-M-ZFA (c, d) loaded with Hg^{2+}

The study of the nanocomposite 2wt.%-Ag-K-ZFA loaded with Hg^{2+} under the TEM-EDS and mapping (Figure 5.8) exposed the nature of the new formation. In case of samples loaded with Hg^{2+}, the metallic Ag particles have been significantly reduced in quantity and in size, presenting a distribution with an average size of 10-20 nm.

It is interesting to note that a metallic Hg was additionally observed along with adsorbed and bound in the nanocomposite structure, which permanently co-existed with the metallic Ag in the form of poorly spread agglomerated fluid formations, developing dark long fibrils or non-transmitted large spots (Figure 5.9).

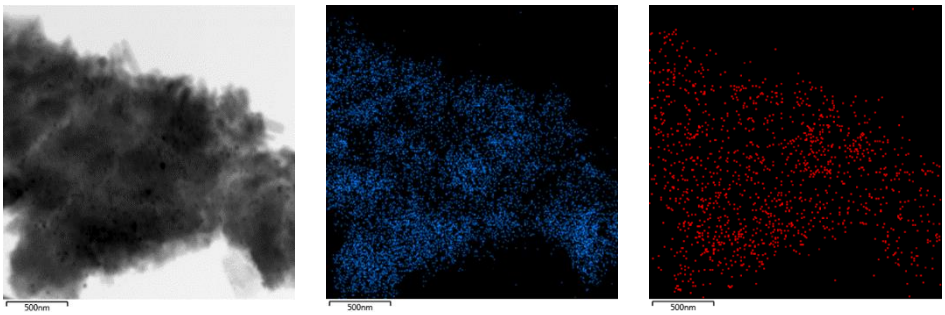

STEM micrograph **Hg – Mercury** **Ag – Silver**

Figure 5.9. TEM mapping of 2wt.%-Ag-K-ZFA loaded with Hg^{2+}

Another important factor that needs to be examined and has a high potential effect on the removal performance of the nanocomposite towards Hg^{2+} is the charge of the surface of solids. This could be investigated by determination of the point of zero charge (pH_{ZPC}), which regulates the electrophoretic mobility wherein the net charge of the particle is zero. The experimental results revealed that the pH_{ZPC} of ZFAs and nanocomposites varies between 4.5-5.0 (Figure 5.10).

The obtained data on pH_{ZPC} of nanocomposites entails that under pH that is < 4.5, wherein the major fraction of Hg^{2+} is potentially removed from solution, the ZFA and nanocomposite have a positively charged surface that ought to initiate the repulsion force towards Hg^{2+} cations. However, there is a vital underestimated aspect in the speciation of ions in solution, which in most cases overlooked and uncovered in the related literature, particularly this become of utmost importance in co-existence of complexing counter ions such as Cl^-.

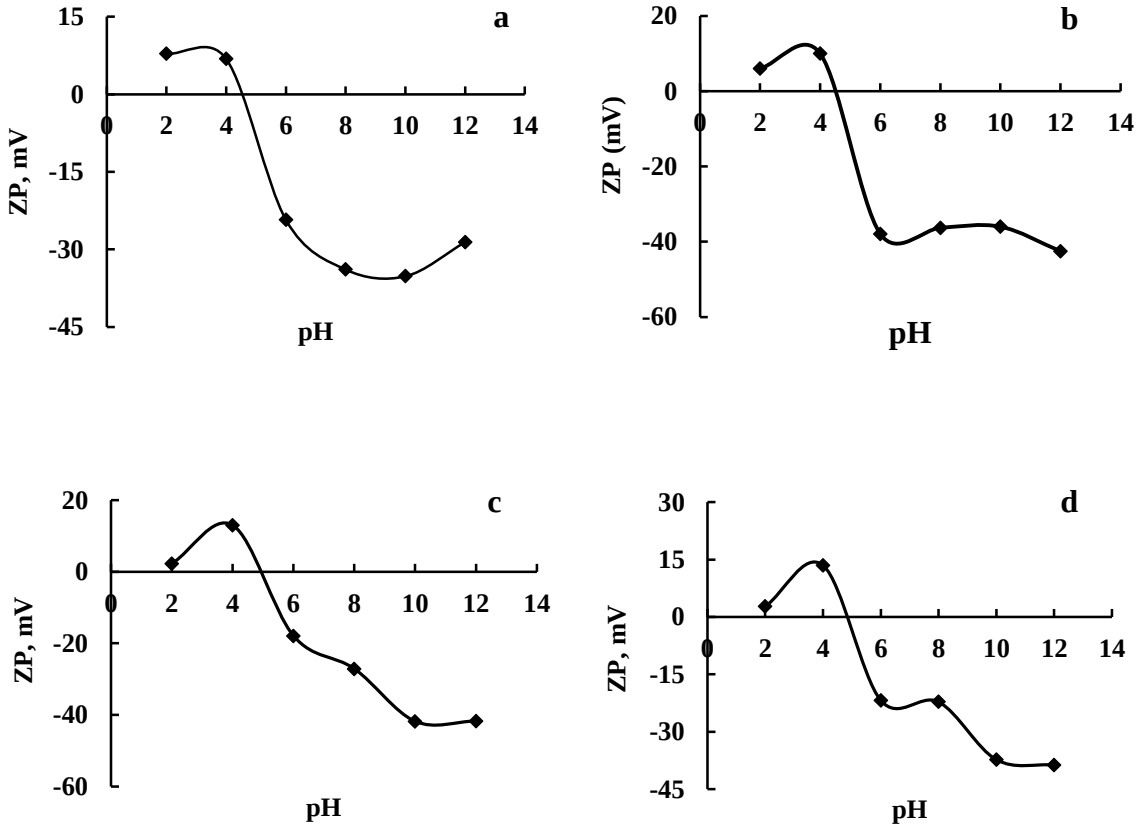

Figure 5.10. Zeta potential values at different pH: K-ZFA (a); 2wt.%-Ag-K-ZFA (b); M-CFA (c); 2wt.%-Ag-M-ZFA (d)

The speciation diagram of the system under study with specific concentrations of each existing ion is displayed in Figure 5.11. It is clearly seen that under strong acidic phases before reaching the pH < 4.5, the main species that might exist are a neutral soluble $HgCl_2$.Therefore, the removal of Hg^{2+} species from solution under these experimental conditions has potentially no effect by the surface charge of material. These results allow to conclude that the mechanism of nanocomposite is complex and comprised of amalgamation followed by adsorption and precipitation; whereas the parent CFA, ZFA and R-ZFA undergoes an adsorption.

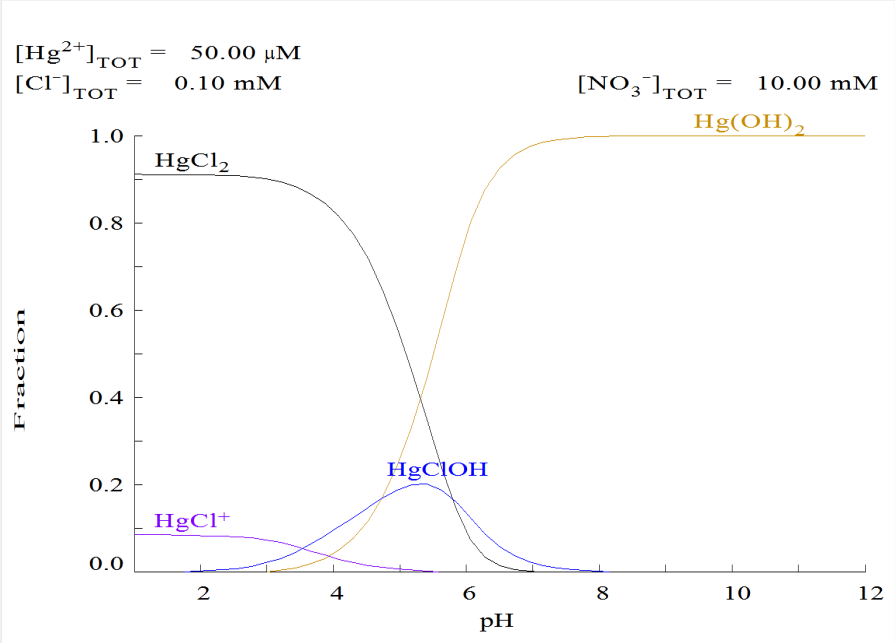

Figure 5.11. Speciation of 10 ppm Hg^{2+} solution (0.05 mmol Hg^{2+}, 0.1 mmol Cl^-)
[Diagram created on Medusa speciation software]

5.5. Adsorption equilibrium isotherms

The adsorption equilibrium of zeolites and nanocomposites are shown in Figures 5.12 and 5.13. According to results, the ZFAs (analcime and sodalite) have the maximum adsorption capacity of 4.5-5.8 mg/g, while the corresponding nanocomposites reveal 20.3-24.4 mg/g (2wt.%-Ag-K-ZFA and 2wt.%-Ag-M-ZFA). These entails that the adsorption behavior is inherently diverse than in parent zeolites as hypothesized. The molar ratio calculations further entails a hyper-stoichiometric profile in nanocomposites. For instance, if the

maximum adsorption capacity of 2wt.%-Ag-K-ZFA is taken as 20.3 mg/g and 4.5 mg/g for K-ZFA. The difference due to amalgamation reaction between Hg and Ag metals constitute 15.8 mg/g or 0.079 moles of Hg. According to the XRF results, the nanocomposite 2wt.%-Ag-K-ZFA experimentally contain 2.33% of Ag, which is 23.3 mg/g or 0.215 moles. Thus, the molar ratio of Hg:Ag would be 0.37. A similar calculation with 2wt.%-Ag-M-ZFA provides a molar ratio of Hg;Ag to be 0.46. This in turn suggests that the nanocomposites might have the formation of amalgam or alloy with an empirical formula of paraschachnerite Ag_3Hg_2 with a hyper-stoichiometry.

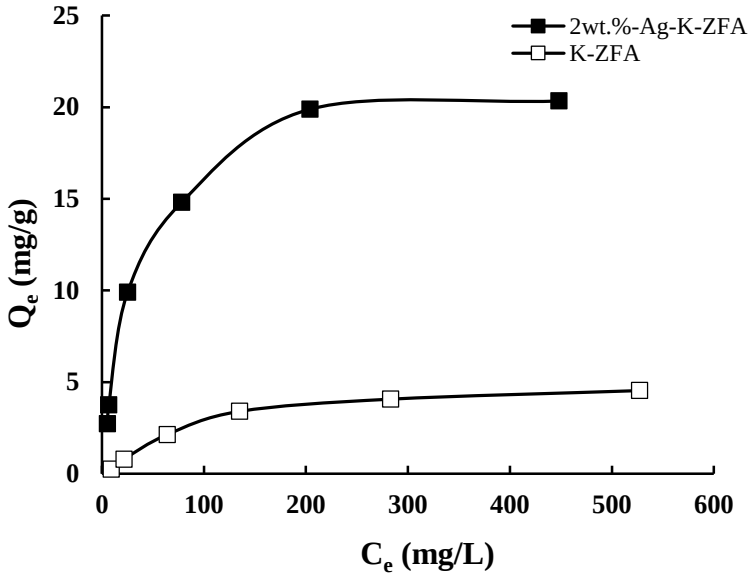

Figure 5.12. The adsorption equilibrium isotherms of K-ZFA and 2wt.%-Ag-K-ZFA

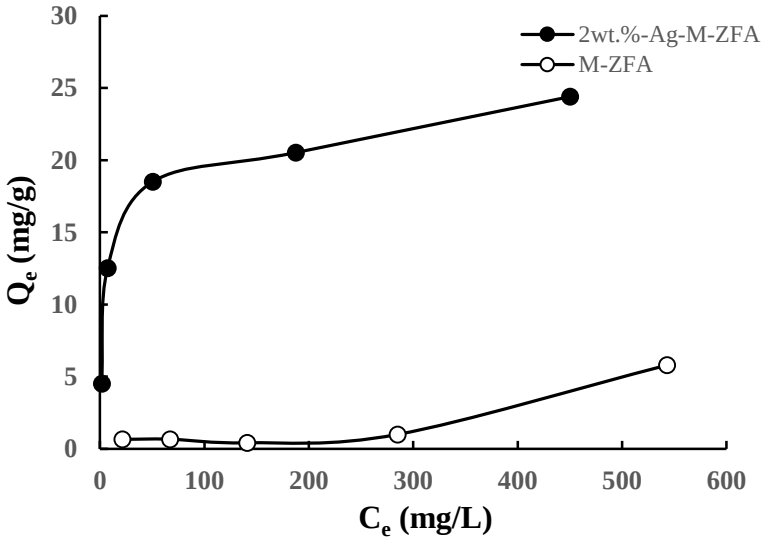

Figure 5.13. The adsorption equilibrium isotherms of M-ZFA and 2wt.%-Ag-M-ZFA

5.6. Leaching studies and maximum adsorption capacity

It is of utmost importance to examine the leaching or desorption level of adsorbed Hg^{2+} in nanocomposite and zeolites, as the critical aim of the study is a safe storing of the adsorbed toxic and hazardous species either in ionic, elemental or compound state. According to the outcomes, less than 1% of adsorbed Hg^{2+} was leached out from the nanocomposites demonstrating the remarkable storage capacity under both strong acidic and neutral conditions. These obtained values are 4 to 8 fold lower than in corresponding ZFAs as shown in Table 5.4.

Table 5.4. Leaching experiment of Hg^{2+} from K-samples under acidic and neutral media

Adsorbent type	Total adsorbed Hg [mg]	Leached Hg after 12 days [mg]	Leached Hg after 12 days [%]
K-CFA (pH 7.0)	0.92	0.015	1.63
K-CFA (pH 2.0)	0.95	0.065	6.84
K-ZFA (pH 7.0)	6.06	0.195	3.22
K-ZFA (pH 2.0)	5.88	0.215	3.66
R-K-ZFA (pH 7.0)	4.25	0.230	5.41
R-K-ZFA (pH 2.0)	4.14	0.365	8.82
2wt.%-Ag-K-ZFA (pH 7.0)	7.69	0.060	0.78
2wt.%-Ag-K-ZFA (pH 2.0)	7.69	0.070	0.86

Similar leaching investigations carried out elsewhere [165] revealed a considerably more leaching effect from raw CFAs compared to zeolites owing to the material properties, which supports the acquired results. Therefore, it could be concluded that the adsorbed Hg^{2+} within the matrix of the CFA-derived nanocomposite might be safely stored and utilized in natural systems with some pre-treatment. Furthermore, the results confirm the proposed hypothesis that nanocomposites with Ag NPs have a rather diverse adsorption mechanism (more possibly amalgamation or alloy formation) than in pristine zeolites, where primary mechanism of removal is physical adsorption.

Another interesting study is the maximum adsorption capacity of the ZFA and nanocomposite that was measured to be 0.4 and 6 mg/g, correspondingly. The outcomes indicate that the Ag NPs further improve the capacity of composite by demonstrating an enhanced adsorption capacity compared with the pristine zeolite. The maximum capacity values differ from the results obtained in adsorption kinetics experiments, however it should be noted that the maximum capacity is measured under intense conditions of repeated equilibrations, resulting in local selectivity differences. Similar deviations were observed in literature, where authors studied adsorption of metals by plotting isotherms and measuring the maximum capacity (maximum exchange levels) [220,221].

5.7. Effect of the silver loading in nanocomposite

The concentration change over time of the Hg^{2+} due to adsorption on nanocomposites with different Ag NPs loading revealed that the amount of Ag NPs within the matrix of nanocomposite has a direct relation to the adsorption capacity and adsorption dynamics. The elemental analysis of nanocomposites present the estimated content of Ag NPs, which confirms the formation of nanocomposite with several Ag NPs loading with close to theoretical indexes. For instance, 0.2wt.%-Ag-ZFA removed 79.7% of Hg^{2+} in 9 days and reached equilibrium, wherein 0.4wt.%-Ag-K-ZFA and 1wt.% Ag-ZFA could remove 90.74% and 96.36% in just 2 days, respectively (Table 5.5).

Table 5.5. A comparative Hg^{2+} adsorption capacity of nanocomposites

Nanocomposite	Removal after 2 days [%]	Removal after 9 days [%]	Removal after 11 days [%]
0.2wt.%-Ag-K-ZFA	69.97	78.25	79.70
0.4wt.%-Ag-K-ZFA	90.74	90.64	90.67
1wt.%-Ag-K-ZFA	96.36	95.72	95.52

The average size of particles of nanocomposites is very similar, thus it might be proposed that the kinetics in these materials are associated with Ag NPs loading. It was identified that the adsorption capacity of the produced nanocomposites are directly related with the Ag NPs loading and follow this order: 0.2wt.%-Ag-ZFA < 0.4wt.%-Ag-ZFA < 1wt.%-Ag-ZFA < 2wt.%-Ag-ZFA. The experimental values of Ag NPs content within nanocomposites are shown in Table 5.6.

Table 5.6. Chemical composition of silver-loaded nanocomposites

Compounds	0.2wt.%-Ag-K-ZFA	0.4wt.%-Ag-K-ZFA	1.0wt.%-Ag-K-ZFA	2.0wt.%-Ag-K-ZFA
Na_2O	4.369	4.272	3.557	3.405
MgO	0.758	0.677	0.651	0.646
Al_2O_3	29.984	29.637	29.201	28.245
SiO_2	31.596	31.357	31.237	30.959
SO_3	0.076	0.080	0.060	0.047
K_2O	0.142	0.172	0.141	0.119
CaO	2.332	2.274	2.162	2.089
TiO_2	1.156	1.111	1.159	1.142
Cr_2O_3	3.302	3.174	2.890	3.359
MnO	0.482	0.491	0.466	0.463
Fe_2O_3	24.595	25.340	26.494	22.389
Ag_2O	0.161	0.361	0.989	2.510

5.8. Effect of the co-existing anions

In order to comprehend the effect of the co-existing anions on adsorption of Hg^{2+} from water, four types of anions, namely CH_3COO^-, SO_4^{2-}, NO_3^- and Cl^-, were examined to correlate the possible influence of the ions on the retention of Hg^{2+} from simulated water. According to 48-hour studies, the nanocomposite 2wt.%-Ag-K-ZFA could uptake 99% of Hg^{2+} when the co-existing anions is Cl^-, while SO_4^{2-} and Ac^- presented similar uptakes of Hg^{2+} at 83.3% and 80.1%, respectively. The lowest retention of Hg^{2+} was detected for NO_3^- that revealed almost

71%. According to findings, the adsorption kinetics dependence on anions nature at the initial 48 hours follow this order: Cl^- >> $SO4^{2-}$ > Ac^- > NO_3^-. These results show a relative effect of the anions during the set duration of adsorption that might be related to the radii, presence of oxygen and affinity of the particular anion to nanocomposite matrix.

5.9. Summary of the chapter

In this chapter, ZFAs produced from CFA were converted to corresponding Ag NPs impregnated nanocomposites with various loadings of Ag NPs that was followed by multiple confirmation of phase development employing advanced characterization methods, such as TEM-EDS, SEM, XRD, XRF, PSA, porosimetry and zeta potential measurements. The produced nanocomposites were further meticulously investigated for the uptake of Hg^{2+} from simulated water solutions by conducting the adsorption kinetics, adsorption equilibrium isotherms, studying the influence of the anions nature and Ag NPs loading. The outcomes proved that nanocomposites can remove up to 99% of Hg^{2+}, which is on average up to 20% and 90% higher than the removal effectiveness exhibited by parent zeolites and CFAs, accordingly. According to findings, the Hg^{2+} removal mechanism is complex, comprising an adsorption, surface precipitation and amalgamation that was proved by applying multiple characterization techniques. The removal is higher with the increase of Ag NPs amount in nanocomposite matrix, while the kinetics rate follow the order of Cl^- >> SO_4^{2-} > Ac^- > NO_3^- depending on anions nature. The leaching studies further illustrated the advantage of the nanocomposite materials both in terms of Hg^{2+} removal and retention, which in turn broadens the possible application fields of novel nanocomposites. One possible way to recover and reuse the materials after remediation is a thermal treatment. The materials could be thermally treated under elevated temperatures to entrap the evaporated Hg for further use or storage. The materials after thermal treatment might be reused provided that there are no structural damage. However, the cost-benefit analysis should be conducted in order to evaluate the feasibility of the method.

CHAPTER 6

IODIDE REMOVAL STUDIES FROM WATER

6.1. Introduction

The presence of I^- in water resources has several causes and has attracted the attention due to the hazardousness it may pose, especially in its radioactive state or when combined with organic substances. A natural source of I^- is a seawater which may migrate into drinking water aquifers leading to elevated I^- concentrations [133]. The most serious anthropogenic source is the nuclear energy stations, which produce various radioactive wastes, including radioactive isotopes of iodine used in uranium fission [118]. The requirement for proper utilization of radioactive waste rose globally after the nuclear power accidents in Fukushima (Japan, 2011) and earlier in Chernobyl (Ukraine, 1986) that caused the discharge of radioactive iodine, which in turn was the source for development of radioactive I^- that drastically harmed the environment [117]. Other sources of radioactive I^- waste are the biological and medical applications, which also pollute the water resources [137].

The ^{129}I and ^{131}I radioactive isotopes of iodine could readily be dissolved in water and sublimated in the air causing various problems to the ecosystem [34,117]. The radioactive isotopes of iodine may cause long-term risks owing to their prolonged half-life and might negatively affect the human metabolic processes [117,119,121]. On the other hand, the ^{127}I isotope of iodine and its ionic form (I^-) is not a potential harm for human and surrounding environment [192,222–224]. It is generally used as an important precursor of iodinated products applied for the disinfection of drinking water [34,225]. However, under the oxidative treatment used in water treatment, I^- might form organic containing by-products, which may be a health concern [191]. Hence, all these issues require an effective approach of sequestration of radioactive I_2 and I^- from both aqueous and gaseous media.

There are several existing purification approaches that are typically applied for removal of I^- from water such as anion exchange, which however is not highly selective and also introduces other anions into the water. The most attractive and highly selective method is precipitation that utilizes the low solubility of metal iodides, such as AgI formation.

Table 6.1. Adsorbents for the removal of I^- from the aqueous phase

Adsorbent type	Surface area [m^2/g]	Ag conc. [%]	Initial I^- conc. [ppm]	pH	Adsorption capacity [mg/g]	Ref.
Ag@activated carbon	941	1.05	0-450	8.0	25.4-38.1	[130]
Ag_2O@$Mg(OH)_2$	78.19	34.74	300	7.0	368.6	[226]
Ag_2O-Ag_2O_3@ZIF-8	369.9	20	0-600	-	232.12	[227]
Bimetallic AgCu/Cu_2O hybrid	-	-	100	3.0	65.9	[34]
AgII-doped MIL-101	2513	2.00	500	3.0	43.2	[135]
1.0%-Ag@Cu_2O	-	1.00	20	7.0	25.4	[122]
Ag-doped carbon aerogels	428	10	1.27	7.0	0.25	[191]
3D Ag_2O-Ag/TiO_2	153.7	5.82	1150	-	207.6	[137]
MIL-101(Cr)-SO_3Ag	-	30.44	127-2305	7.5	244.2	[133]
Ag-Ag_2O modified on carbon spheres	-	6.62	-	2.1	374.91	[228]
Ag_2O grafted titanate nanoalumina	143	-	500	-	428	[118]
AgCl@caclium alginate	-	10.89	0-700	6.0	133	[133]
Ag-cloths	< 5	-	3.2	7.8	1.12-1.66	[229]
Montmorillonite-magnetite NPs	148.8	-	1000	3.0	322.42	[117]
Porous Bi_2O_3/LDH composite	235.07	-	200	7.0	101.2	[194]
Cu_2S	6	-	12.7	7.0	6.1	[230]
Cu_2O	-	-	20	7.0	2.54	[119]
Nano Cu_2O/Cu-C	1220	-	1-30	7.0	41.2	[195]
Modified zeolite ODTMA	-	-	500	4.0	4.0	[231]

However, the method of direct precipitation of I^- is particularly problematic in water treatment due to the chemistry of AgI in water, as it forms small crystalline particles and even colloids, which are very difficult to effectively remove by precipitation [191]. A way to overcome this drawback is to use supported metals on substrates and remove I^- *via* chemical adsorption. Iodide has been removed from aqueous media by means of various porous and non-porous adsorbents doped with metal nanoparticles (NPs) and metal oxides. Table 6.1 summarizes the silver containing adsorbents used for I^- removal.

6.2. Focus of the chapter

The main drawback of these studies is that the potential leaching of loaded silver and dissolution of precipitated or adsorbed AgI back into solution was not thoroughly investigated and mostly qualitatively confirmed the formation of AgI via surface characterization methods. Besides the surface interactions, the published studies do not consider the water chemistry of I^- and the potential effects of redox reactions that can take place in the solution phase. It is important to note that in most studies the reported adsorption capacity is a sum of the I^- removed by a surface precipitation and physical adsorption, as in Hoskins *et al*. [130] or the above combined to external precipitation as in Zhao *et al*. [133]. Thus, a more detailed qualitative and quantitative examination of the mechanism of I^- removal and proper quantification of adsorbed and leached I^- is required. In this chapter, the mechanism of I^- removal is discussed in detail and confirmed *via* advanced characterization methods and backed by a variety of experiments and the application of a diffusion-based model which enables the estimation of the solid phase diffusion coefficient.

6.3. Nanocomposite synthesis and characterization

XRD spectra of both nanocomposites before adsorption of I^- from water show a characteristic peak of Ag NPs at 38.18º and 64.52º in zeolite matrix as shown in Figure 6.1. This confirms the production of ZFA from CFA and formation of metallic Ag NPs within nanocomposite matrix. During the hydrothermal treatment of CFA, two major zeolitic phases were produced. Analcime was observed as the main zeolitic phase in 2wt.%-Ag-K-ZFA a nanocomposite, whereas the sodalite was formed in 2wt.%-Ag-M-ZFA

nanocomposite. The mineralogical compositions of parent CFAs and synthesized zeolites can be found elsewhere [1,7].

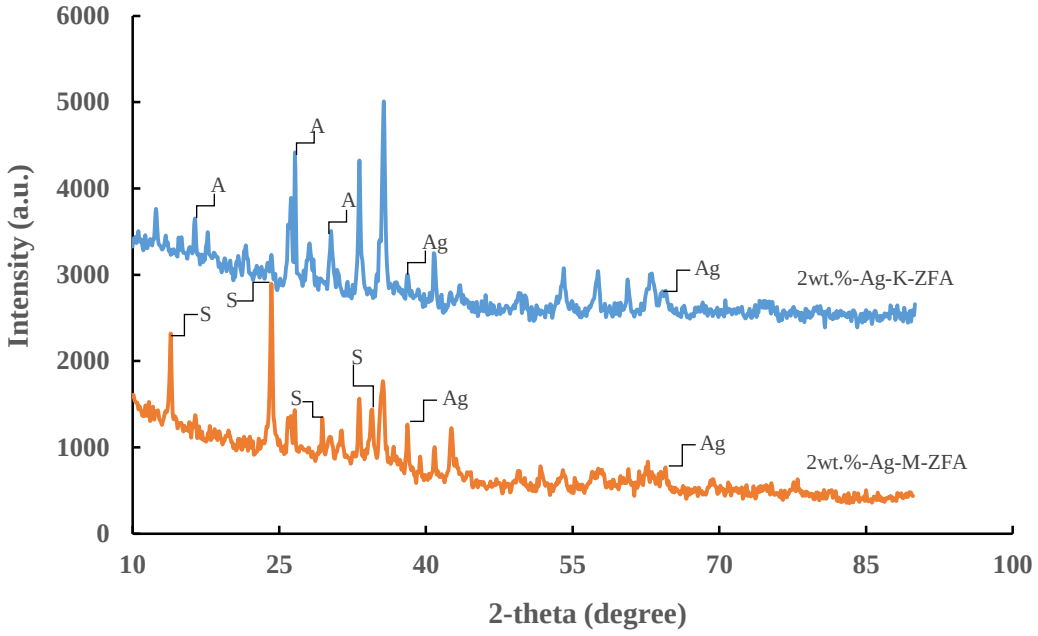

Figure 6.1. The XRD spectrum of pristine nanocomposites (A: analcime; S: sodalite; Ag: silver)

The chemical composition of nanocomposites clearly indicates the aluminosilicate nature of the material as shown in Table 6.2. The total content of silica and aluminum oxides in both nanocomposites is approximately 35 wt.% with a Si/Al ratio varying between 1.25-1.68 and high amount of Fe_2O_3 (40.69-51.92 wt.%), which indicates the bituminous coal nature of CFA type F that in turn might be considered as an advantage since it could facilitate the separation of nanocomposite owing to paramagnetic properties. The results of impregnated Ag NPs (2.25-2.33 wt.%) calculated from XRF analysis are close to the theoretical amount (2.15 wt.%) calculated from the material balance under the assumption provided that the Ag^+ ion exchange and following reduction reactions were fully completed.

Table 6.2. The chemical composition of nanocomposites

Compound [%]	Na_2O	MgO	Al_2O_3	SiO_2	K_2O	CaO	Cr_2O_3	MnO	Fe_2O_3	Ag_2O
2%-Ag-K-ZFA	0.35	0.43	14.63	20.84	0.32	3.72	0.06	0.63	51.92	2.51
2%-Ag-M-ZFA	0.68	0.54	11.85	23.87	0.56	11.07	0.05	0.81	40.69	2.42

The results of BET analysis shows that the surface area of both nanocomposites, namely 2wt.%-Ag-K-ZFA and 2wt.%-Ag-M-ZFA are relatively similar (Table 6.3). The sorption-desorption and pore size distribution (Figures 14 and 15) indicate that both nanocomposites predominantly possess a mesoporous structure.

Table 6.3. The BET analysis of pristine nanocomposites

Material type	BET surface area, m^2/g	Average pore size, nm	Total pore volume, cm^3/g
2wt.%-Ag-K-ZFA	34 ± 2.7	15 ± 3.9	0.22 ± 0.07
2wt.%-Ag-M-ZFA	51 ± 5.6	10 ± 0.1	0.13 ± 0.05

The zeolitic phase formation and Ag NPs impregnation were also observed under the SEM analysis. The corresponding micrograph of a representative sample of nanocomposite 2wt.%-Ag-K-ZFA shown in Figure 6.2 indicate the growth of crystalline zeolites on the surface of CFA particles with impregnated Ag NPs that was quantitatively confirmed with SEM-EDS analysis. The particle size analysis revealed that 2wt.%-Ag-K-ZFA and 2wt.%-Ag-M-ZFA have an average size of 9.53±4.02 μm and 20.43±0.04 μm, respectively, which is in corroboration with SEM analysis.

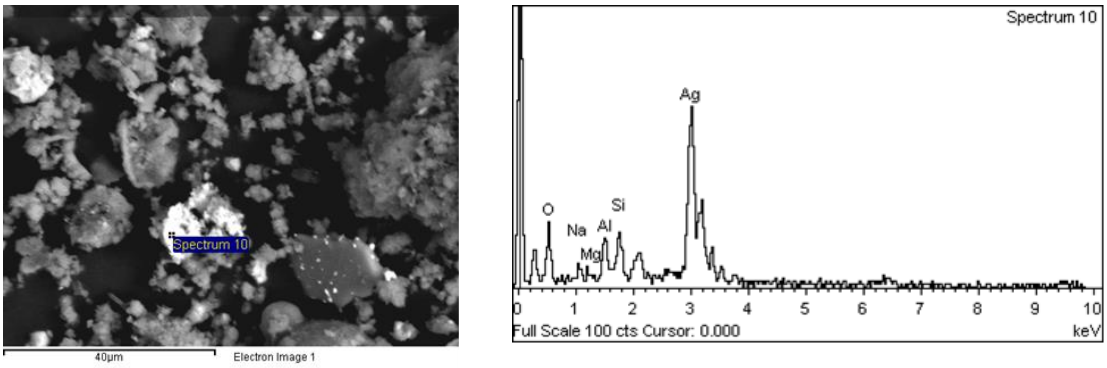

Figure 6.2. The SEM of zeolite crystal growth and EDS analysis of 2wt.%-Ag-K-ZFA

The metallic Ag NPs formation and homogeneous distribution on nanocomposites matrix previously detected on XRD and quantified on XRF was additionally corroborated by TEM imaging. Figure 6.3 demonstrates the TEM analysis of 2wt.%-Ag-M-ZFA and 2wt.%-Ag-K-ZFA nanocomposites with Ag NPs evenly spread on the matrix of nanocomposites.

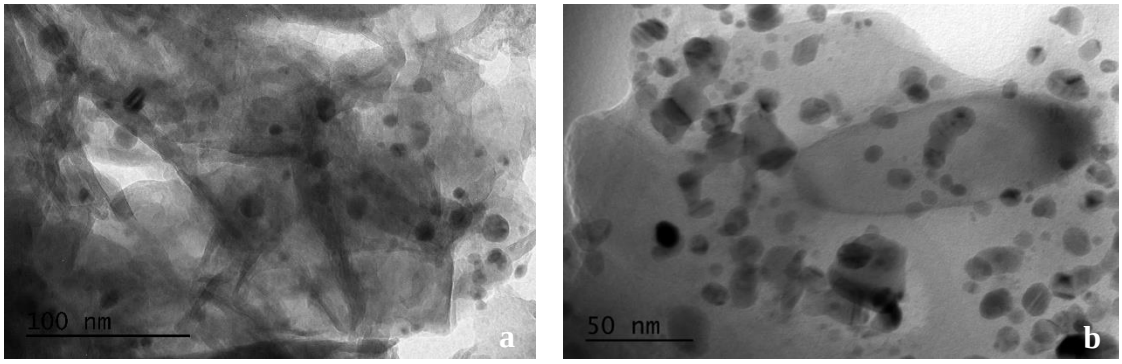

Figure 6.3. The TEM analysis of 2wt.%-Ag-M-ZFA (a) and 2wt.%-Ag-K-ZFA (b)

According to obtained micrographs, the metallic silver is evenly dispersed in the nanocomposite matrix with a relatively low degree of agglomeration of particles and the particle size ranging from 4 to 45 nm. It is obvious from TEM images that in most cases the particle geometry corresponds to a well-defined spherical shape with an average size of 15 nm. The TEM-EDS analysis also confirms the presence of Ag NPs in nanocomposites 2wt.%-Ag-K-ZFA and 2wt.%-Ag-K-ZFA as shown in Figure 6.4.

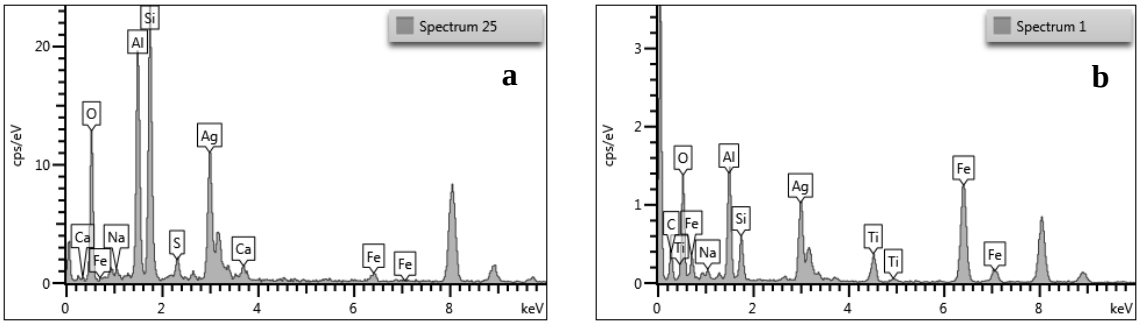

Figure 6.4. The TEM-EDS analysis of 2wt.%-Ag-M-ZFA (a) and 2wt.%-Ag-K-ZFA (b)

6.4. Adsorption kinetics and equilibrium isotherms

It is important to emphasize that both a radioactive and non-radioactive iodine could easily be transformed into species of iodide, iodate, and triiodide in water solutions [222] a fact that is overlooked in literature. This is especially important because the traditional method for I^- measurement is UV-Vis, and if a redox reaction takes place then the decrease of I^- concentration can be mistakenly considered as removal due to adsorption. In Figure 6.5 the Pourbaix diagram of iodine species is given. Taking into account that laboratory pure water

has a redox potential of 0.25-0.5 V, I^- solutions are stable unless pH is higher than ~10 or an oxidizing agent is added to the solution under acidic conditions.

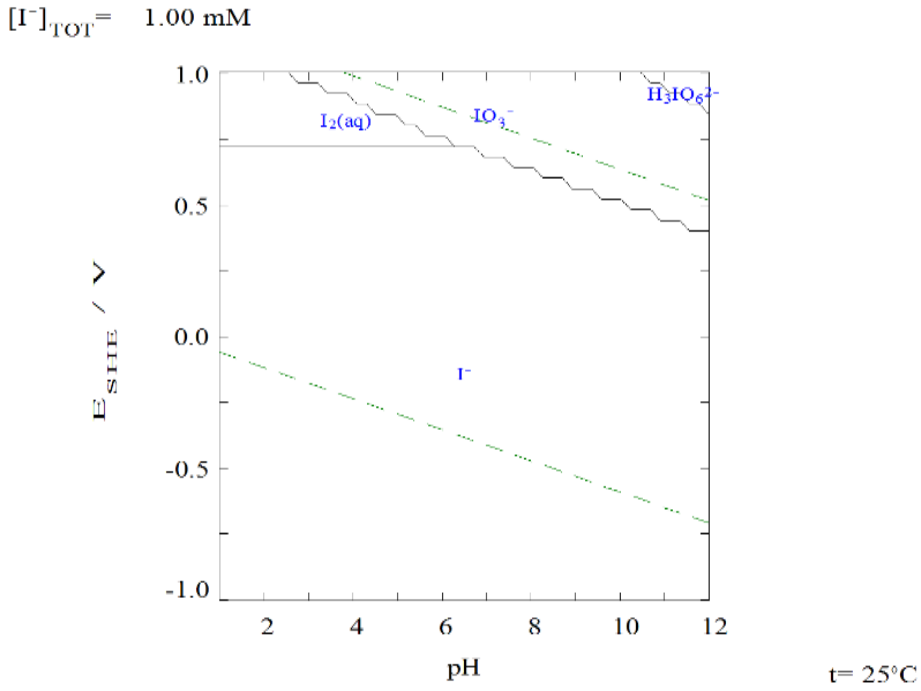

Figure 6.5. The speciation diagram generated by Medusa software

Comprehensive research conducted by Kireev and Shnyrev [120] on speciation was conducted employing UV-Vis spectroscopy for identification of iodine species. Similarly, other research groups applied the UV-Vis to measure the I^- concentration in removal studies [34,117,118,122]. The transformation of species might follow a single or combination of these reactions depending on environmental conditions [120]:

$$I_2 + H_2O \rightarrow HIO + H^+ + I^- \quad (6.1)$$

$$3HIO \rightarrow 3H^+ + IO_3^- + 2I^- \quad (6.2)$$

$$I_2 + I^- \leftrightarrow I_3^- \quad (6.3)$$

$$HIO_3 \rightarrow H + IO_3^- \quad (6.4)$$

According to Kireev and Shnyrev [120] IO_3^- shows no peaks and the intensity is gradually decreasing from 180 nm onwards, I_2 shows a peak at 203 nm, I^- at 226 nm while I_3^- shows two peaks at 288 and 352 nm. It should be noted that I_3^- is formed in the solution provided that I^- and I_2 are mixed to form it. During the experiments we have scanned the UV-Vis range

from 180 to 400 nm and no other than I^- peak was observed, which is in agreement with the Purbaix diagram (Figure 6.5).

The surface charge of the solid affects the interaction between the surface and species existing in the solution provided that they have opposite charges. The measurements of the zeta potential of nanocomposites at different pH provide information on the surface charge and the point of zero charge (pH_{ZPC}), where the net surface charge becomes zero. The results obtained for both nanocomposites reveal that the surface of materials is positively charged from pH 2.0 to 4.5 and negatively charged from pH 4.5 to 12 (Figure 6.6). The pH of the solutions during I^- removal was increased from 2.5 to 6 and thus the electrostatic attraction of I^- is favored, at least for some part of the process. Although in the absence of silver on the surface of materials the I^- adsorption was found to be negligible, thus the attraction of I^- ions on the surface should have a minor effect accelerating the reaction in the presence of silver.

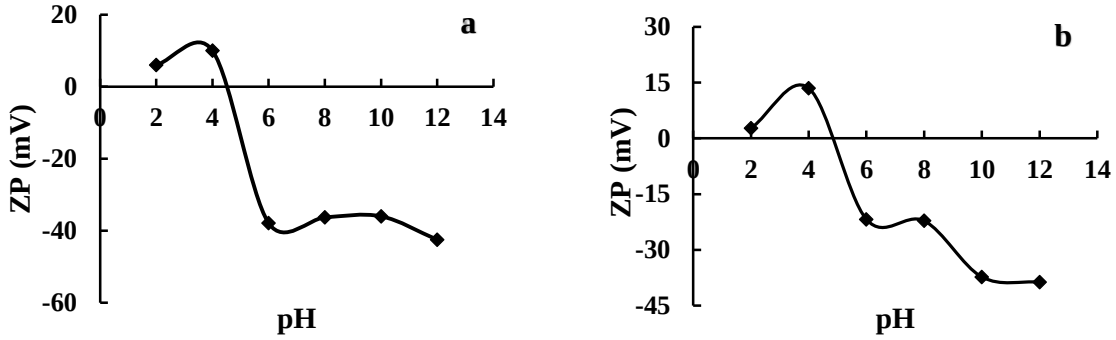

Figure 6.6. The surface charge of nanocomposites at different pH values: 2wt.%-Ag-K-ZFA (a) and 2wt.%-Ag-M-ZFA (b)

The adsorption kinetics results presented in Figure 6.7 show that adsorption curves of both nanocomposites and both concentrations reached a plateau, which indicates equilibrium or saturation. The semi-logarithmic curves of the adsorption kinetics provide more details on how the adsorption underwent at the initial hours of the experiment (see Figure D1). It is clear from the logarithmic curves that the rate of adsorption over time is faster in 2wt.%-Ag-K-ZFA for all concentrations under study, which might be explained by the diverse microstructure of nanocomposites that entails different diffusion rates of I^- species. The nanocomposites adsorbed half of the initial concentration within 10 hours and gradually reached the average maximum removal values of 93%, 57% and 35% for 75 ppm, 150 ppm,

and 250 ppm I^- solutions, respectively. The fast removal in the first hours is attributed to the fast reaction with Ag located in the outer part of the material while the slow diffusion to the interior caused the removal to slow down. It should be noted that although the kinetics of nanocomposites were diverse at the initial hours, both of them reached the plateau after approximately the same duration with a comparable adsorption capacity.

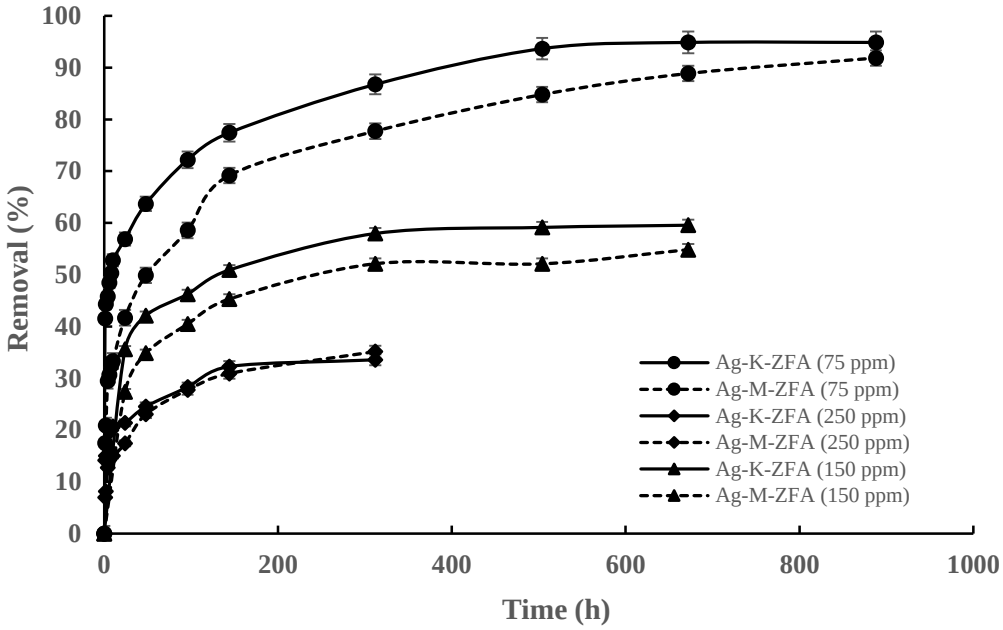

Figure 6.7. The adsorption kinetics of I^- using nanocomposites

The relatively slow adsorption kinetics might be explained by the removal mechanism of I^-, which undergoes first oxidation of Ag NPs to Ag_2O, then diffusion in the pore structure of the material and finally a chemical reaction between the I^- and oxidized silver [130,232]:

$$4Ag^o + O_2 \rightarrow 2Ag_2O \quad (6.5)$$

$$Ag_2O + 2H^+ \rightarrow 2Ag^+ + H_2O \quad (6.6)$$

$$Ag^+ + I^- \rightarrow AgI\ (\downarrow) \quad (6.7)$$

As the reaction proceeds, a layer of AgI and below a layer of Ag_2O are formed through which the oxygen and iodide have to diffuse in order the reaction to proceed. The mechanism was described by Krausman and Drossinos [233] who used bulk silver to perform the reaction with I^- and I_2 from solutions. Also, they argued that the AgI layer is non-porous as the molar volume of the halide is bigger than the silver metal. This means that the size of Ag NPs influence the overall removal rate.

The degree and rate of silver oxidation plays a decisive role. It is well-known that the interaction of metallic silver with iodide in water can happen only under oxidizing conditions [232,233]. Besides the dissolved oxygen, the pH of the solution plays a crucial role and many authors have observed that oxidation gradually disappears as the solution pH increases above 7.0 [130,233]. As Liu and Hurt [232] experimentally demonstrated the dissolution reaction (6.6) in air-saturated water is mediated by peroxide intermediates:

$$O_2 + H^+ \xrightarrow{Ag^o} Ag^+ + H_2O_2 \text{ intermediates} \xrightarrow{Ag^o} Ag^+ + H_2O \quad (6.8)$$

Thus, it is likely that the oxidation is hindering by elevated OH^- concentrations which act as scavengers of the H_2O_2 intermediates.

Liu and Hurt [232] examined the oxidation of free Ag^o nanoparticles of average size of 1.9 nm to Ag_2O and the dissolution of the latter to Ag^+ which takes place in the presence of dissolved oxygen and mild acidic conditions (pH > 4). Actually, the process results in complete disappearance of the nanoparticles at pH 5.68 which becomes dissolved Ag^+, although the process is relatively slow (6-125 days). Complete dissolution was not observed in other works, as for example the work conducted by Peretyazhko *et al.* [234] who found that after 26 days the systems reach equilibrium. The extend of dissolution at pH 6-8 was 14.9%, 5.5% and 3.2% and negligible for Ag NPs of size of 6, 9, 13 and 70 nm, respectively. In acetic acid solutions at pH 3.0 the dissolution was larger at 41%, 20.7%, 13.5% and 6.5%, respectively. The kinetics of Ag^+ release due to dissolved O_2 in water is poorly understood. In general, the smaller free Ag NPs release more Ag^+ than larger ones [234]. For more details see the work of Molleman and Hiemstra [235].

Surprisingly, the Ag^+ release from fixed nanoparticles on substrates due to dissolved O_2 in water is not thoroughly discussed in the related literature. In fact, in many publications the dissolution reaction (6.6) is not mentioned and it is assumed that I^- reacts with Ag_2O [118,119,227]. An exception is the work of Hoskins *et al*. [130] who experimentally proved that Ag^+ is released from metallic silver impregnated in activated carbon following oxidation to Ag_2O in the presence of oxygen in acidic solutions. The leaching experiments on the 2wt.%-Ag-K-ZFA and 2wt.%-Ag-M-ZFA samples at pH 2.5 showed that after 12 days less than 0.17% of silver is leached back to the aqueous phase resulting in a solution concentration between 0.06-0.11 ppm. This result is in agreement with Polo *et al*. [229] who

mention the absence of silver leaching during oxidation of Ag^o to Ag^+ even by use of strong oxidants such as H_2O_2. Polo *et al*. provides the following mechanism:

$$Ag^o + H_2O_2 \rightarrow \text{intermediate } H_2O_2 \rightarrow Ag^o\text{-}Ag+ + O_2^{\cdot -} + 2H_2O \quad (6.9)$$

The Ag^o-Ag^+ and Ago-cloth-Ag^+ complexes are used to highlight the absence of Ag^+ leaching from the material, a polymeric-based cloth. The low degree of leaching observed in our experiments can be attributed to the relatively large NPs (up to 45 nm) and the properties of the zeolitic surface, i.e. chemistry, surface area and porous structure. Another possibility is the adsorption of Ag^+ on the NPs surface [234]. The release of Ag^+ from fixed NPs on substrates is something that requires further investigation and is beyond the scope of this paper. In our experiments silver loss to the solution can also happen due to ion exchange with K^+ but this is unlikely as excess reducer was used and all Ag^+ ions that should have been converted to Ag NPs. Leached Ag^+ would have resulted in the formation of a visible cloud in the solution and, in the case of colloids formation, a peak at about 424 nm, both of which were not observed during the experiments. The fact is that reaction (6.7) takes place and thus the Ag^+ formation is beyond doubt, regardless the presence of I^-. The Ag NPs and the produced AgI are firmly fixed on the surface of the material as all characterizations demonstrate (XRD, XRF, SEM-EDS, TEM-EDS). The absence of Ag^+ release into the solution can only be explained if it is adsorbed either on the NPs as Ag^o-Ag^+, the outer surface of the formed Ag_2O layer or in other sites in the zeolite structure.

The adsorption isotherms of I^- further confirm the proposed mechanism showing that adsorption reaches the equilibrium value when all existing I^- is reacted with Ag NPs, i.e. the overall process is irreversible resulting in a rectangular isotherm as shown in Figure 6.8. Also, according to reaction (6.6) the pH of the solution increases, as indeed happened, from 2.5 to about 6.0. A rectangular isotherm indicates the absence of physical adsorption and gives the capacity expected from the Ag content of the material, as for example was observed in the removal of I^- by Ag_2O grafted titanate nanolamina [118]. Based on the theoretical Ag content of the materials (2.15%) the capacity of the materials in terms of I^- is 25.28 mg/g while the average measured capacities are 19.33±0.76 mg/g and 18.60±0.74 mg/g for the 2wt.%-Ag-K-ZFA and 2wt.%-Ag-M-ZFA, respectively. This means that the 73.6-76.5% of the capacity is utilized indicating that some Ag NPs are located in locations not accessible to I^-, probably due to the partial blockage of the pores of the materials during the reaction.

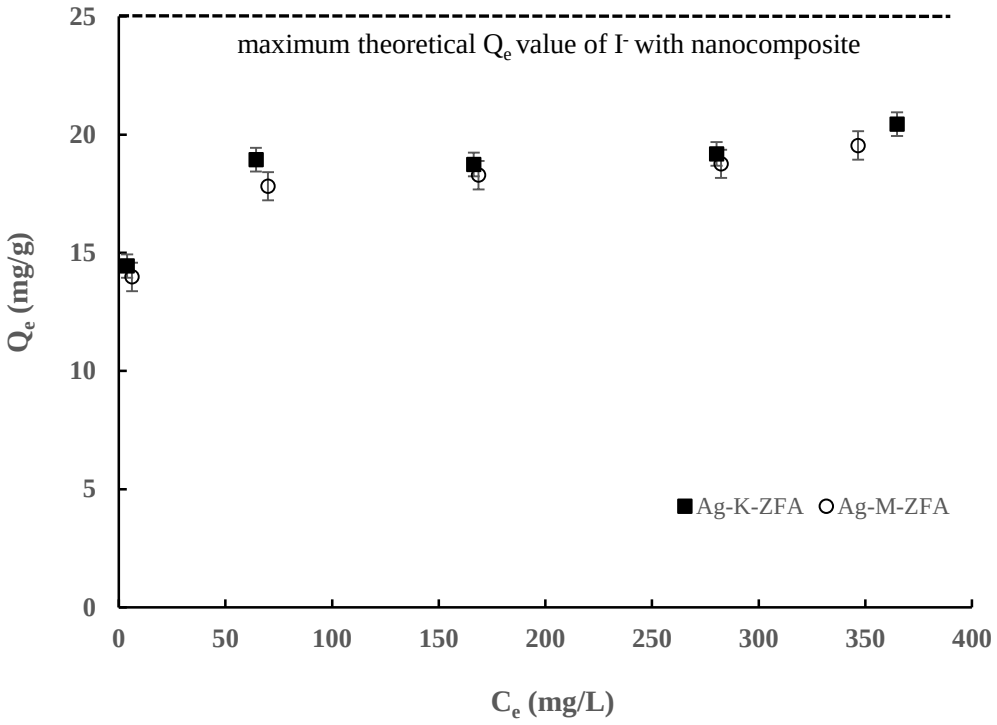

Figure 6.8. The adsorption isotherms of I^- using nanocomposites

6.5. Adsorption mechanism studies

The formation of AgI precipitate on the surface of the material is additionally confirmed by XRD analysis that shows the phase content in the mineral. The corresponding indicative peaks of Ag NPs present in nanocomposites (38.18º, 44.33º and 64.52º) has disappeared or significantly decreased in intensity, while the formation of AgI could be observed by the corresponding peaks at 22.32º, 23.71º, 39.20º, 42.63º and 46.30º, indicating that the reaction between the iodide and silver formed the precipitate as presented in Figure 6.9. It should be noted that the I^- uptake is slightly lower than the doped amount of Ag NPs, which explains the existence of low-intensity peaks of silver in iodide-adsorbed nanocomposites.

The adsorbed amount of I^- on the samples treated with the 350 ppm and 450 ppm initial I^- concentrations is quantified using XRF analysis (Table 6.4). According to results obtained, the nanocomposites contained 18-23% less silver than the parent materials while the I:Ag molar rations are 0.77:1 and 1:1 for 2wt.%-Ag-M-ZFA and 2wt.%-Ag-K-ZFA, respectively. Keeping in mind that XRF is a semi-quantitative analysis, the I:Ag ratios are reasonable but there is a question on the lower amounts of Ag detected by XRF.

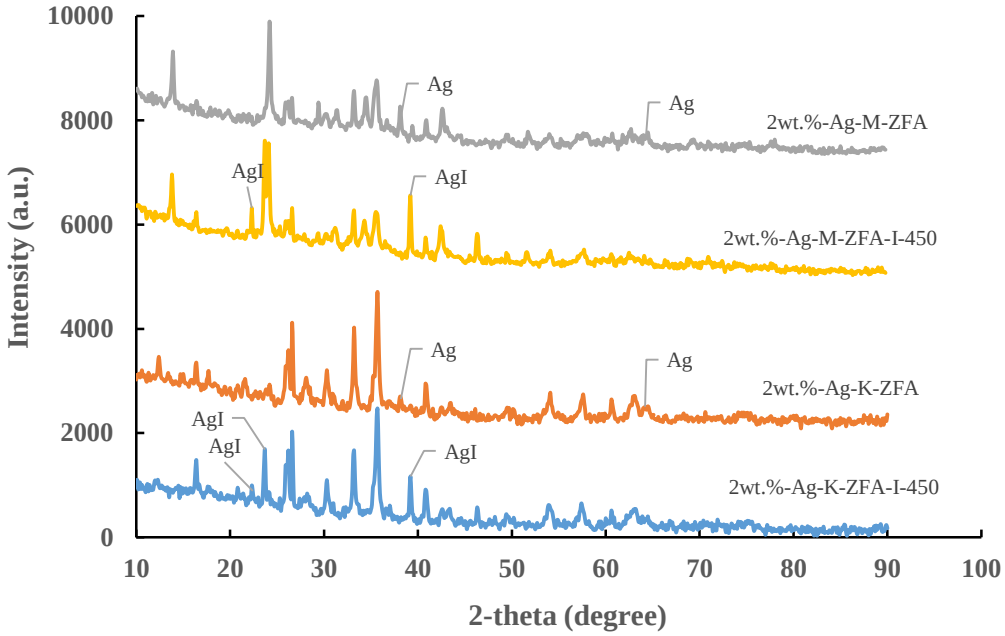

Figure 6.9. XRD spectrum of pristine and I^- adsorbed nanocomposites

However, as discussed above, the release of Ag^+ to the solution is unlikely and even if it takes place the released Ag^+ should be arrested by incoming I^- ions in the porous structure of the zeolites. Thus, the deviations of silver content observed by XRF can be attributed to the semi-quantitative nature of the technique and the conclusion is that Ag NPs and AgI are stable on the surface of the materials. The schematic diagram of I^- adsorption could be depicted as in Figure 6.10.

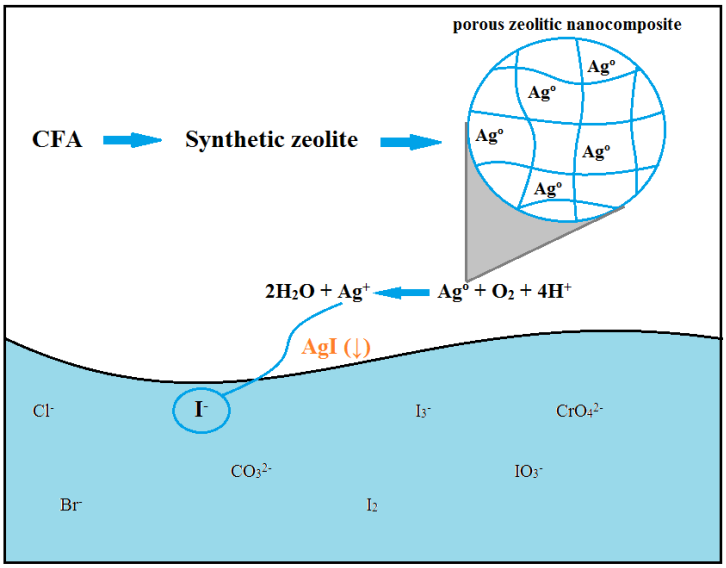

Figure 6.10. Schematic diagram of I^- adsorption from water

Table 6.4. The chemical composition of iodide-adsorbed nanocomposites

Compounds	2%-Ag-K-ZFA-I-350 [%]	2%-Ag-K-ZFA-I-450 [%]	2%-Ag-M-ZFA-I-350 [%]	2%-Ag-M-ZFA-I-450 [%]
Na_2O	0.056	0.046	0.230	0.114
MgO	0.359	0.399	0.574	0.611
Al_2O_3	14.598	13.625	13.103	13.519
SiO_2	20.953	18.720	24.160	24.557
K_2O	1.158	0.667	3.016	1.881
CaO	2.661	1.809	5.655	4.270
Cr_2O_3	0.063	0.058	0.045	0.057
MnO	0.630	0.652	0.876	0.887
Fe_2O_3	51.645	56.125	43.504	46.106
Ag_2O	1.737	1.817	2.005	1.787
I	1.523	1.469	2.076	2.049

The surface morphology of nanocomposites after adsorption of I^- was studied using SEM-EDS analysis. The results of mapping and quantitative analysis further revealed that the elemental silver exists at specific points where the I^- is found and *vice versa*, while the EDS indicated close to 1:1 ratio of Ag and I confirming the AgI precipitate development in both nanocomposites (Figure 6.11-6.13).

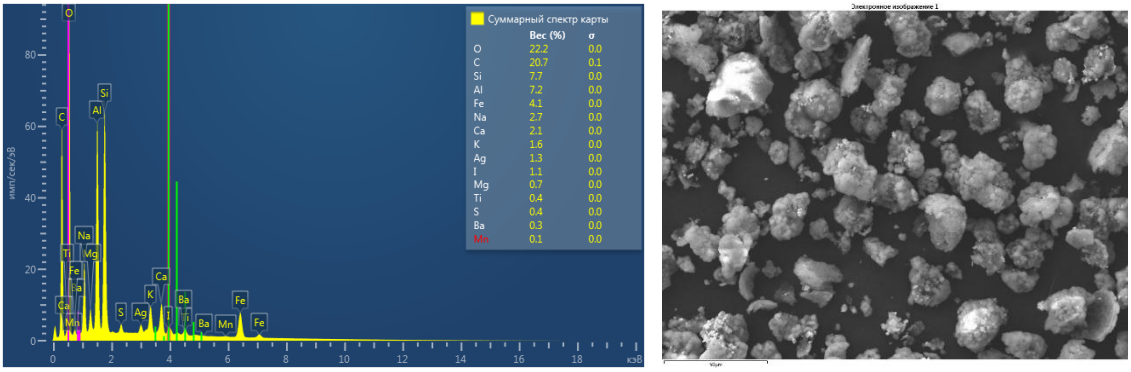

Figure 6.11. SEM-EDS analysis of iodide-adsorbed 2wt.%-Ag-M-ZFA nanocomposite

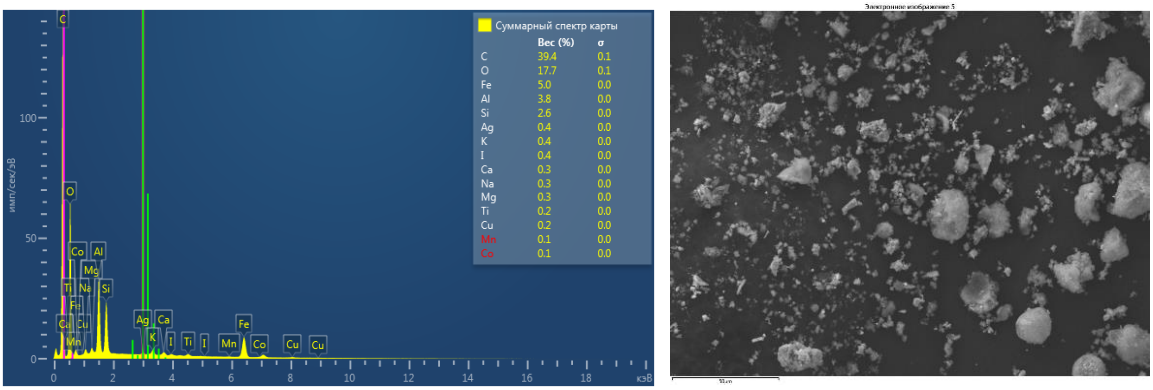

Figure 6.12. SEM-EDS analysis of iodide-adsorbed 2wt.%-Ag-K-ZFA nanocomposite

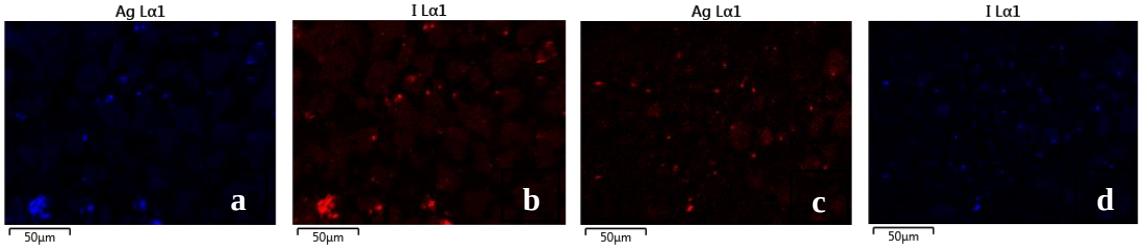

Figure 6.13. SEM mapping of 2wt.%-Ag-M-ZFA-I (a, b) and 2wt.%-Ag-K-ZFA-I (c, d)

TEM analysis also corroborated with SEM-EDS analysis and confirmed the formation of AgI precipitate. As shown in Figure 6.14, the initial Ag NPs present in both nanocomposites were transformed into AgI precipitate indicated by the extended dark areas on TEM images. Additional TEM images and SEM-EDS analysis of nanocomposites after I^- adsorption could be found in Figures D2-D3.

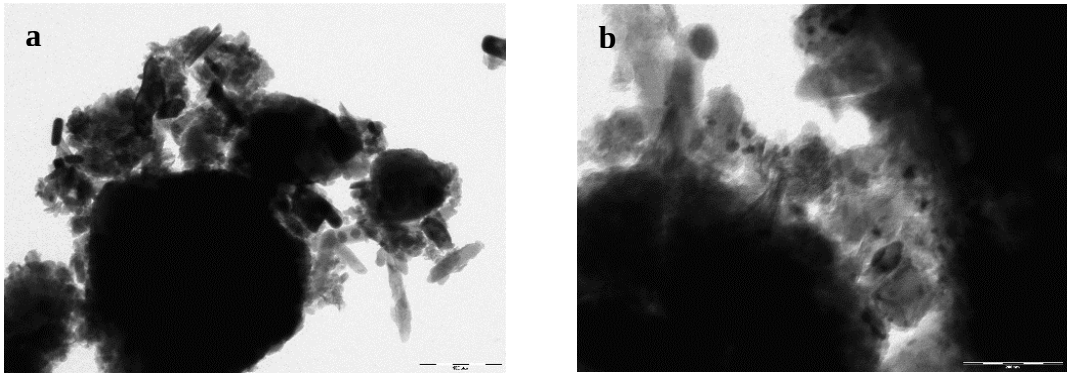

Figure 6.14. TEM of iodide-adsorbed 2wt.%-Ag-K-ZFA (a) and 2wt.%-Ag-M-ZFA (b)

The BET surface area analysis showed the slight increase of initial surface area from 34±2.7 to 37±2.8 m^2/g and 51±5.6 to 57±4.1 m^2/g for 2wt.%-Ag-K-ZFA and 2wt.%-Ag-M-ZFA, respectively. This, in turn, could be explained due to fine new formations of AgI precipitate particles within the structure of the materials or unblocking effect of pores by Ag NPs owing to reaction of Ag NPs with I^- to form AgI precipitates. The adsorption-desorption curves of both materials with 450 ppm I^- indicate the Type II hysteresis as shown in Figure 6.15, which is characteristic for macro-porous and mesoporous adsorbents as nanocomposites used in this study.

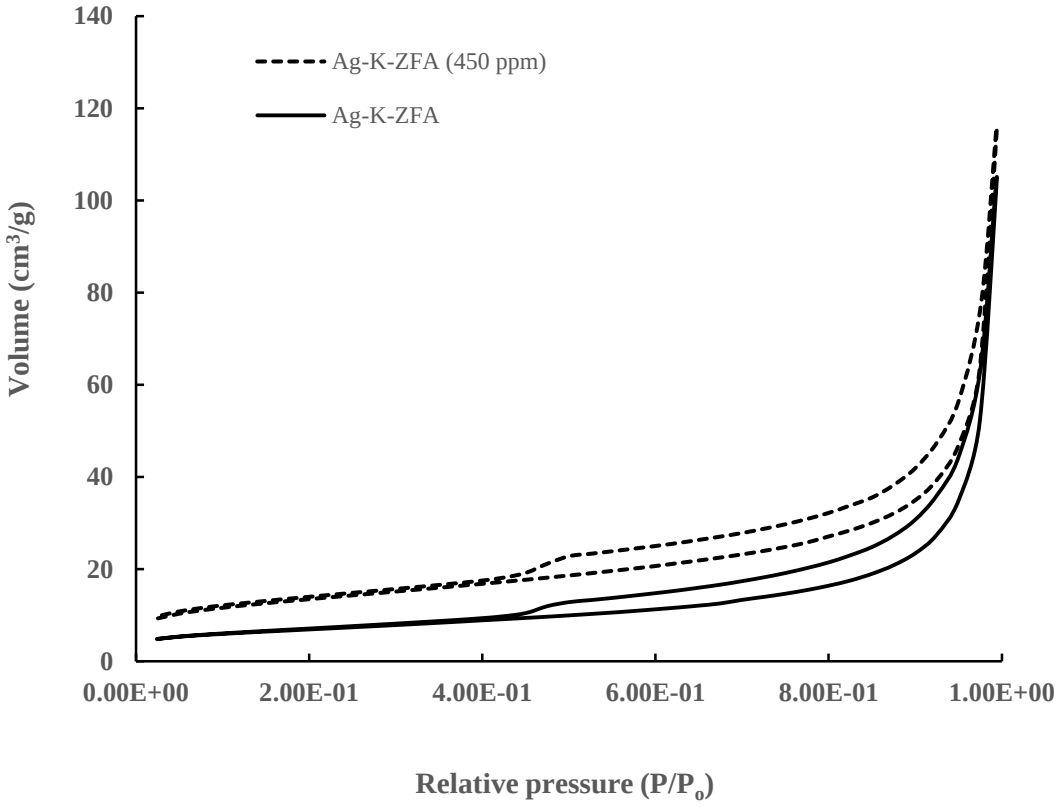

Figure 6.15. Adsorption-desorption of 2wt.%-Ag-K-ZFA and 2wt.%-Ag-K-ZFA-I-450

The formation of distinctive hysteresis on both isotherms validates that adsorbents contain mesopores with the size of 2-50 nm that is in agreement with pore size distribution analysis shown in Figure 6.16. The pore size distribution calculated by the BJH method for both pristine and iodide-containing nanocomposites shows that the major fractions of pores have the same size of 3.72 nm. These results demonstrate that no significant structural changes occur during the adsorption experiments under strongly acidic conditions and the minor

increase of BET surface area of iodide-adsorbed nanocomposites could be due to the synergetic effect of precipitated particles on the surface and within the mesoporous structure of nanocomposites.

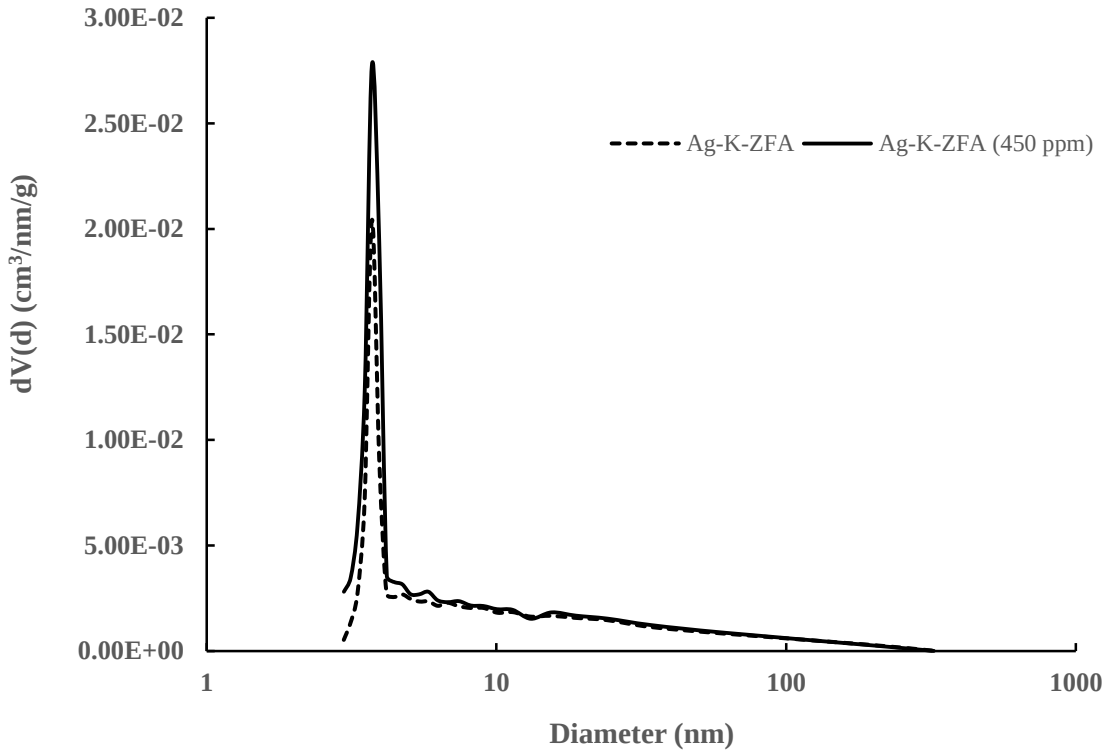

Figure 6.16. Pore size distribution of 2wt.%-Ag-K-ZFA and 2wt.%-Ag-K-ZFA-I-450

6.6. Adsorption kinetics modeling

The quality of the diffusion-based model is good with an average error of 6.88±4.98% (Figure 6.17), strongly indicating that the controlling mechanism is slow intra-particle surface diffusion with diffusion coefficients in the range of 0.37-1.72×10^{-13} cm^2/s.

In Table 6.5 the published values of surface diffusion coefficients in liquid phase adsorption on analcime and sodalite are summarized. Similar values have been reported by Dyer *et al*. for the diffusion of heavy metals in anaclime [236]. Nevertheless, the estimated diffusion coefficients are much lower than those reported for other zeolites [237] and this can be attributed to the internal precipitation of AgI, which partly blocks the pores and inhibits the diffusion of I^- towards other active sites, as discussed in the analysis of the isotherm.

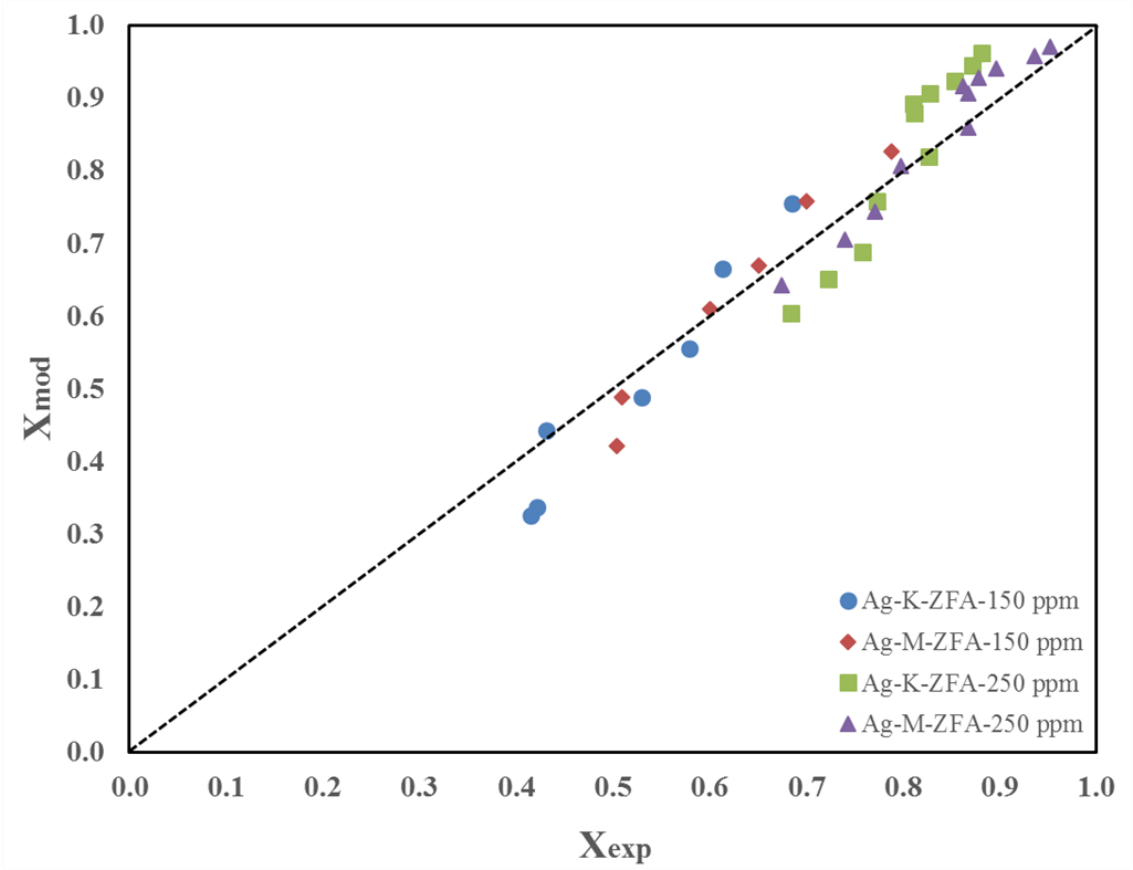

Figure 6.17. The adsorption kinetics modeling vs. experimental values

Table 6.5. Diffusion coefficients on sodalite and analcime

Type of the zeolite	Type of adsorbed species	Temperature [°C]	Diffusion coefficient [cm^2/s]	Reference
Synthetic analcime	Cu^{2+}, Ni^{2+}, Pb^{2+}, Zn^{2+}	25-60	10^{-13}	[236]
Synthetic sodalite	Cs^{+}	80	10^{-10}	[238]
Natural sodalite	Na^{+}	580	8.7×10^{-11}	[239]
Natural analcime	Na^{+}	357	2.3×10^{-9}	[239]

6.7. Effect of the competing and co-existing anions

The supplementary experiments were conducted to examine the effect of competing Cl- (1000 ppm) anion with excess concentration than that of starting concentration of I- (300 ppm). In addition, the effect of selective adsorption of I- in the presence of co-existing anions was studied with the same initial concentrations as of I-, which also potentially could form the precipitates with Ag NPs. As shown in Figure 6.18, the I^- equilibrium uptake is not significantly hindered by any of studied co-existing anions under the same initial concentration of 300 ppm. The removal kinetics of I^- was slightly slower at the starting points for CO_3^{2-}, however, it has closely reached the maximum theoretical adsorption capacity as for I^-, I^- with Cl^-, Br^- and CrO_4^{2-}. In addition, it was observed that the I^- concentration in control solutions with co-existence of CrO_4^{2-} anion was significantly reduced by time. This is explained by the redox reaction of Cr^{6+}/Cr^{3+}, which in turn oxidized the I^-/I_2, while the other co-existing and competing anions have not noticeably affected the control solutions.

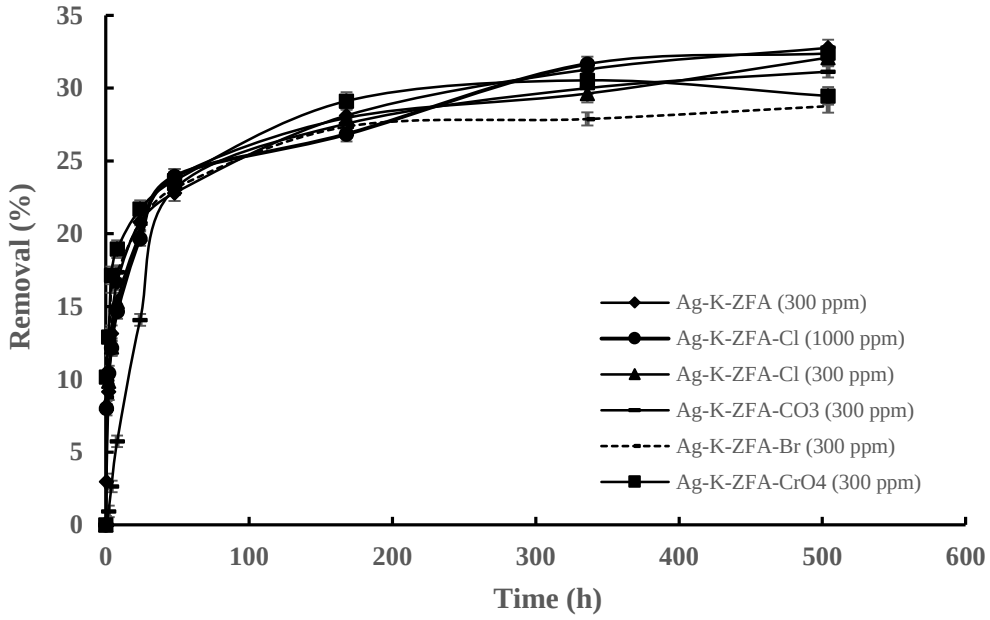

Figure 6.18. The competitive and co-existing anions effect on I^- removal

The semi-logarithmic curves of kinetics clearly show the effect of CO_3^{2-} resulting in slow adsorption until 64 hours after which it reaches the removal levels of the other anions (see Figure D4). The strongly negative effect of CO_3^{2-} has been attributed by Zhang *et al*. [195] to its high negative charge density which facilitates the adsorption on positively charged surfaces. The pH of the solutions increased from 2.5 to 6.0, and according to Figure 6 the

surface is positive at the beginning of the removal and thus it explains the negative effect of CO_3^{2-} up to 64 hours. This effect diminishes in the course of the process as the pH increases and the surface of the nanocomposites becomes negatively charged.

The competing Cl^- anion with more than three-fold excess concentration than of I-, has not affected the removal performance of nanocomposite. This is explained by the lower Gibbs energy of the reaction (-32 kJ/mole) between the I^- and Ag_2O along with affinity to the surface of material and relatively small radius of anion [118,191], than that of other competing anions Cl^-, CO_3^{2-}, Br^- and CrO_4^{2-}. The highly selective adsorption of I^- in the presence of other anions is due to solubility differences between AgI and other precipitates of competing anions. In both scenarios, the kinetically favorable reaction undergoes first and that is the precipitation of AgI. Thus, the obtained results indicate that the Ag NPs shows high selectivity primarily towards I^- in solution and form the precipitates until all available I^- is reacted, after which other existing anions form their precipitates with remaining Ag NPs. Similar trends were observed by other researchers elsewhere [34,117,119].

6.8. Leaching studies

In order to evaluate the stability of adsorbed I^- on the nanocomposite matrix, it is valuable to examine the leaching or desorption behavior of entrapped species. The leaching studies of I^- adsorbed within both nanocomposites 2wt.%-Ag-K-ZFA and 2wt.%-Ag-M-ZFA were conducted by using two different concentrations under strong acidic and neutral phases as presented in Table 6.6.

Table 6.6. Leaching studies of I^- using 2wt.%-Ag-K-ZFA and 2wt.%-Ag-M-ZFA

Adsorbent and initial I^- concentration	pH used for leaching studies	Total adsorbed I^- [mg]	Leached amount [mg]	Leached amount [%]
2wt.%-Ag-K-ZFA-I-350	2.0	3.84	0.054	1.42
	7.0		0.004	0.11
2wt.%-Ag-K-ZFA-I-450	2.0	4.18	0.055	1.33
	7.0		0.005	0.12
2wt.%-Ag-M-ZFA-I-350	2.0	3.75	0.024	0.64
	7.0		0.004	0.11
2wt.%-Ag-M-ZFA-I-450	2.0	3.91	0.040	1.03
	7.0		0.005	0.14

The results revealed that AgI is stable on the nanocomposite under the conditions of neutral and acidic environment for 12 consecutive days of experiments. The leached amount of I^- under strong acidic phase conditions varies between 0.64-1.42% for both nanocomposites, which is considerably low compared to results obtained under neutral and basic conditions elsewhere [34]. In general, the nanocomposites demonstrated a high stability under both sets of experimental conditions, which further expands the possibility of application of the material in remediation of I^- species from water.

6.9. Summary of the chapter

In this chapter, CFA-derived novel nanocomposites with impregnated Ag NPs were used to remove I^- from aqueous solutions. The results revealed a high removal efficiency (up to 94.85%) and stability of adsorbed species within the microstructure of nanocomposite. The maximum achieved adsorption capacity of the nanocomposites was between 19.54-20.44 mg/g. The removal mechanisms of I^- were meticulously studied by employing multiple characterization techniques, such as XRD, XRF, SEM-EDS, TEM, and BET analysis. The qualitative and quantitative examination of pre- and post-adsorption samples of nanocomposite proved the formation and development of AgI *via* oxidation of initial Ag NPs followed by the reaction with I^- to form a stable crystalline precipitate on the surface of the materials. The diffusion-based model indicated that the controlling mechanism is a slow intra-particle surface diffusion with diffusion coefficients in the range of $0.37\text{-}1.72\times10^{-13}$ cm^2/s. The investigation of competing and co-existing anions (Cl^-, Br^-, CO_3^{2-}, and CrO_4^{2-}) on the removal efficiency of I^- demonstrated a negligible effect showing the kinetically favorable reaction of I^- precipitation over other halides and oxygen containing anions.

CHAPTER 7

CONCLUSIONS AND FUTURE WORK

The water resources contamination with various toxic and hazardous organic and inorganic pollutants is one of the severe issues that needs to be tackled through cost-effective and easy-to-processing methods. During the last decade, the interest of research world among these hazardous contaminants laid on toxic Hg^{2+} and radioactive I^- due to the devastating effects that create many problems to the environment. The abundant by-product of coal combustion power plants in the form of CFA, which is accumulated during the electricity and power generation in many developed and developing countries, could be efficiently utilized for production of synthetic zeolites and nanocomposites with Ag NPs for removal of Hg^{2+} and I^-, which strongly binds with these ions to form amalgam and precipitates that possess stability and non-hazardousness required for optimal utilization. However, these requires a considerate understanding of the production and optimization methods of synthetic zeolites derived from CFA and corresponding Ag NPs-doped nanocomposites.

7.1. Conclusions

The work presented in Chapter 4 under this research contributes experimental results on the production of ZFA from CFA under different reaction conditions, such as the reaction time, reaction temperature, alkali solution concentration, Si/Al and L/S ratio. According to findings, depending on reaction parameters, an average conversion of CFA into ZFA, both in the literature and experiments of this work, ranges from ~20 to ~80%. The experimental results and literature data were farther studied employing the heuristic method in order to optimize the system identification of conversion. According to results, the optimized fuzzy models illustrate a close similarity with an average divergence of 5%, both with empirical results and literature values. These allow assuming the probability of application of the heuristic method with fuzzy models in the production of ZFAs from CFAs, which enables to predict the influence of reaction parameters and guide on the probable development mechanism of synthetic zeolite.

The obtained ZFAs were further doped with Ag NPs to produce nanocomposites via alkaline hydrothermal treatment followed by ion-exchange and reduction of Ag^+ ions in Chapter 5.

The novel nanocomposites with doped Ag NPs (up to 50 nm), its parent CFA and ZFA were efficaciously applied for Hg^{2+} uptake from water solutions. The adsorption kinetics of Hg^{2+} on the CFA-derived ZFA, a novel Ag NPs containing nanocomposite, and respective reduced materials has shown that nanocomposites demonstrate a strong and fast adsorption compared with parent ZFAs and CFAs. The advanced characterization on XRD, TEM/EDS and mapping of post-adsorption materials has revealed that the controlling mechanisms of Hg^{2+} uptake in ZFAs is a physical adsorption, wherein the novel nanocomposites overcome a reduction and oxidation reaction by producing Hg° and amalgam of two metals Ag_xHg_y. The leaching studies of adsorbed Hg^{2+} ions in nanocomposite indicated a strong stability under neutral and acidic conditions (on average 0.82%), which further adds the advantage for the novel material. Thus, the produced novel nanocomposite revealed a superior adsorption capacity, adsorption rate and significantly less leaching of adsorbed and amalgamated mercury. Furthermore, the Ag NPs doped novel nanocomposites were investigated for removal of I^- from water solutions in Chapter 6. The results showed an enhanced removal potential of I^- up to 94.85% with saturation capacities of 19.54-20.44 mg/g. The detailed studies of removal mechanism indicated that I^- is removed from water by a step-wise oxidation of Ag NPs followed by diffusion into the porous structure and a precipitation reaction, which was confirmed by multiple advanced characterizations methods, such as XRD, XRF, SEM-EDS and TEM analysis. The investigation of the competing and co-existing anions on I^- removal showed insignificant effect on the performance of nanocomposite with an average adsorption capacity of 19.76 mg/g, which is similar to pure I^- removal experiments. The leaching studies further demonstrated the high stability of adsorbed and precipitated iodide in the form of AgI in nanocomposite matrix in both strong acidic and neutral conditions.

The study on the application of the developed nanocomposites to the environmental systems could be investigated in order to evaluate the different reactor systems and optimize the collection and recycle of used nanocomposites for the economical operations. The nanocomposites could be tested in fixed-bed reactors by varying the operating parameters, such as the size of the granules produced from nanocomposites using various binding agents, the input concentrations and flow-rates of the solutions, etc. As for the collection and recycle of the used nanocomposite, an elevated thermal treatment could be an option to consider. Magnetic properties can be useful to separate the particles from solutions in batch mode

reactors. However, additional detailed studies required to be conducted to draw conclusions based on cost-benefit analysis and feasibility studies.

In conclusion, the comprehensive studies carried out in this thesis provide important insights into the ZFA production from CFA facilitated with factorial analysis and optimization, the effective approach of synthesis of Ag NPs doped nanocomposites along with thorough examination of the produced materials for Hg^{2+} and I^- adsorption from water, which confirms that the novel nanocomposite could be a possible alternative material for an efficient removal of toxic Hg^{2+} and radioactive I^- species from aqueous media.

7.2. Future work

The obtained valuable experimental and modeling results allow to propose several possible research directions for future work that could be summarized as follows:

- The developed fuzzy system might be used for envisaging the type of zeolites to be produced from CFA, which could be further studied in future work. This may help the researchers to save time and produce the targeted type of zeolite more efficiently.
- The produced ZFAs and nanocomposites could be further studied to develop granules or tablets with optimal shape, size and mechanical properties to examine them on lab-scale adsorption columns. The parameters of the experiments and material properties could be varied, such as the flow-rate of input contaminated water, the length and diameter of the column, the shape and size of the tablets or granules, the amount and size of the doped Ag NPs within nanocomposite, etc. These will assist to obtain a valuable experimental data on the performance of the ZFAs and nanocomposites under lab-scale conditions.
- Other heavy metals, such as lead and arsenic, could be studied for remediation from water using the developed novel nanocomposites. The optimum experimental boundaries will be selected by employing a speciation studies and literature analysis.
- On the basis of the batch experiments, it could be proposed that the main experimental parameters that affect the adsorption of contaminant species (Hg^{2+} and I^-) are the initial pH of the solution, the amount of Ag NPs within nanocomposite and the initial concentration of solution. In order to optimize the adsorption process the response surface methodology and analysis of variance (ANOVA) could be applied.

APPENDICES

A. Appendices for Chapter 3

Table A1: The 32 rules, which are used in the fuzzy inferencing mechanism

	Inputs					Consequent variables (Rule outputs)
No.	**Conc.**	**Time**	**Temperature**	**L/S**	**Si/Al**	
1	L	L	L	L	L	865172.029089283
2	L	L	L	L	H	-4372720.15116934
3	L	L	L	H	L	-117809.669323069
4	L	L	L	H	H	510856.405511973
5	L	L	H	L	L	-119494.757805391
6	L	L	H	L	H	574073.568239593
7	L	L	H	H	L	15231.0400738391
8	L	L	H	H	H	-64196.2036847660
9	L	H	L	L	L	64706.0270543526
10	L	H	L	L	H	-341811.845277067
11	L	H	L	H	L	4192.48951983944
12	L	H	L	H	H	-8472.62492975665
13	L	H	H	L	L	-2940.70541357534
14	L	H	H	L	H	43662.4004166549
15	L	H	H	H	L	8661.60453404555
16	L	H	H	H	H	-34265.8759590465
17	H	L	L	L	L	-13166.5525997066
18	H	L	L	L	H	-8997.18172360444
19	H	L	L	H	L	489.345010679993
20	H	L	L	H	H	2049.93389690699

21	H	L	H	L	L	-6313.47990530853
22	H	L	H	L	H	193230.833978243
23	H	L	H	H	L	3220.41750048166
24	H	L	H	H	H	-22374.7985863134
25	H	H	L	L	L	12235.9693787333
26	H	H	L	L	H	1252.06804900537
27	H	H	L	H	L	1835.88827844155
28	H	H	L	H	H	-9821.16156796513
29	H	H	H	L	L	-30171.5306545123
30	H	H	H	L	H	8724.09071150934
31	H	H	H	H	L	4004.20084894336
32	H	H	H	H	H	-6834.36073106111

B. Appendices for Chapter 4

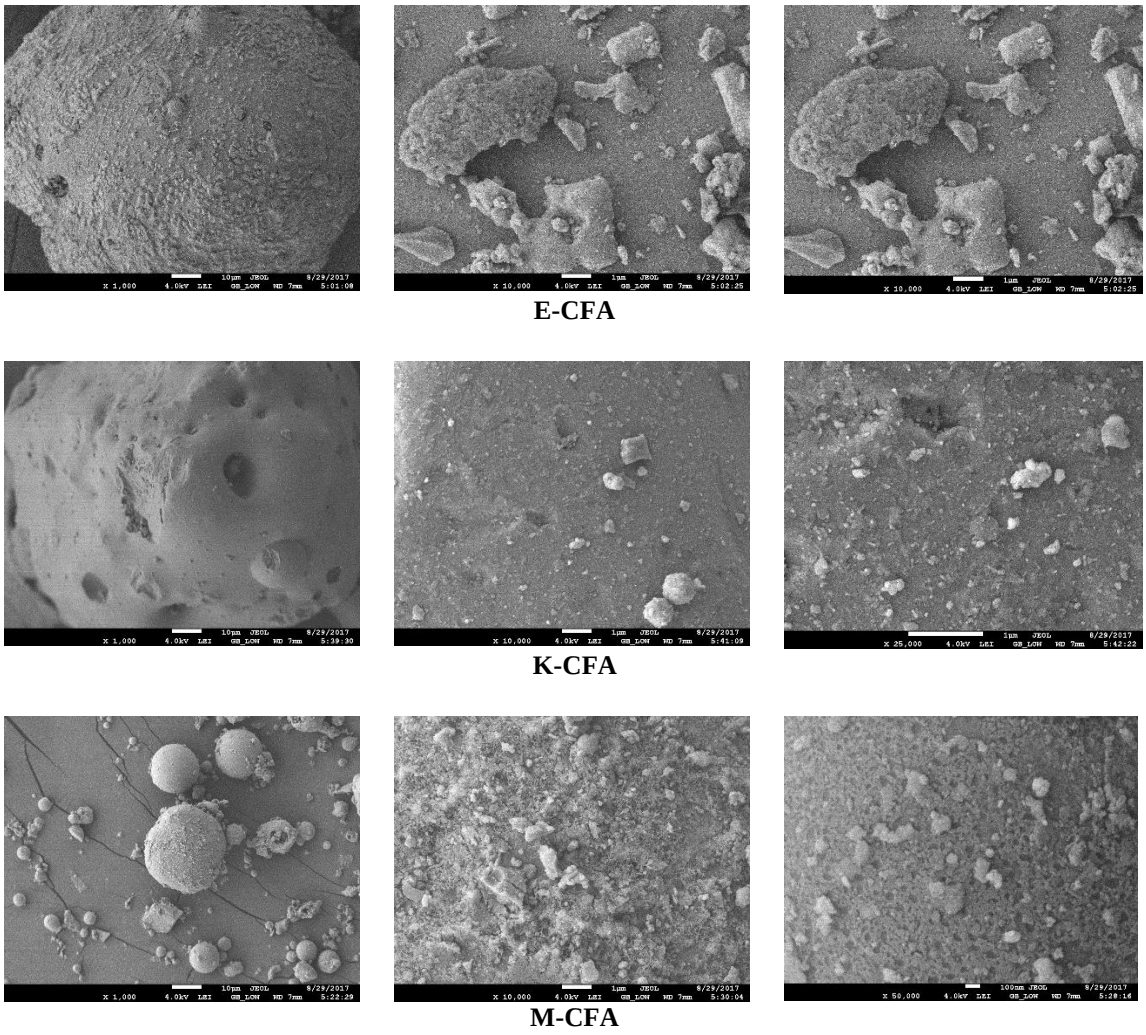

Figure B1. The SEM micrographs of E-CFA, K-CFA and M-CFA

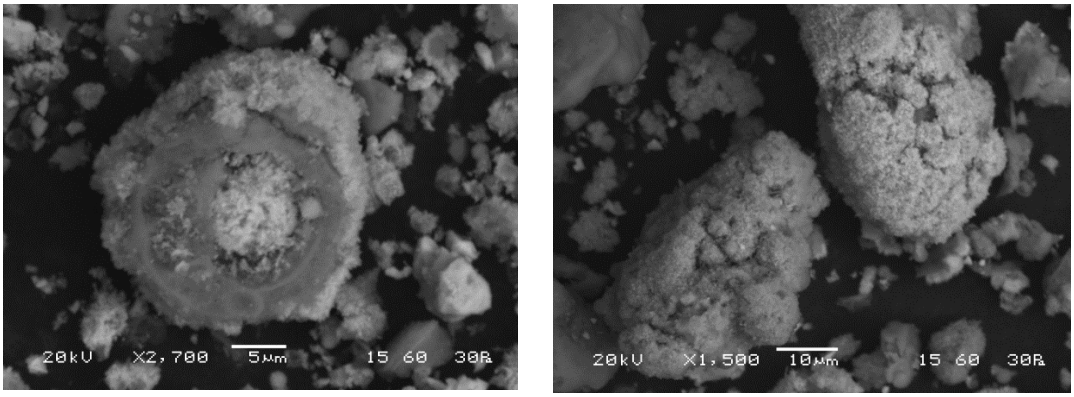

Figure B2. The SEM micrographs of K-ZFA

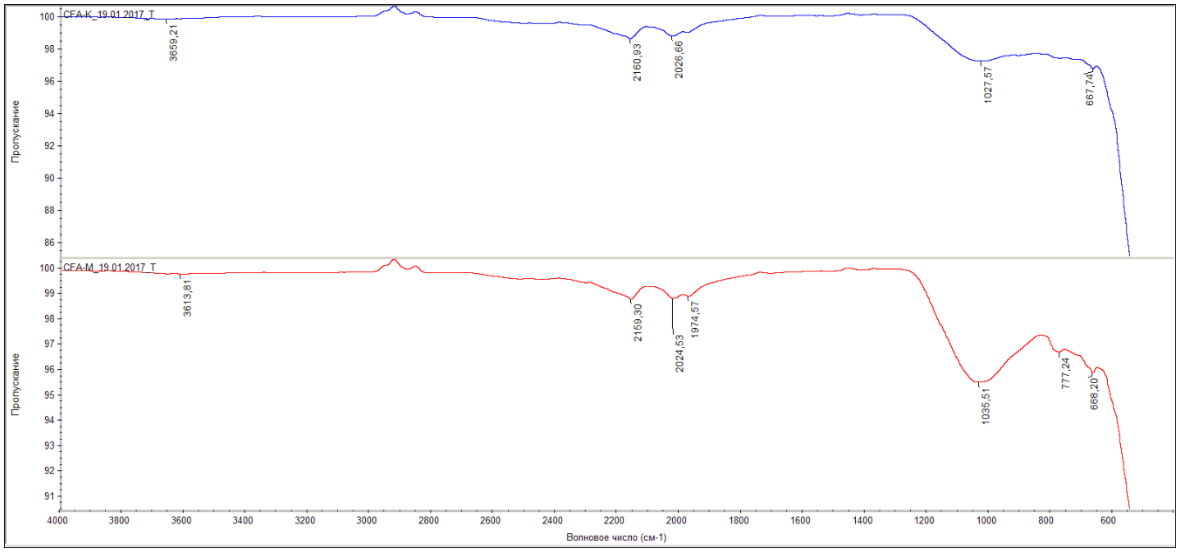

Figure B3. The FTIR spectrums of K-CFA and M-CFA

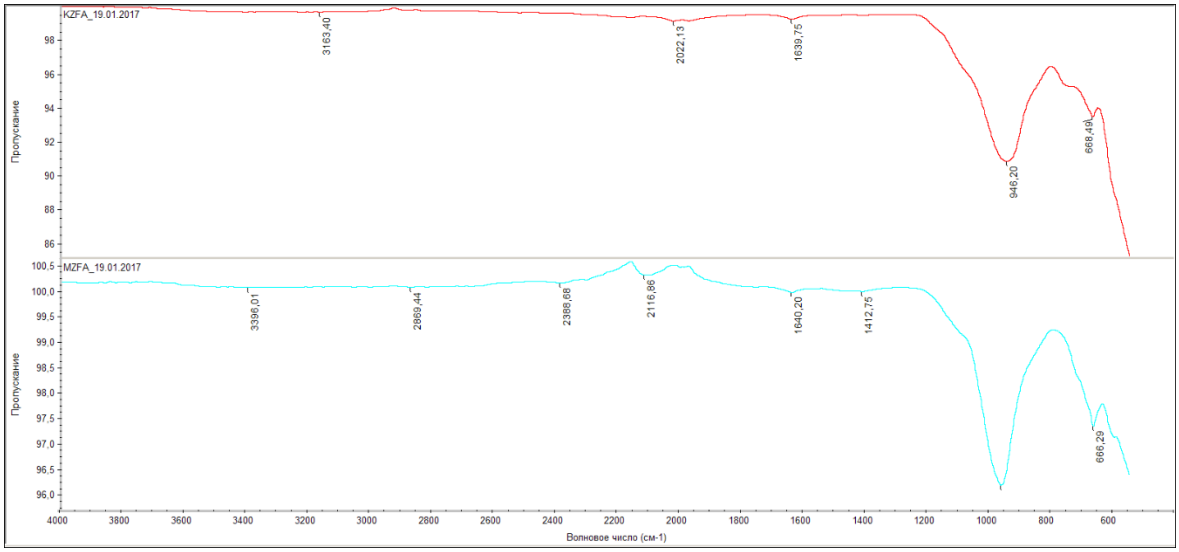

Figure B4. The FTIR spectrums of K-ZFA and M-ZFA

C. Appendices for Chapter 5

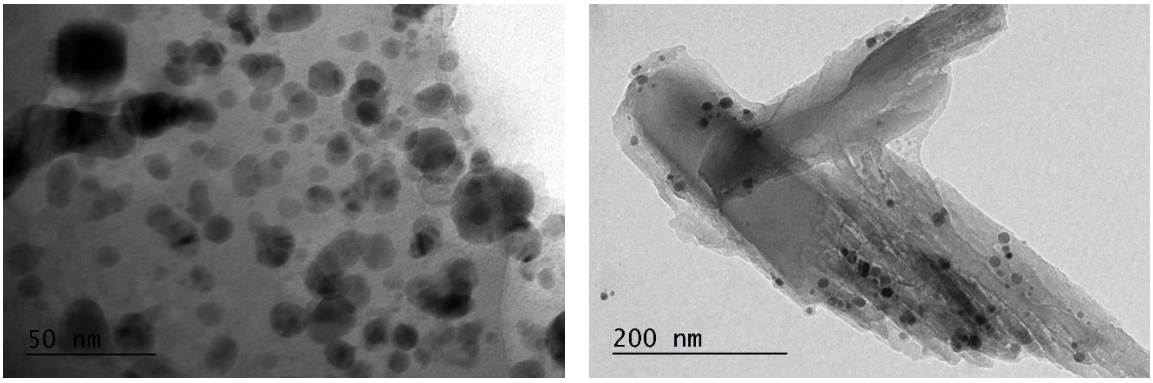

2wt.%-Ag-K-ZFA

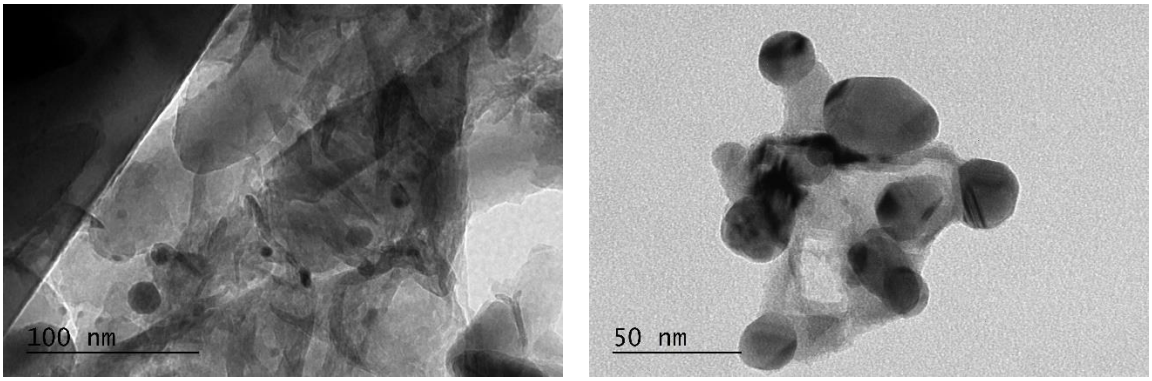

2wt.%-Ag-M-ZFA

Figure C1. The TEM images of nanocomposites

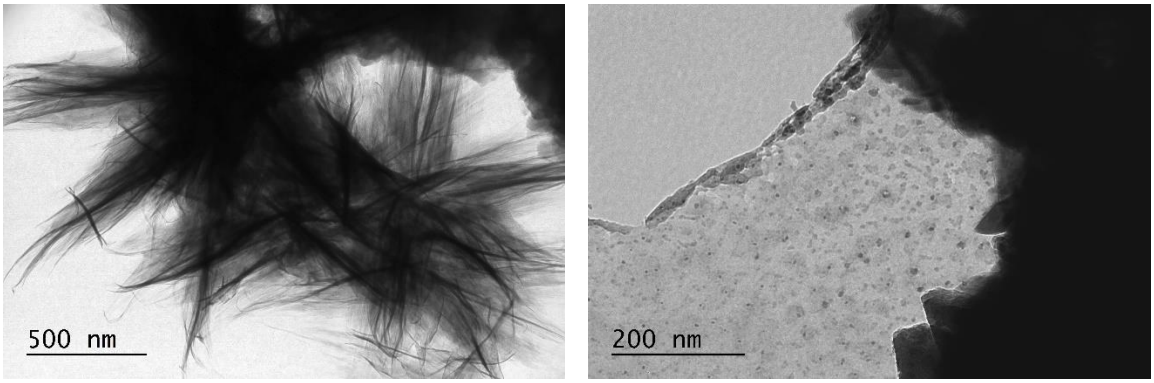

2wt.%-Ag-K-ZFA-Hg **2wt.%-Ag-M-ZFA-Hg**

Figure C2. The TEM images of nanocomposites loaded with Hg^{2+}

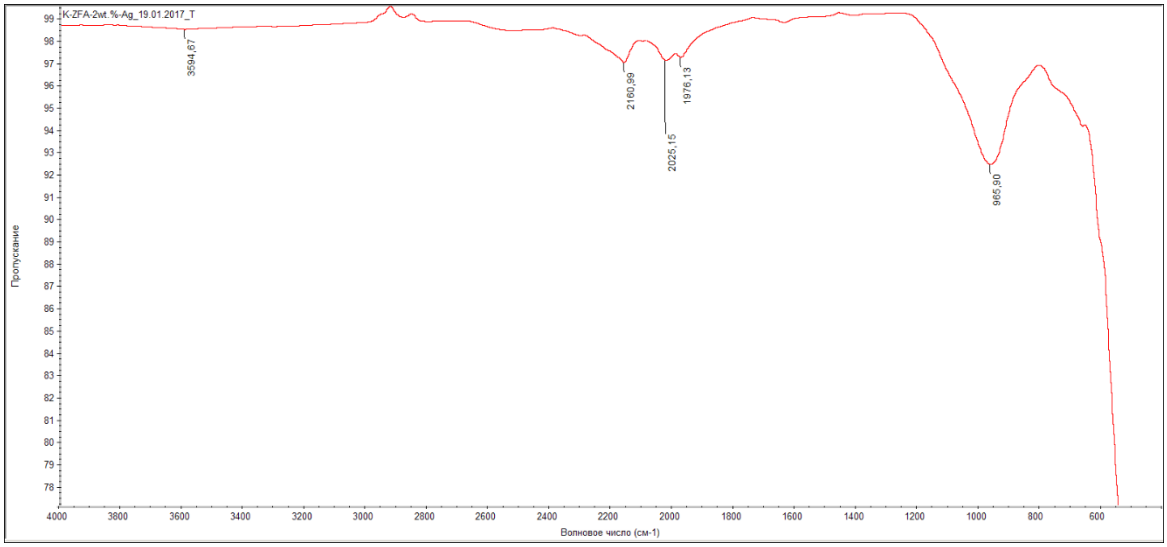

Figure C3. The FTIR spectrums of 2wt.%-Ag-K-ZFA

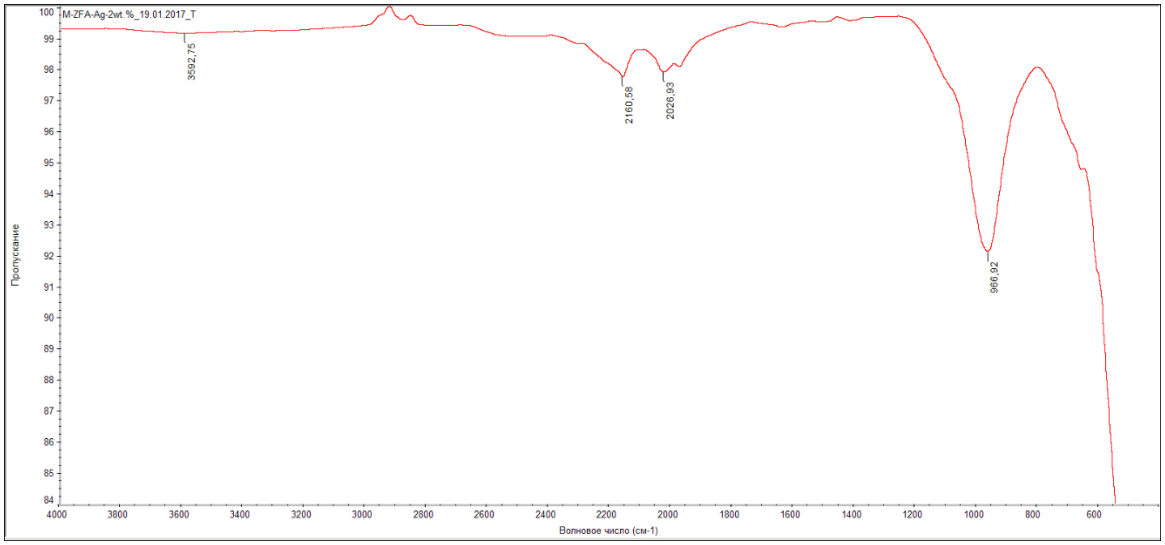

Figure C4. The FTIR spectrums of 2wt.%-Ag-M-ZFA

D. Appendices for Chapter 6

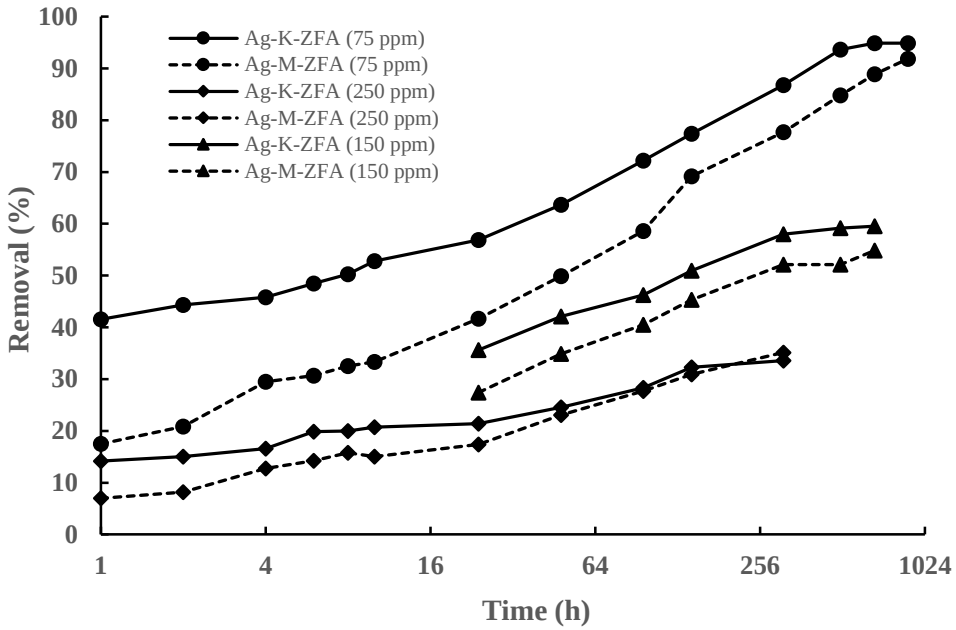

Figure D1. The semi-logarithmic curves of adsorption kinetics of I^- using nanocomposites

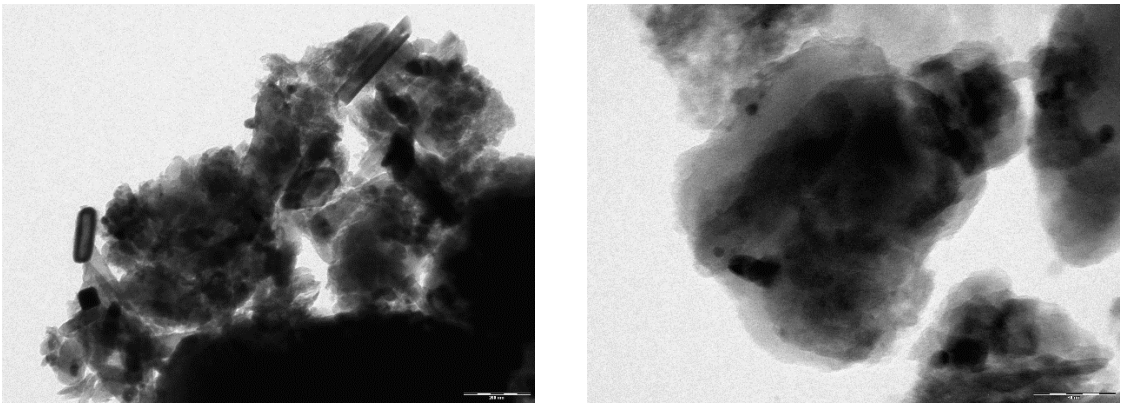

2wt.%-Ag-K-ZFA-I **2wt.%-Ag-M-ZFA-I**

Figure D2. The TEM images of nanocomposites loaded with I^-

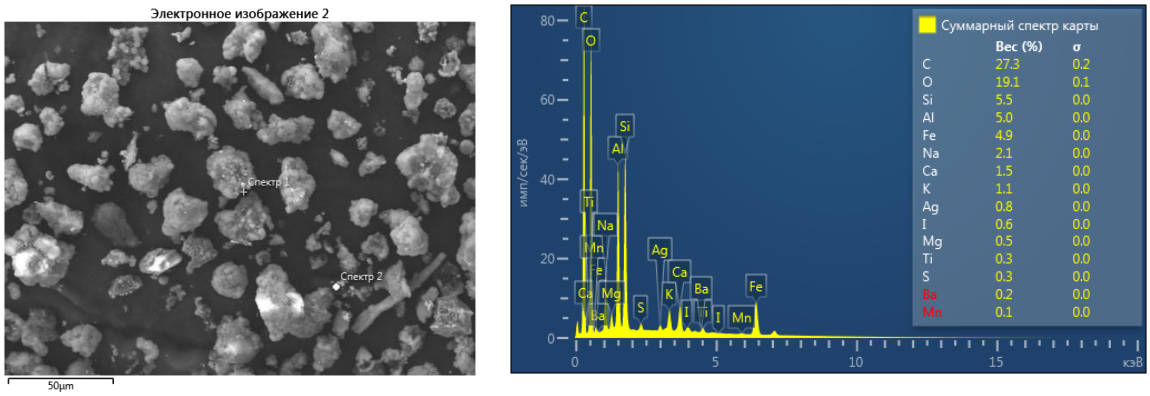

2wt.%-Ag-K-ZFA-I

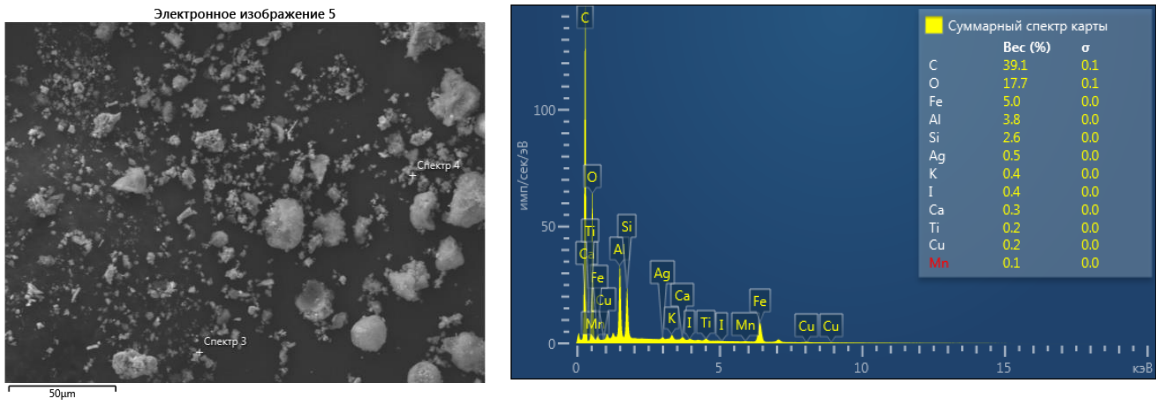

2wt.%-Ag-M-ZFA-I

Figure D3. The SEM-EDS analysis of nanocomposites loaded with I^-

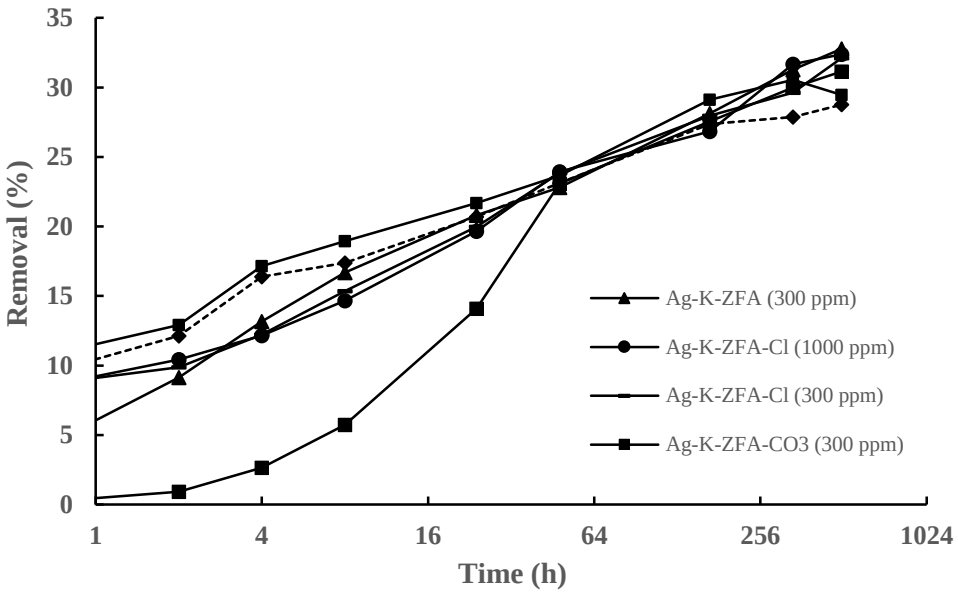

Figure D4. The semi-logarithmic curves of adsorption kinetics of competitive and co-existing anions effect on I^- removal using nanocomposite

BIBLIOGRAPHY

[1] Z. Tauanov, D. Shah, V. Inglezakis, P.K. Jamwal, Hydrothermal synthesis of zeolite production from coal fly ash: A heuristic approach and its optimization for system identification of conversion, J. Clean. Prod. 182 (2018) 616–623. doi:10.1016/j.jclepro.2018.02.047.

[2] Z. Tauanov, P.E. Tsakiridis, S.V. Mikhalovsky, V.J. Inglezakis, Synthetic coal fly ash-derived zeolites doped with silver nanoparticles for mercury (II) removal from water, J. Environ. Manage. 224 (2018) 164–171. doi:10.1016/j.jenvman.2018.07.049.

[3] Z. Tauanov, P.E. Tsakiridis, D. Shah, V.J. Inglezakis, Synthetic sodalite doped with silver nanoparticles: Characterization and mercury (II) removal from aqueous solutions, J. Environ. Sci. Heal. - Part A Toxic/Hazardous Subst. Environ. Eng. 0 (2019) 1–9. doi:10.1080/10934529.2019.1611129.

[4] Z. Tauanov, V.J. Inglezakis, Removal of iodide from water using silver nanoparticles-impregnated synthetic zeolites, Sci. Total Environ. 682 (2019) 259–270. doi:10.1016/j.scitotenv.2019.05.106.

[5] Z. Tauanov, D. Shah, G. Itskos, V. Inglezakis, Optimized Production of Coal Fly Ash Derived Synthetic Zeolites for Mercury Removal from Wastewater, IOP Conf. Ser. Mater. Sci. Eng. 230 (2017). doi:10.1088/1757-899X/230/1/012044.

[6] Z. Tauanov, L. Abylgazina, C. Spitas, G. Itskos, V. Inglezakis, Mineralogical, Microstructural and Thermal Characterization of Coal Fly Ash Produced from Kazakhstani Power Plants, IOP Conf. Ser. Mater. Sci. Eng. 230 (2017) 012046. doi:10.1088/1757-899X/230/1/012046.

[7] Z. Tauanov, D. Shah, V. Inglezakis, Silver Nanoparticles Impregnated Zeolites Derived from Coal Fly Ash: Effect of the Silver Loading on Adsorption of Mercury (II), Proceedings. 2 (2018) 647. doi:10.3390/proceedings2110647.

[8] S.S. Bukhari, J. Behin, H. Kazemian, S. Rohani, Conversion of coal fly ash to zeolite utilizing microwave and ultrasound energies: A review, Fuel. 140 (2015) 250–266. doi:10.1016/j.fuel.2014.09.077.

[9] Z.T. Yao, X.S. Ji, P.K. Sarker, J.H. Tang, L.Q. Ge, M.S. Xia, Y.Q. Xi, A comprehensive review on the applications of coal fly ash, Earth-Science Rev. 141 (2015) 105–121. doi:10.1016/j.earscirev.2014.11.016.

[10] World Coal Institute, the Coal Resource a Comprehensive Overview of Coal the Coal Resource Where Does Coal Come From ? What Is It, World Coal Inst. (2005) 1–44. doi:10.1017/CBO9781107415324.004.

[11] R.S. Blissett, N.A. Rowson, A review of the multi-component utilisation of coal fly ash, Fuel. 97 (2012) 1–23. doi:10.1016/j.fuel.2012.03.024.

[12] B. Jha, D.N. Singh, A three step process for purification of fly ash zeolites by hydrothermal treatment, Appl. Clay Sci. 90 (2014) 122–129. doi:10.1016/j.clay.2013.12.035.

[13] W. Chansiriwat, D. Tanangteerapong, K. Wantala, Synthesis of zeolite from coal fly ash by hydrothermal method without adding alumina and silica sources: Effect of

aging temperature and time, Sains Malaysiana. 45 (2016) 1723–1731.

[14] V.K. Jha, M. Matsuda, M. Miyake, Sorption properties of the activated carbon-zeolite composite prepared from coal fly ash for Ni2+, Cu2+, Cd2+ and Pb2+, J. Hazard. Mater. 160 (2008) 148–153. doi:10.1016/j.jhazmat.2008.02.107.

[15] C. Belviso, F. Cavalcante, S. Di Gennaro, A. Lettino, A. Palma, P. Ragone, S. Fiore, Removal of Mn from aqueous solution using fly ash and its hydrothermal synthetic zeolite, J. Environ. Manage. 137 (2014) 16–22. doi:10.1016/j.jenvman.2014.01.040.

[16] D. Czarna, P. Baran, P. Kunecki, R. Panek, R. Żmuda, M. Wdowin, Synthetic zeolites as potential sorbents of mercury from wastewater occurring during wet FGD processes of flue gas, J. Clean. Prod. 172 (2018) 2636–2645. doi:10.1016/j.jclepro.2017.11.147.

[17] M. Visa, A.M. Chelaru, Hydrothermally modified fly ash for heavy metals and dyes removal in advanced wastewater treatment, Appl. Surf. Sci. 303 (2014) 14–22. doi:10.1016/j.apsusc.2014.02.025.

[18] J. Xie, Z. Wang, D. Wu, H. Kong, Synthesis and properties of zeolite/hydrated iron oxide composite from coal fly ash as efficient adsorbent to simultaneously retain cationic and anionic pollutants from water, Fuel. 116 (2014) 71–76. doi:10.1016/j.fuel.2013.07.126.

[19] J. Wang, D. Li, F. Ju, L. Han, L. Chang, W. Bao, Supercritical hydrothermal synthesis of zeolites from coal fly ash for mercury removal from coal derived gas, Fuel Process. Technol. 136 (2015) 96–105. doi:10.1016/j.fuproc.2014.10.020.

[20] G. Itskos, A. Koutsianos, N. Koukouzas, C. Vasilatos, Zeolite development from fly ash and utilization in lignite mine-water treatment, Int. J. Miner. Process. 139 (2015) 43–50. doi:10.1016/j.minpro.2015.04.011.

[21] M. Attari, S.S. Bukhari, H. Kazemian, S. Rohani, A low-cost adsorbent from coal fly ash for mercury removal from industrial wastewater, J. Environ. Chem. Eng. 5 (2017) 391–399. doi:10.1016/j.jece.2016.12.014.

[22] M. Wdowin, M.M. Wiatros-Motyka, R. Panek, L.A. Stevens, W. Franus, C.E. Snape, Experimental study of mercury removal from exhaust gases, Fuel. 128 (2014) 451–457. doi:10.1016/j.fuel.2014.03.041.

[23] M. Wdowin, M. Macherzyński, R. Panek, J. Górecki, W. Franus, Investigation of the sorption of mercury vapour from exhaust gas by an Ag-X zeolite, Clay Miner. 50 (2015) 31–40. doi:10.1180/claymin.2015.050.1.04.

[24] W. Yang, A. Hussain, J. Zhang, Y. Liu, Removal of Elemental Mercury from Flue Gas Using Red Mud Impregnated by KBr and KI Reagent, Chem. Eng. J. (2018). doi:10.1016/j.cej.2018.02.023.

[25] M. Rumayor, K. Svoboda, J. Švehla, M. Pohořelý, M. Šyc, Mercury removal from MSW incineration flue gas by mineral-based sorbents, Waste Manag. 73 (2017) 265–270. doi:10.1016/j.wasman.2017.12.007.

[26] P.T. Huong, B.K. Lee, J. Kim, C.H. Lee, Nitrophenols removal from aqueous medium using Fe-nano mesoporous zeolite, Mater. Des. 101 (2016) 210–217.

doi:10.1016/j.matdes.2016.04.020.

[27] D. Jiraroj, S. Tungasmita, D.N. Tungasmita, Silver ions and silver nanoparticles in zeolite A composites for antibacterial activity, Powder Technol. 264 (2014) 418–422. doi:10.1016/j.powtec.2014.05.049.

[28] J. Gou, Q. Ma, X. Deng, Y. Cui, H. Zhang, X. Cheng, X. Li, M. Xie, Q. Cheng, Fabrication of Ag2O/TiO2-Zeolite composite and its enhanced solar light photocatalytic performance and mechanism for degradation of norfloxacin, Chem. Eng. J. 308 (2017) 818–826. doi:10.1016/j.cej.2016.09.089.

[29] J. Liu, D. Wang, J.F. Chen, Y. Zhang, Cobalt nanoparticles imbedded into zeolite crystals: A tailor-made catalyst for one-step synthesis of gasoline from syngas, Int. J. Hydrogen Energy. 41 (2016) 21965–21978. doi:10.1016/j.ijhydene.2016.10.004.

[30] Y. Tonbul, M. Zahmakiran, S. Özkar, Iridium(0) nanoparticles dispersed in zeolite framework: A highly active and long-lived green nanocatalyst for the hydrogenation of neat aromatics at room temperature, Appl. Catal. B Environ. 148–149 (2014) 466–472. doi:10.1016/j.apcatb.2013.11.017.

[31] J. Goscianska, M. Ptaszkowska-Koniarz, M. Frankowski, M. Franus, R. Panek, W. Franus, Removal of phosphate from water by lanthanum-modified zeolites obtained from fly ash, J. Colloid Interface Sci. 513 (2018) 72–81. doi:10.1016/j.jcis.2017.11.003.

[32] Y. He, H. Lin, Y. Dong, Q. Liu, L. Wang, Simultaneous removal of ammonium and phosphate by alkaline-activated and lanthanum-impregnated zeolite, Chemosphere. 164 (2016) 387–395. doi:10.1016/j.chemosphere.2016.08.110.

[33] A. Henglein, Colloidal silver nanoparticles: photochemical preparation and interaction with O2, CCl4, and some metal ions, Chem. Mater. 2 (1998) 444–450.

[34] P. Mao, Y. Liu, X. Liu, Y. Wang, J. Liang, Q. Zhou, Y. Dai, Y. Jiao, S. Chen, Y. Yang, Bimetallic AgCu/Cu2O hybrid for the synergetic adsorption of iodide from solution, Chemosphere. 180 (2017) 317–325. doi:10.1016/j.chemosphere.2017.04.038.

[35] M. Zahmakiran, Preparation and characterization of LTA-type zeolite framework dispersed ruthenium nanoparticles and their catalytic application in the hydrolytic dehydrogenation of ammonia-borane for efficient hydrogen generation, Mater. Sci. Eng. B Solid-State Mater. Adv. Technol. 177 (2012) 606–613. doi:10.1016/j.mseb.2012.03.003.

[36] L. Akhigbe, S. Ouki, D. Saroj, Disinfection and removal performance for Escherichia coli and heavy metals by silver-modified zeolite in a fixed bed column, Chem. Eng. J. 295 (2016) 92–98. doi:10.1016/j.cej.2016.03.020.

[37] C. Belviso, State-of-the-art applications of fly ash from coal and biomass: A focus on zeolite synthesis processes and issues, Prog. Energy Combust. Sci. 000 (2017) 1–27. doi:10.1016/j.pecs.2017.10.004.

[38] U. Bhattacharjee, T.C. Kandpal, Potential of fly ash utilisation in India, Energy. 27 (2002) 151–166. doi:https://doi.org/10.1016/S0360-5442(01)00065-2.

[39] S. Wang, T. Terdkiatburana, M.O. Tadé, Single and co-adsorption of heavy metals and humic acid on fly ash, Sep. Purif. Technol. 58 (2008) 353–358. doi:https://doi.org/10.1016/j.seppur.2007.05.009.

[40] S. V Vassilev, C.G. Vassileva, Methods for Characterization of Composition of Fly Ashes from Coal-Fired Power Stations: A Critical Overview, Energy & Fuels. 19 (2005) 1084–1098. doi:10.1021/ef049694d.

[41] S. V Vassilev, C.G. Vassileva, Geochemistry of coals, coal ashes and combustion wastes from coal-fired power stations, Fuel Process. Technol. 51 (1997) 19–45. doi:https://doi.org/10.1016/S0378-3820(96)01082-X.

[42] S. V Vassilev, R. Menendez, D. Alvarez, M. Diaz-Somoano, M.R. Martinez-Tarazona, Phase-mineral and chemical composition of coal fly ashes as a basis for their multicomponent utilization. 1. Characterization of feed coals and fly ashes☆, Fuel. 82 (2003) 1793–1811. doi:https://doi.org/10.1016/S0016-2361(03)00123-6.

[43] R.S. Iyer, J.A. Scott, Power station fly ash - A review of value-added utilization outside of the construction industry, Resour. Conserv. Recycl. 31 (2001) 217–228. doi:10.1016/S0921-3449(00)00084-7.

[44] G.L. Fisher, B.A. Prentice, D. Silberman, J.M. Ondov, A.H. Biermann, R.C. Ragaini, A.R. McFarland, Physical and morphological studies of size-classified coal fly ash, Environ. Sci. Technol. 12 (1978) 447–451. doi:10.1021/es60140a008.

[45] A. Duta, M. Visa, Simultaneous removal of two industrial dyes by adsorption and photocatalysis on a fly-ash-TiO2 composite, J. Photochem. Photobiol. A Chem. 306 (2015) 21–30. doi:10.1016/j.jphotochem.2015.03.007.

[46] M. Visa, Synthesis and characterization of new zeolite materials obtained from fly ash for heavy metals removal in advanced wastewater treatment, Powder Technol. 294 (2016) 338–347. doi:10.1016/j.powtec.2016.02.019.

[47] V.K. Jha, M. Nagae, M. Matsuda, M. Miyake, Zeolite formation from coal fly ash and heavy metal ion removal characteristics of thus-obtained Zeolite X in multi-metal systems, J. Environ. Manage. 90 (2009) 2507–2514. doi:10.1016/j.jenvman.2009.01.009.

[48] M. Izquierdo, X. Querol, Leaching behaviour of elements from coal combustion fly ash: An overview, Int. J. Coal Geol. 94 (2012) 54–66. doi:https://doi.org/10.1016/j.coal.2011.10.006.

[49] J. Jankowski, C.R. Ward, D. French, S. Groves, Mobility of trace elements from selected Australian fly ashes and its potential impact on aquatic ecosystems, Fuel. 85 (2006) 243–256. doi:https://doi.org/10.1016/j.fuel.2005.05.028.

[50] J. Jankowski, C.R. Ward, D. French, S. Groves, Mobility of trace elements from selected Australian fly ashes and its potential impact on aquatic ecosystems, Fuel. 85 (2006) 243–256. doi:https://doi.org/10.1016/j.fuel.2005.05.028.

[51] K.K. Panday, G. Prasad, V.N. Singh, Copper(II) removal from aqueous solutions by fly ash, Water Res. 19 (1985) 869–873. doi:https://doi.org/10.1016/0043-1354(85)90145-9.

[52] H. Cho, D. Oh, K. Kim, A study on removal characteristics of heavy metals from aqueous solution by fly ash, J. Hazard. Mater. 127 (2005) 187–195. doi:https://doi.org/10.1016/j.jhazmat.2005.07.019.

[53] B. Bayat, Comparative study of adsorption properties of Turkish fly ashes: I. The case of nickel(II), copper(II) and zinc(II), J. Hazard. Mater. 95 (2002) 251–273. doi:https://doi.org/10.1016/S0304-3894(02)00140-1.

[54] J. Ayala, F. Blanco, P. García, P. Rodriguez, J. Sancho, Asturian fly ash as a heavy metals removal material, Fuel. 77 (1998) 1147–1154. doi:https://doi.org/10.1016/S0016-2361(98)00027-1.

[55] I.J. Alinnor, Adsorption of heavy metal ions from aqueous solution by fly ash, Fuel. 86 (2007) 853–857. doi:https://doi.org/10.1016/j.fuel.2006.08.019.

[56] E. Diamadopoulos, S. Ioannidis, G.P. Sakellaropoulos, As(V) removal from aqueous solutions by fly ash, Water Res. 27 (1993) 1773–1777. doi:https://doi.org/10.1016/0043-1354(93)90116-Y.

[57] S.S. Banerjee, M. V Joshi, R. V Jayaram, Removal of Cr(VI) and Hg(II) from Aqueous Solutions Using Fly Ash and Impregnated Fly Ash, Sep. Sci. Technol. 39 (2005) 1611–1629. doi:10.1081/SS-120030778.

[58] J. Pattanayak, K. Mondal, S. Mathew, S.B. Lalvani, A parametric evaluation of the removal of As(V) and As(III) by carbon-based adsorbents, Carbon N. Y. 38 (2000) 589–596. doi:https://doi.org/10.1016/S0008-6223(99)00144-X.

[59] Z. Aksu, J. Yener, The usage of dried activated sludge and fly ash wastes in phenol biosorption/adsorption: Comparison with granular activated carbon, J. Environ. Sci. Heal. Part A. 34 (1999) 1777–1796. doi:10.1080/10934529909376928.

[60] Z. Aksu, J. Yener, A comparative adsorption/biosorption study of mono-chlorinated phenols onto various sorbents, Waste Manag. 21 (2001) 695–702. doi:https://doi.org/10.1016/S0956-053X(01)00006-X.

[61] H. Nollet, M. Roels, P. Lutgen, P. Van der Meeren, W. Verstraete, Removal of PCBs from wastewater using fly ash, Chemosphere. 53 (2003) 655–665. doi:https://doi.org/10.1016/S0045-6535(03)00517-4.

[62] M. Matheswaran, T. Karunanithi, Adsorption of Chrysoidine R by using fly ash in batch process, J. Hazard. Mater. 145 (2007) 154–161. doi:https://doi.org/10.1016/j.jhazmat.2006.11.006.

[63] N. Singh, Adsorption of herbicides on coal fly ash from aqueous solutions, J. Hazard. Mater. 168 (2009) 233–237. doi:https://doi.org/10.1016/j.jhazmat.2009.02.016.

[64] P. Davini, Investigation of flue gas desulphurization by fly ash and calcium hydroxide mixtures, Resour. Conserv. Recycl. 15 (1995) 193–201. doi:https://doi.org/10.1016/0921-3449(95)00029-1.

[65] G.Q. Lu, D.D. Do, Adsorption properties of fly ash particles for NOx removal from flue gases, Fuel Process. Technol. 27 (1991) 95–107. doi:https://doi.org/10.1016/0378-3820(91)90011-Z.

[66] M. Sarmah, B.P. Baruah, P. Khare, A comparison between CO2 capturing capacities of fly ash based composites of MEA/DMA and DEA/DMA, Fuel Process. Technol. 106 (2013) 490–497. doi:https://doi.org/10.1016/j.fuproc.2012.09.017.

[67] N.M. Agyei, C.A. Strydom, J.H. Potgieter, The removal of phosphate ions from aqueous solution by fly ash, slag, ordinary Portland cement and related blends, Cem. Concr. Res. 32 (2002) 1889–1897. doi:https://doi.org/10.1016/S0008-8846(02)00888-8.

[68] A. Ugurlu, B. Salman, Phosphorus removal by fly ash, Environ. Int. 24 (1998) 911–918. doi:https://doi.org/10.1016/S0160-4120(98)00079-8.

[69] S. Wang, T. Terdkiatburana, M.O. Tadé, Single and co-adsorption of heavy metals and humic acid on fly ash, Sep. Purif. Technol. 58 (2008) 353–358. doi:https://doi.org/10.1016/j.seppur.2007.05.009.

[70] M. Akhtar, S.M. Hasany, M.I. Bhanger, S. Iqbal, Low cost sorbents for the removal of methyl parathion pesticide from aqueous solutions, Chemosphere. 66 (2007) 1829–1838. doi:https://doi.org/10.1016/j.chemosphere.2006.09.006.

[71] A. González, R. Navia, N. Moreno, Fly ashes from coal and petroleum coke combustion: current and innovative potential applications, Waste Manag. Res. 27 (2009) 976–987. doi:10.1177/0734242X09103190.

[72] P. Nath, P. Sarker, Effect of Fly Ash on the Durability Properties of High Strength Concrete, Procedia Eng. 14 (2011) 1149–1156. doi:https://doi.org/10.1016/j.proeng.2011.07.144.

[73] M.J. McCarthy, R.K. Dhir, Development of high volume fly ash cements for use in concrete construction, Fuel. 84 (2005) 1423–1432. doi:https://doi.org/10.1016/j.fuel.2004.08.029.

[74] A. Durán-Herrera, C.A. Juárez, P. Valdez, D.P. Bentz, Evaluation of sustainable high-volume fly ash concretes, Cem. Concr. Compos. 33 (2011) 39–45. doi:10.1016/j.cemconcomp.2010.09.020.

[75] R.-U.-D. Nassar, P. Soroushian, T. Ghebrab, Field investigation of high-volume fly ash pavement concrete, Resour. Conserv. Recycl. 73 (2013) 78–85. doi:https://doi.org/10.1016/j.resconrec.2013.01.006.

[76] R. Kumar, S. Kumar, S.P. Mehrotra, Towards sustainable solutions for fly ash through mechanical activation, Resour. Conserv. Recycl. 52 (2007) 157–179. doi:https://doi.org/10.1016/j.resconrec.2007.06.007.

[77] S. Kumar, R. Kumar, T.C. Alex, A. Bandopadhyay, S.P. Mehrotra, Influence of reactivity of fly ash on geopolymerisation, Adv. Appl. Ceram. 106 (2007) 120–127. doi:10.1179/174367607X159293.

[78] S.E.W. Djwantoro Hardjito Dody M. J. Sumajouw, and B.Vijaya Rangan, On the Development of Fly Ash-Based Geopolymer Concrete, Mater. J. 101 (n.d.). doi:10.14359/13485.

[79] J. Temuujin, A. van Riessen, K.J.D. MacKenzie, Preparation and characterisation of fly ash based geopolymer mortars, Constr. Build. Mater. 24 (2010) 1906–1910.

doi:https://doi.org/10.1016/j.conbuildmat.2010.04.012.

[80] V.C. Pandey, N. Singh, Impact of fly ash incorporation in soil systems, Agric. Ecosyst. Environ. 136 (2010) 16–27. doi:https://doi.org/10.1016/j.agee.2009.11.013.

[81] V. Manoharan, I.A.M. Yunusa, P. Loganathan, R. Lawrie, C.G. Skilbeck, M.D. Burchett, B.R. Murray, D. Eamus, Assessments of Class F fly ashes for amelioration of soil acidity and their influence on growth and uptake of Mo and Se by canola, Fuel. 89 (2010) 3498–3504. doi:https://doi.org/10.1016/j.fuel.2010.06.028.

[82] S. Jala, D. Goyal, Fly ash as a soil ameliorant for improving crop production—a review, Bioresour. Technol. 97 (2006) 1136–1147. doi:https://doi.org/10.1016/j.biortech.2004.09.004.

[83] T. Matsi, V.Z. Keramidas, Fly ash application on two acid soils and its effect on soil salinity, pH, B, P and on ryegrass growth and composition, Environ. Pollut. 104 (1999) 107–112. doi:https://doi.org/10.1016/S0269-7491(98)00145-6.

[84] G.Y. Jayasinghe, Y. Tokashiki, M. Kitou, Use of synthetic soil aggregates as a containerized growth medium component to substitute peat in the ornamental plant production, Arch. Agron. Soil Sci. 56 (2010) 183–199. doi:10.1080/03650340902914024.

[85] J. Chen, Y. Li, Amendment of Fly Ash to Container Substrates for Ornamental Plant Production BT - Coal Combustion Byproducts and Environmental Issues, in: K.S. Sajwan, I. Twardowska, T. Punshon, A.K. Alva (Eds.), Springer New York, New York, NY, 2006: pp. 177–183.

[86] S.A. Sankari, P. Narayanasamy, Bio-efficacy of flyash-based herbal pesticides against pests of rice and vegetables, Curr. Sci. 92 (2007) 811–816. http://www.jstor.org/stable/24097813.

[87] M. Basu, M. Pande, P.B.S. Bhadoria, S.C. Mahapatra, Potential fly-ash utilization in agriculture: A global review, Prog. Nat. Sci. 19 (2009) 1173–1186. doi:https://doi.org/10.1016/j.pnsc.2008.12.006.

[88] M. Erol, S. Küçükbayrak, A. Ersoy-Meriçboyu, Comparison of the properties of glass, glass–ceramic and ceramic materials produced from coal fly ash, J. Hazard. Mater. 153 (2008) 418–425. doi:https://doi.org/10.1016/j.jhazmat.2007.08.071.

[89] A. Kara, H. Kurama, Y. Kara, S. Kurama, Utilization of Coal Combustion Fly Ash in Terracotta Bodies , Key Eng. Mater. 264–268 (2004) 2513–2516. doi:10.4028/www.scientific.net/KEM.264-268.2513.

[90] Z. Jing, Y.-Y. Li, S. Cao, Y. Liu, Performance of double-layer biofilter packed with coal fly ash ceramic granules in treating highly polluted river water, Bioresour. Technol. 120 (2012) 212–217. doi:https://doi.org/10.1016/j.biortech.2012.06.069.

[91] N.U. Kockal, Utilisation of different types of coal fly ash in the production of ceramic tiles, Bol. La Soc. Esp. Ceram. y Vidr. 51 (2012) 297–304. doi:10.3989/cyv.412012.

[92] H. Shao, K. Liang, F. Zhou, G. Wang, F. Peng, Characterization of cordierite-based glass-ceramics produced from fly ash, J. Non. Cryst. Solids. 337 (2004) 157–160. doi:https://doi.org/10.1016/j.jnoncrysol.2004.04.003.

[93] Y. He, W. Cheng, H. Cai, Characterization of α-cordierite glass-ceramics from fly ash, J. Hazard. Mater. 120 (2005) 265–269. doi:https://doi.org/10.1016/j.jhazmat.2004.10.028.

[94] R. Sokolar, L. Vodova, The effect of fluidized fly ash on the properties of dry pressed ceramic tiles based on fly ash–clay body, Ceram. Int. 37 (2011) 2879–2885. doi:https://doi.org/10.1016/j.ceramint.2011.05.005.

[95] X. Lingling, G. Wei, W. Tao, Y. Nanru, Study on fired bricks with replacing clay by fly ash in high volume ratio, Constr. Build. Mater. 19 (2005) 243–247. doi:https://doi.org/10.1016/j.conbuildmat.2004.05.017.

[96] P. Asokan, M. Saxena, S.R. Asolekar, Coal combustion residues—environmental implications and recycling potentials, Resour. Conserv. Recycl. 43 (2005) 239–262. doi:https://doi.org/10.1016/j.resconrec.2004.06.003.

[97] P.K. Rohatgi, R.Q. Guo, Opportunities of using fly ash particles for synthesis of composites, Fuel Energy Abstr. 39 (1998) 28.

[98] C.S. Ramesh, S.K. Seshadri, K.J.L. Iyer, Wear resistance of nickel-fly ash composite coatings, Wear. 145 (1991) 189–195. doi:https://doi.org/10.1016/0043-1648(91)90247-R.

[99] R.S. Iyer, J.A. Scott, Power station fly ash - A review of value-added utilization outside of the construction industry, Resour. Conserv. Recycl. 31 (2001) 217–228. doi:10.1016/S0921-3449(00)00084-7.

[100] T. Ohtake, K. Uchida, F. Ikazaki, M. Kawamura, T. Ohkuba, K. Kamiya, Synthesis of Mullite from Fly Ash and Alumina Powder Mixture, J. Ceram. Soc. Japan. 99 (1991) 239–243. doi:10.2109/jcersj.99.239.

[101] J.-Y. Hwang, X. Huang, A.M. Hein, Synthesizing mullite from beneficiated fly ash, JOM. 46 (1994) 36–39. doi:10.1007/BF03220694.

[102] Y. Fang, Y. Chen, M.R. Silsbee, D.M. Roy, Microwave sintering of flyash, Mater. Lett. 27 (1996) 155–159. doi:https://doi.org/10.1016/0167-577X(96)80007-3.

[103] B. Gutiérrez, C. Pazos, J. Coca, Recovery of gallium from coal fly ash by a dual reactive extraction process, Waste Manag. Res. 15 (1997) 371–382. doi:https://doi.org/10.1006/wmre.1996.0093.

[104] C.A. Pickles, A. McLean, C.B. Alcock, R.N. Nikolic, Plasma Recovery of Metal Values From Flyash, Can. Metall. Q. 29 (1990) 193–200. doi:10.1179/cmq.1990.29.3.193.

[105] I.J. Lin, N. Malts, Y. Shindler, The Complex Chemical Treatment of Alumina–Silica-Containing Materials, J. Mater. Synth. Process. 6 (1998) 27–35. doi:10.1023/A:1022655008877.

[106] P. Miretzky, A.F. Cirelli, Hg(II) removal from water by chitosan and chitosan derivatives: A review, J. Hazard. Mater. 167 (2009) 10–23. doi:https://doi.org/10.1016/j.jhazmat.2009.01.060.

[107] H. Parham, B. Zargar, R. Shiralipour, Fast and efficient removal of mercury from

water samples using magnetic iron oxide nanoparticles modified with 2-mercaptobenzothiazole, J. Hazard. Mater. 205–206 (2012) 94–100. doi:https://doi.org/10.1016/j.jhazmat.2011.12.026.

[108] J.G. Yu, B.Y. Yue, X.W. Wu, Q. Liu, F.P. Jiao, X.Y. Jiang, X.Q. Chen, Removal of mercury by adsorption: a review, Environ. Sci. Pollut. Res. 23 (2016) 5056–5076. doi:10.1007/s11356-015-5880-x.

[109] A.L. Choi, S. Cordier, P. Weihe, P. Grandjean, Negative Confounding in the Evaluation of Toxicity: The Case of Methylmercury in Fish and Seafood, Crit. Rev. Toxicol. 38 (2008) 877–893. doi:10.1080/10408440802273164.

[110] H.-W. Hsiao, S.M. Ullrich, T.W. Tanton, Burdens of mercury in residents of Temirtau, Kazakhstan: I: Hair mercury concentrations and factors of elevated hair mercury levels, Sci. Total Environ. 409 (2011) 2272–2280. doi:https://doi.org/10.1016/j.scitotenv.2009.12.040.

[111] C.F. Carolin, P.S. Kumar, A. Saravanan, G.J. Joshiba, M. Naushad, Efficient techniques for the removal of toxic heavy metals from aquatic environment: A review, J. Environ. Chem. Eng. 5 (2017) 2782–2799. doi:10.1016/j.jece.2017.05.029.

[112] V.M. Yau, P.G. Green, C.P. Alaimo, C.K. Yoshida, M. Lutsky, G.C. Windham, G. Delorenze, M. Kharrazi, J.K. Grether, L.A. Croen, Prenatal and neonatal peripheral blood mercury levels and autism spectrum disorders, Environ. Res. 133 (2014) 294–303. doi:https://doi.org/10.1016/j.envres.2014.04.034.

[113] R. Singh, N. Gautam, A. Mishra, R. Gupta, Heavy metals and living systems: An overview, Indian J. Pharmacol. 43 (2011) 246–253. doi:10.4103/0253-7613.81505.

[114] Y.K. Henneberry, T.E.C. Kraus, J.A. Fleck, D.P. Krabbenhoft, P.M. Bachand, W.R. Horwath, Removal of inorganic mercury and methylmercury from surface waters following coagulation of dissolved organic matter with metal-based salts, Sci. Total Environ. 409 (2011) 631–637. doi:https://doi.org/10.1016/j.scitotenv.2010.10.030.

[115] S. Heaven, M.A. Ilyushchenko, I.M. Kamberov, M.I. Politikov, T.W. Tanton, S.M. Ullrich, E.P. Yanin, Mercury in the River Nura and its floodplain, Central Kazakhstan: II. Floodplain soils and riverbank silt deposits, Sci. Total Environ. 260 (2000) 45–55. doi:10.1016/S0048-9697(00)00566-0.

[116] C.-Y. Wu, H. Mouri, S.-S. Chen, D.-Z. Zhang, M. Koga, J. Kobayashi, Removal of trace-amount mercury from wastewater by forward osmosis, J. Water Process Eng. 14 (2016) 108–116. doi:https://doi.org/10.1016/j.jwpe.2016.10.010.

[117] J. Jang, D.S. Lee, Magnetite nanoparticles supported on organically modi fi ed montmorillonite for adsorptive removal of iodide from aqueous solution : Optimization using response surface methodology, Sci. Total Environ. 615 (2018) 549–557. doi:10.1016/j.scitotenv.2017.09.324.

[118] A. Bo, S. Sarina, Z. Zheng, D. Yang, H. Liu, H. Zhu, Removal of radioactive iodine from water using Ag2O grafted titanate nanolamina as efficient adsorbent, J. Hazard. Mater. 246–247 (2013) 199–205. doi:10.1016/j.jhazmat.2012.12.008.

[119] P. Mao, Y. Liu, Y. Jiao, S. Chen, Y. Yang, Enhanced uptake of iodide on Ag@Cu2O

nanoparticles, Chemosphere. 164 (2016) 396–403. doi:10.1016/j.chemosphere.2016.08.116.

[120] S. V. Kireev, S.L. Shnyrev, Study of molecular iodine, iodate ions, iodide ions, and triiodide ions solutions absorption in the UV and visible light spectral bands, Laser Phys. 25 (2015) 75602. doi:10.1088/1054-660X/25/7/075602.

[121] S. V. Kireev, S.L. Shnyrev, Study of molecular iodine, iodate ions, iodide ions, and triiodide ions solutions absorption in the UV and visible light spectral bands, Laser Phys. 25 (2015) 75602. doi:10.1088/1054-660X/25/7/075602.

[122] P. Mao, Y. Liu, Y. Jiao, S. Chen, Y. Yang, Enhanced uptake of iodide on Ag@Cu2O nanoparticles, Chemosphere. 164 (2016) 396–403. doi:10.1016/j.chemosphere.2016.08.116.

[123] F.-S. Zhang, J.O. Nriagu, H. Itoh, Mercury removal from water using activated carbons derived from organic sewage sludge, Water Res. 391. Zhang (2005) 389–395. doi:https://doi.org/10.1016/j.watres.2004.09.027.

[124] A.K. Meena, G.K. Mishra, S. Kumar, C. Rajagopal, Low Cost Adsorbents for the Removal of Mercury (II) from Aqueous Solution- A Comparative Study, Def. Sci. J. 54 (2004) 537–548.

[125] N. Rahbar, A. Jahangiri, S. Boumi, M.J. Khodayar, Mercury removal from aqueous solutions with chitosan-coated magnetite nanoparticles optimized using the box-behnken design, Jundishapur J. Nat. Pharm. Prod. 9 (2014).

[126] Z. Qu, L. Fang, D. Chen, H. Xu, N. Yan, Effective and regenerable Ag/graphene adsorbent for Hg(II) removal from aqueous solution, Fuel. 203 (2017) 128–134. doi:10.1016/j.fuel.2017.04.105.

[127] M.B.P. Dos Santos, K.Z. Leal, F.J.S. Oliveira, S.M. Sella, M.D. Vieira, E.M.D. Marques, V.A.C. Gomes, Efficient removal of mercury from aqueous solutions and industrial effluent, J. Environ. Sci. Heal. Part A. 50 (2015) 1230–1240. doi:10.1080/10934529.2015.1055147.

[128] W. Liu, X. Zhao, T. Wang, J. Fu, J. Ni, Selective and irreversible adsorption of mercury(ii) from aqueous solution by a flower-like titanate nanomaterial, J. Mater. Chem. A. 3 (2015) 17676–17684. doi:10.1039/C5TA04521E.

[129] K. Abbas, H. Znad, M.R. Awual, A ligand anchored conjugate adsorbent for effective mercury(II) detection and removal from aqueous media, Chem. Eng. J. 334 (2018) 432–443. doi:10.1016/j.cej.2017.10.054.

[130] J.S. Hoskins, T. Karanfil, S.M. Serkiz, Removal and sequestration of iodide using silver-impregnated activated carbon, Environ. Sci. Technol. 36 (2002) 784–789. doi:10.1021/es010972m.

[131] T. Madrakian, A. Afkhami, M.A. Zolfigol, M. Ahmadi, N. Koukabi, Application of Modified Silica Coated Magnetite Nanoparticles for Removal of Iodine from Water Samples, Nano-Micro Lett. 4 (2012) 57–63. doi:10.1007/BF03353693.

[132] B. Riebe, S. Dultz, C. Bunnenberg, Temperature effects on iodine adsorption on organo-clay minerals - I. Influence of pretreatment and absorption temperature, Appl.

Clay Sci. 28 (2005) 9–16. doi:10.1016/j.clay.2004.01.004.

[133] X. Zhao, X. Han, Z. Li, H. Huang, D. Liu, C. Zhong, Enhanced removal of iodide from water induced by a metal-incorporated porous metal-organic framework, Appl. Surf. Sci. 351 (2015) 760–764. doi:10.1016/j.apsusc.2015.05.186.

[134] P. Mao, L. Qi, X. Liu, Y. Liu, Y. Jiao, S. Chen, Y. Yang, Synthesis of Cu/Cu2O hydrides for enhanced removal of iodide from water, J. Hazard. Mater. 237 (2017) 274–283.

[135] P. Mao, B. Qi, Y. Liu, L. Zhao, Y. Jiao, Y. Zhang, Z. Jiang, Q. Li, J. Wang, S. Chen, Y. Yang, AgII doped MIL-101 and its adsorption of iodine with high speed in solution, J. Solid State Chem. 237 (2016) 274–283. doi:https://doi.org/10.1016/j.jssc.2016.02.030.

[136] J.-L. Dai, M. Zhang, Y.-G. Zhu, Adsorption and desorption of iodine by various Chinese soils: I. Iodate, Environ. Int. 30 (2004) 525–530. doi:https://doi.org/10.1016/j.envint.2003.10.007.

[137] S. Liu, N. Wang, Y. Zhang, Y. Li, Z. Han, P. Na, Efficient removal of radioactive iodide ions from water by three-dimensional Ag2O–Ag/TiO2 composites under visible light irradiation, J. Hazard. Mater. 284 (2015) 171–181. doi:https://doi.org/10.1016/j.jhazmat.2014.10.054.

[138] J. Brassell, T. Ojumu, L. Petrik, Upscaling of Zeolite Synthesis from Coal Fly Ash Waste: Current Status and Future Outlook, 2016. doi:10.5772/63792.

[139] F.P. X. Querol, N. Moreno, J.C. Umana, A. Alastuey, E. Hernandez, A. Lopez-Soler, Synthesis of zeolites from coal fly ash: an overview, Int. J. Coal Geol. 50 (2002) 413–423. doi:10.1088/1757-899X/230/1/012044.

[140] M. Wdowin, M. Franus, R. Panek, L. Badura, W. Franus, The conversion technology of fly ash into zeolites, Clean Technol. Environ. Policy. 16 (2014) 1217–1223. doi:10.1007/s10098-014-0719-6.

[141] Y. WANG, Synthesis of zeolites using fly ash and their application in removing heavy metals from waters, Sci. China Ser. D. 46 (2003) 967. doi:10.1360/02yd0487.

[142] Y. WANG, Synthesis of zeolites using fly ash and their application in removing heavy metals from waters, Sci. China Ser. D. 46 (2003) 967. doi:10.1360/02yd0487.

[143] J. Luo, H. Zhang, J. Yang, Hydrothermal Synthesis of Sodalite on Alkali-Activated Coal Fly Ash for Removal of Lead Ions, Procedia Environ. Sci. 31 (2016) 605–614. doi:10.1016/j.proenv.2016.02.105.

[144] W. Franus, M. Wdowin, M. Franus, Synthesis and characterization of zeolites prepared from industrial fly ash, Environ. Monit. Assess. 186 (2014) 5721–5729. doi:10.1007/s10661-014-3815-5.

[145] N. Murayama, H. Yamamoto, J. Shibata, Mechanism of zeolite synthesis from coal fly ash by alkali hydrothermal reaction, Int. J. Miner. Process. 64 (2002) 1–17. doi:https://doi.org/10.1016/S0301-7516(01)00046-1.

[146] N. Shigemoto, H. Hayashi, K. Miyaura, Selective formation of Na-X zeolite from coal

fly ash by fusion with sodium hydroxide prior to hydrothermal reaction, J. Mater. Sci. 28 (1993) 4781–4786. doi:10.1007/BF00414272.

[147] V. Berkgaut, A. Singer, High capacity cation exchanger by hydrothermal zeolitization of coal fly ash, Appl. Clay Sci. 10 (1996) 369–378. doi:https://doi.org/10.1016/0169-1317(95)00033-X.

[148] H.-L. Chang, W.-H. Shih, A General Method for the Conversion of Fly Ash into Zeolites as Ion Exchangers for Cesium, Ind. Eng. Chem. Res. 37 (1998) 71–78. doi:10.1021/ie970362o.

[149] C. Belviso, F. Cavalcante, A. Lettino, S. Fiore, Effects of ultrasonic treatment on zeolite synthesized from coal fly ash, Ultrason. Sonochem. 18 (2011) 661–668. doi:https://doi.org/10.1016/j.ultsonch.2010.08.011.

[150] S.S. Bukhari, S. Rohani, H. Kazemian, Effect of ultrasound energy on the zeolitization of chemical extracts from fused coal fly ash, Ultrason Sonochem. 140 (2016) 250–266.

[151] C.D. Woolard, J. Strong, C.R. Erasmus, Evaluation of the use of modified coal ash as a potential sorbent for organic waste streams, Appl. Geochemistry. 17 (2002) 1159–1164. doi:https://doi.org/10.1016/S0883-2927(02)00057-4.

[152] N.M. Musyoka, L.F. Petrik, E. Hums, Ultrasonic assisted synthesis of zeolite A from coal fly ash using mine waters (acid mine drainage and circumneutral mine water) as a substitute for ultra pure water, Proc. Int. Miner. Water Assoc. Aachen, Ger. (2011) 423–428.

[153] S. Wang, Z.H. Zhu, Sonochemical treatment of fly ash for dye removal from wastewater, J. Hazard. Mater. 126 (2005) 91–95. doi:https://doi.org/10.1016/j.jhazmat.2005.06.009.

[154] X. Querol, A. Alastuey, A. López-Soler, F. Plana, J.M. Andrés, R. Juan, P. Ferrer, C.R. Ruiz, A Fast Method for Recycling Fly Ash: Microwave-Assisted Zeolite Synthesis, Environ. Sci. Technol. 31 (1997) 2527–2533. doi:10.1021/es960937t.

[155] J.M. Andrés, P. Ferrer, X. Querol, F. Plana, C. Juan, Zeolitisation of Coal Fly Ashes using Microwaves . Process Optimization, 1999 Int. Ash Util. Symp. (1999).

[156] M. Inada, H. Tsujimoto, Y. Eguchi, N. Enomoto, J. Hojo, Microwave-assisted zeolite synthesis from coal fly ash in hydrothermal process, Fuel. 84 (2005) 1482–1486. doi:https://doi.org/10.1016/j.fuel.2005.02.002.

[157] R.P. Penilla, A. Guerrero Bustos, S. Goñi Elizalde, Immobilization of Cs, Cd, Pb and Cr by synthetic zeolites from Spanish low-calcium coal fly ash, Fuel. 85 (2006) 823–832. doi:https://doi.org/10.1016/j.fuel.2005.08.022.

[158] V. Somerset, L. Petrik, E. Iwuoha, Alkaline hydrothermal conversion of fly ash precipitates into zeolites 3: The removal of mercury and lead ions from wastewater, J. Environ. Manage. 87 (2008) 125–131. doi:https://doi.org/10.1016/j.jenvman.2007.01.033.

[159] C.D. Woolard, K. Petrus, M. Van der Horst, The use of a modified fly ash as an adsorbent for lead, Water SA. 26 (2000) 531–536.

https://www.scopus.com/inward/record.uri?eid=2-s2.0-0033758336&partnerID=40&md5=389d29b400607a687dab6d7e623b888a.

[160] K.J. Scott, D. Darrow, J.H. Greinwald, R.J.H. Smith, Endobronchial Tumors in Children: An Uncommon Clinical Entity, Ann. Otol. Rhinol. Laryngol. 110 (2001) 63–69. doi:10.1177/000348940111000112.

[161] S. Golbad, P. Khoshnoud, N. Abu-Zahra, Hydrothermal synthesis of hydroxy sodalite from fly ash for the removal of lead ions from water, Int. J. Environ. Sci. Technol. 14 (2017) 135–142. doi:10.1007/s13762-016-1133-x.

[162] M.-G. Lee, J.-K. Cheon, S.-K. Kam, Heavy metal adsorption characteristics of zeolite synthesized from fly ash, J. Ind. Eng. Chem. 9 (2003) 174–180. https://www.scopus.com/inward/record.uri?eid=2-s2.0-26644467174&partnerID=40&md5=f4af9bb2202f84eb432385519cec2084.

[163] N. Koukouzas, C. Vasilatos, G. Itskos, I. Mitsis, A. Moutsatsou, Removal of heavy metals from wastewater using CFB-coal fly ash zeolitic materials, J. Hazard. Mater. 173 (2010) 581–588. doi:10.1016/j.jhazmat.2009.08.126.

[164] N. Moreno, X. Querol, C. Ayora, C.F. Pereira, M. Janssen-Jurkovicová, Utilization of Zeolites Synthesized from Coal Fly Ash for the Purification of Acid Mine Waters, Environ. Sci. Technol. 35 (2001) 3526–3534. doi:10.1021/es0002924.

[165] A. Derkowski, W. Franus, E. Beran, A. Czímerová, Properties and potential applications of zeolitic materials produced from fly ash using simple method of synthesis, Powder Technol. 166 (2006) 47–54. doi:10.1016/j.powtec.2006.05.004.

[166] N. Moreno, X. Querol, C. Ayora, C.F. Pereira, M. Janssen-Jurkovicová, Utilization of Zeolites Synthesized from Coal Fly Ash for the Purification of Acid Mine Waters, Environ. Sci. Technol. 35 (2001) 3526–3534. doi:10.1021/es0002924.

[167] W. Qiu, Y. Zheng, Removal of lead, copper, nickel, cobalt, and zinc from water by a cancrinite-type zeolite synthesized from fly ash, Chem. Eng. J. 145 (2009) 483–488. doi:https://doi.org/10.1016/j.cej.2008.05.001.

[168] K.S. Hui, C.Y.H. Chao, S.C. Kot, Removal of mixed heavy metal ions in wastewater by zeolite 4A and residual products from recycled coal fly ash, J. Hazard. Mater. 127 (2005) 89–101. doi:https://doi.org/10.1016/j.jhazmat.2005.06.027.

[169] Y. Fan, F.S. Zhang, J. Zhu, Z. Liu, Effective utilization of waste ash from MSW and coal co-combustion power plant-Zeolite synthesis, J. Hazard. Mater. 153 (2008) 382–388. doi:10.1016/j.jhazmat.2007.08.061.

[170] M. Zhang, H. Zhang, D. Xu, L. Han, D. Niu, B. Tian, J. Zhang, L. Zhang, W. Wu, Removal of ammonium from aqueous solutions using zeolite synthesized from fly ash by a fusion method, Desalination. 271 (2011) 111–121. doi:https://doi.org/10.1016/j.desal.2010.12.021.

[171] D. Wu, B. Zhang, C. Li, Z. Zhang, H. Kong, Simultaneous removal of ammonium and phosphate by zeolite synthesized from fly ash as influenced by salt treatment, J. Colloid Interface Sci. 304 (2006) 300–306. doi:https://doi.org/10.1016/j.jcis.2006.09.011.

[172] B. Zhang, D. Wu, C. Wang, S. He, Z. Zhang, H. Kong, Simultaneous removal of ammonium and phosphate by zeolite synthesized from coal fly ash as influenced by acid treatment, J. Environ. Sci. 19 (2007) 540–545. doi:https://doi.org/10.1016/S1001-0742(07)60090-4.

[173] L. Bandura, R. Panek, M. Rotko, W. Franus, Synthetic zeolites from fly ash for an effective trapping of BTX in gas stream, Microporous Mesoporous Mater. 223 (2016) 1–9. doi:https://doi.org/10.1016/j.micromeso.2015.10.032.

[174] A. Bandura, O. Skaskiv, Entire Functions of Bounded L-Index: Its Zeros and Behavior of Partial Logarithmic Derivatives, J. Complex Anal. 2017 (2017). doi:10.1155/2017/3253095.

[175] T. Sakthivel, D.L. Reid, I. Goldstein, L. Hench, S. Seal, Hydrophobic High Surface Area Zeolites Derived from Fly Ash for Oil Spill Remediation, Environ. Sci. Technol. 47 (2013) 5843–5850. doi:10.1021/es3048174.

[176] A. Srinivasan, M.W. Grutzeck, The Adsorption of SO2 by Zeolites Synthesized from Fly Ash, Environ. Sci. Technol. 33 (1999) 1464–1469. doi:10.1021/es9802091.

[177] X. Querol, N. Moreno, J.C. Umaa, R. Juan, S. Hernndez, C. Fernandez-Pereira, C. Ayora, M. Janssen, J. Garca-Martnez, A. Linares-Solano, D. Cazorla-Amoros, Application of zeolitic material synthesised from fly ash to the decontamination of waste water and flue gas, J. Chem. Technol. Biotechnol. 77 (2002) 292–298. doi:10.1002/jctb.597.

[178] I. Majchrzak-Kucęba, W. Nowak, A thermogravimetric study of the adsorption of CO2 on zeolites synthesized from fly ash, Thermochim. Acta. 437 (2005) 67–74. doi:https://doi.org/10.1016/j.tca.2005.06.003.

[179] F. Fotovat, M. Kazemeini, H. Kazemian, Novel Utilization of Zeolited Fly Ash Hosting Cobalt Nanoparticles as a Catalyst Applied to the Fischer–Tropsch Synthesis, Catal. Letters. 127 (2009) 204–212. doi:10.1007/s10562-008-9671-6.

[180] C.A. Ríos R., J.A. Oviedo V., J.A. Henao M., M.A. Macías L., A NaY zeolite synthesized from Colombian industrial coal by-products: Potential catalytic applications, Catal. Today. 190 (2012) 61–67. doi:https://doi.org/10.1016/j.cattod.2012.02.025.

[181] T. Yamamoto, A. Eiad-ua, S.I. Kim, T. Ohmori, Preparation and Characterization of Cobalt Cation-Exchanged NaX Zeolite as Catalyst for Wastewater Treatment, J. Ind. Eng. Chem. 13 (2007) 1142–1148.

[182] Y.-M. Nam, S.-M. Kim, J.-H. Lee, S.-J. Kim, S.-H. Chung, A study on the application of fly ash-derived zeolite materials for pyrolysis of polypropylene (II), J. Ind. Eng. Chem. 10 (2004) 788–793. https://www.scopus.com/inward/record.uri?eid=2-s2.0-34047093753&partnerID=40&md5=1c1dba0522b0acb74c526ec543865a3a.

[183] S.-S. Kim, J.-H. Kim, S.-H. Chung, A study on the application of fly ash-derived zeolite materials for pyrolysis of polypropylene, J. Ind. Eng. Chem. 9 (2003) 287–293. https://www.scopus.com/inward/record.uri?eid=2-s2.0-34047160870&partnerID=40&md5=3ca206b61e4f2305da9391cb77de153c.

[184] A.M. Cardoso, A. Paprocki, L.S. Ferret, C.M.N. Azevedo, M. Pires, Synthesis of zeolite Na-P1 under mild conditions using Brazilian coal fly ash and its application in wastewater treatment, Fuel. 139 (2015) 59–67. doi:10.1016/j.fuel.2014.08.016.

[185] T. Takagi, M. Sugeno, Fuzzy Identification of Systems and Its Applications to Modeling and Control, IEEE Trans. Syst. Man Cybern. SMC-15 (1985) 116–132. doi:10.1109/TSMC.1985.6313399.

[186] D.K. Pratihar, Soft Computing, Alpha Science International, Ltd, 2007.

[187] M. Suzuki, Adsorption engineering, Kodansha ; Elsevier, Tokyo : Amsterdam ; New York, 1990.

[188] V.J. Inglezakis, M.M. Fyrillas, J. Park, Variable diffusivity homogeneous surface diffusion model and analysis of merits and fallacies of simplified adsorption kinetics equations, J. Hazard. Mater. 367 (2019) 224–245. doi:10.1016/j.jhazmat.2018.12.023.

[189] Y.-S. Ho, Review of second-order models for adsorption systems, J. Hazard. Mater. 136 (2006) 681–689. doi:https://doi.org/10.1016/j.jhazmat.2005.12.043.

[190] G. Blanchard, M. Maunaye, G. Martin, Removal of heavy metals from waters by means of natural zeolites, Water Res. 18 (1984) 1501–1507. doi:doi:10.1016/0043-1354(84)90124-6.

[191] M. Sánchez-Polo, J. Rivera-Utrilla, E. Salhi, U. von Gunten, Ag-doped carbon aerogels for removing halide ions in water treatment, Water Res. 41 (2007) 1031–1037. doi:10.1016/j.watres.2006.07.009.

[192] K. Yu, X. Li, L. Chen, J. Fang, H. Chen, Q. Li, N. Chi, J. Ma, Mechanism and efficiency of contaminant reduction by hydrated electron in the sulfite/iodide/UV process, Water Res. 129 (2018) 357–364. doi:10.1016/j.watres.2017.11.030.

[193] J.S. Yoon, T. Lee, J.W. Choi, D.J. Suh, K. Lee, J.M. Ha, J. Choi, Layered MWW zeolite-supported Rh catalysts for the hydrodeoxygenation of lignin model compounds, Catal. Today. 293–294 (2017) 142–150. doi:10.1016/j.cattod.2016.10.033.

[194] T. Zhang, X. Yue, L. Gao, F. Qiu, J. Xu, J. Rong, J. Pan, Hierarchically porous bismuth oxide/layered double hydroxide composites: Preparation, characterization and iodine adsorption, J. Clean. Prod. 144 (2017) 220–227. doi:10.1016/j.jclepro.2017.01.030.

[195] X. Zhang, P. Gu, X. Li, G. Zhang, Efficient adsorption of radioactive iodide ion from simulated wastewater by nano Cu2O/Cu modified activated carbon, Chem. Eng. J. 322 (2017) 129–139. doi:10.1016/j.cej.2017.03.102.

[196] F.G. Helfferich, Ion Exchange, Dover, 1962. https://books.google.kz/books?id=F9OQMEA88CAC.

[197] M. Delkash, B. Ebrazi Bakhshayesh, H. Kazemian, Using zeolitic adsorbents to cleanup special wastewater streams: A review, Microporous Mesoporous Mater. 214 (2015) 224–241. doi:10.1016/j.micromeso.2015.04.039.

[198] T. V. Ojumu, P.W. Du Plessis, L.F. Petrik, Synthesis of zeolite A from coal fly ash using ultrasonic treatment - A replacement for fusion step, Ultrason. Sonochem. 31 (2016) 342–349. doi:10.1016/j.ultsonch.2016.01.016.

[199] A.Á.B. Maia, R.F. Neves, R.S. Angélica, H. Pöllmann, Synthesis of sodalite from Brazilian kaolin wastes, Clay Miner. 50 (2015) 663–675. doi:10.1180/claymin.2015.050.5.09.

[200] H. Liu, T. Shen, W. Wang, T. Li, Y. Yue, X. Bao, From natural aluminosilicate minerals to zeolites: Synthesis of ZSM-5 from rectorites activated via different methods, Appl. Clay Sci. 115 (2015) 201–211. doi:10.1016/j.clay.2015.07.040.

[201] C. Wang, L. Lippincott, I.-H. Yoon, X. Meng, Modeling, rate-limiting step investigation, and enhancement of the direct bio-regeneration of perchlorate laden anion-exchange resin, Water Res. 43 (2009) 127–136. doi:https://doi.org/10.1016/j.watres.2008.10.012.

[202] W. Ma, P.W. Brown, S. Komarneni, Characterization and cation exchange properties of zeolite synthesized from fly ashes, J. Mater. Res. 13 (1998) 3–7. doi:10.1557/JMR.1998.0001.

[203] M. Park, C.L. Choi, W.T. Lim, M.C. Kim, J. Choi, N.H. Heo, Molten-salt method for the synthesis of zeolitic materials I. Zeolite formation in alkaline molten-salt system, Microporous Mesoporous Mater. 37 (2000) 81–89. doi:10.1016/S1387-1811(99)00196-1.

[204] T. Hu, W. Gao, X. Liu, Y. Zhang, C. Meng, Synthesis of zeolites Na-A and Na-X from tablet compressed and calcinated coal fly ash, R. Soc. Open Sci. 4 (2017) 170921. doi:10.1098/rsos.170921.

[205] A. Derkowski, W. Franus, E. Beran, A. Czímerová, Properties and potential applications of zeolitic materials produced from fly ash using simple method of synthesis, Powder Technol. 166 (2006) 47–54. doi:https://doi.org/10.1016/j.powtec.2006.05.004.

[206] G.P. Zhou, Editorial: current progress in structural bioinformatics of protein-biomolecule interactions, Med Chem. 11 (2015) 216–217. doi:10.2174/1573406411666141229162618.

[207] G. Garcia, E. Cardenas, S. Cabrera, J. Hedlund, J. Mouzon, Synthesis of zeolite y from diatomite as silica source, Microporous Mesoporous Mater. 219 (2016) 29–37. doi:10.1016/j.micromeso.2015.07.015.

[208] P. Sharma, S.J. Jeong, M.H. Han, C.H. Cho, Influence of silica precursors on octahedron shaped nano NaY zeolite crystal synthesis, J. Taiwan Inst. Chem. Eng. 50 (2015) 259–265. doi:10.1016/j.jtice.2014.12.025.

[209] D. Wu, Y. Sui, S. He, X. Wang, C. Li, H. Kong, Removal of trivalent chromium from aqueous solution by zeolite synthesized from coal fly ash, J. Hazard. Mater. 155 (2008) 415–423. doi:10.1016/j.jhazmat.2007.11.082.

[210] H. Javadian, F. Ghorbani, H. allah Tayebi, S.M.H. Asl, Study of the adsorption of Cd (II) from aqueous solution using zeolite-based geopolymer, synthesized from coal fly

ash; kinetic, isotherm and thermodynamic studies, Arab. J. Chem. 8 (2015) 837–849. doi:10.1016/j.arabjc.2013.02.018.

[211] M.C. Manique, L.V. Lacerda, A.K. Alves, C.P. Bergmann, Biodiesel production using coal fly ash-derived sodalite as a heterogeneous catalyst, Fuel. 190 (2017) 268–273. doi:10.1016/j.fuel.2016.11.016.

[212] S. Zeng, R. Wang, Z. Zhang, S. Qiu, Solventless green synthesis of sodalite zeolite using diatomite as silica source by a microwave heating technique, Inorg. Chem. Commun. 70 (2016) 168–171. doi:10.1016/j.inoche.2016.06.013.

[213] J. Li, X. Zeng, X. Yang, C. Wang, X. Luo, Synthesis of pure sodalite with wool ball morphology from alkali fusion kaolin, Mater. Lett. 161 (2015) 157–159. doi:10.1016/j.matlet.2015.08.058.

[214] P. Atkins, J. De Paula, Atkins' Physical chemistry 8th edition, Chemistry (Easton). (2009) 430–468. doi:10.1021/ed056pA260.1.

[215] A. Henglein, C. Brancewicz, Absorption spectra and reactions of colloidal bimetallic nanoparticles containing mercury, Chem. Mater. 4756 (1997) 2164–2167.

[216] E. Sumesh, M.S. Bootharaju, Anshup, T. Pradeep, A practical silver nanoparticle-based adsorbent for the removal of Hg2+ from water, J. Hazard. Mater. 189 (2011) 450–457. doi:10.1016/j.jhazmat.2011.02.061.

[217] L. Deng, Y. Li, X. Yan, J. Xiao, C. Ma, J. Zheng, S. Liu, R. Yang, Ultrasensitive and highly selective detection of bioaccumulation of methyl-mercury in fish samples via ag0/hg0amalgamation, Anal. Chem. 87 (2015) 2452–2458. doi:10.1021/ac504538v.

[218] N. Panichev, M.M. Kalumba, K.L. Mandiwana, Solid phase extraction of trace amount of mercury from natural waters on silver and gold nanoparticles, Anal. Chim. Acta. 813 (2014) 56–62. doi:10.1016/j.aca.2014.01.011.

[219] J.T.T. Pang, I.M. Ritchie, The reactions between mercury ions and silver: dissolution and displacements, Electrochim. Acta. 27 (1982) 683–689. doi:10.1016/0013-4686(82)85060-3.

[220] V.J. Inglezakis, M.D. Loizidou, H.P. Grigoropoulou, Equilibrium and kinetic ion exchange studies of Pb2+, Cr3+, Fe3+ and Cu2+ on natural clinoptilolite, Water Res. 36 (2002) 2784–2792. doi:10.1016/S0043-1354(01)00504-8.

[221] A. Langella, M. Pansini, P. Cappelletti, B. De Gennaro, M. De' Gennaro, C. Colella, NH4+, Cu2+, Zn2+, Cd2+ and Pb2+ exchange for Na + in a sedimentary clinoptilolite, North Sardinia, Italy, Microporous Mesoporous Mater. 37 (2000) 337–343. doi:10.1016/S1387-1811(99)00276-0.

[222] T. Gong, X. Zhang, Determination of iodide, iodate and organo-iodine in waters with a new total organic iodine measurement approach, Water Res. 47 (2013) 6660–6669. doi:10.1016/j.watres.2013.08.039.

[223] D.B. Jones, A. Saglam, H. Song, T. Karanfil, The impact of bromide/iodide concentration and ratio on iodinated trihalomethane formation and speciation, Water Res. 46 (2012) 11–20. doi:https://doi.org/10.1016/j.watres.2011.10.005.

[224] Z. Sun, C. Zhang, P. Chen, Q. Zhou, M.R. Hoffmann, Impact of humic acid on the photoreductive degradation of perfluorooctane sulfonate (PFOS) by UV/Iodide process, Water Res. 127 (2017) 50–58. doi:10.1016/j.watres.2017.10.010.

[225] P. Mao, L. Qi, X. Liu, Y. Liu, Y. Jiao, S. Chen, Y. Yang, Synthesis of Cu/Cu<inf>2</inf>O hydrides for enhanced removal of iodide from water, J. Hazard. Mater. 237 (2017) 274–283.

[226] Y.Y. Chen, S.H. Yu, Q.Z. Yao, S.Q. Fu, G.T. Zhou, One-step synthesis of Ag2O@Mg(OH)2 nanocomposite as an efficient scavenger for iodine and uranium, J. Colloid Interface Sci. 510 (2018) 280–291. doi:10.1016/j.jcis.2017.09.073.

[227] J. Chen, Q. Gao, X. Zhang, Y. Liu, P. Wang, Y. Jiao, Y. Yang, Nanometer mixed-valence silver oxide enhancing adsorption of ZIF-8 for removal of iodide in solution, Sci. Total Environ. 646 (2019) 634–644. doi:10.1016/j.scitotenv.2018.07.298.

[228] F. Yu, Y. Chen, Y. Wang, C. Liu, W. Ma, Enhanced removal of iodide from aqueous solution by ozonation and subsequent adsorption on Ag-Ag2O modified on Carbon Spheres, Appl. Surf. Sci. 427 (2018) 753–762. doi:10.1016/j.apsusc.2017.08.089.

[229] A.M.S. Polo, I. Velo-Gala, M. Sánchez-Polo, U. von Gunten, J.J. López-Peñalver, J. Rivera-Utrilla, Halide removal from aqueous solution by novel silver-polymeric materials, Sci. Total Environ. 573 (2016) 1125–1131. doi:10.1016/j.scitotenv.2016.08.071.

[230] G. Lefèvre, J. Bessière, J.J. Ehrhardt, A. Walcarius, Immobilization of iodide on copper(I) sulfide minerals, in: J. Environ. Radioact., 2003: pp. 73–83. doi:10.1016/S0265-931X(03)00119-X.

[231] J. Warchoł, P. Misaelides, R. Petrus, D. Zamboulis, Preparation and application of organo-modified zeolitic material in the removal of chromates and iodides, J. Hazard. Mater. 137 (2006) 1410–1416. doi:https://doi.org/10.1016/j.jhazmat.2006.04.028.

[232] J. Liu, H.R. Hurt, Ion Release Kinetics and Particle Persistence in Aqueous Nano-Silver Colloids, Environ. Sci. Technol. 44 (2010) 2169–2175. doi:10.1021/es9035557.

[233] E. Krausmann, Y. Drossinos, A model of silver-iodine reactions in a light water reactor containment sump under severe accident conditions, J. Nucl. Mater. 264 (1999) 113–121. doi:10.1016/S0022-3115(98)00471-1.

[234] T.S. Peretyazhko, Q. Zhang, V.L. Colvin, Size-controlled dissolution of silver nanoparticles at neutral and acidic pH conditions: Kinetics and size changes, Environ. Sci. Technol. 48 (2014) 11954–11961. doi:10.1021/es5023202.

[235] B. Molleman, T. Hiemstra, Time, pH, and size dependency of silver nanoparticle dissolution: The road to equilibrium, Environ. Sci. Nano. 4 (2017) 1314–1327. doi:10.1039/c6en00564k.

[236] A. Dyer, S. Tangkawanit, K. Rangsriwatananon, Exchange diffusion of Cu2+, Ni2+, Pb2+ and Zn2+ into analcime synthesized from perlite, Microporous Mesoporous Mater. 75 (2004) 273–279. doi:10.1016/j.micromeso.2004.07.007.

[237] V.J. Inglezakis, M.M. Fyrillas, M.A. Stylianou, Two-phase homogeneous diffusion

model for the fixed bed sorption of heavy metals on natural zeolites, Microporous Mesoporous Mater. 266 (2018) 164–176. doi:10.1016/j.micromeso.2018.02.045.

[238] J. Mon, Y. Deng, M. Flury, J.B. Harsh, Cesium incorporation and diffusion in cancrinite, sodalite, zeolite, and allophane, Microporous Mesoporous Mater. 86 (2005) 277–286. doi:10.1016/j.micromeso.2005.07.030.

[239] R.F. Sippel, sodium self diffusion in natural minerals, Geochim. Cosmochim. Acta. 27 (1963) 107–120.